Avian Wing Joints Provide Longitudinal Flight Stability and Control

by

Christina Harvey

A dissertation submitted in partial fulfillment
of the requirements for the degree of
Doctor of Philosophy
(Aerospace Engineering)
in The University of Michigan
2022

Doctoral Committee:

Professor Daniel J. Inman, Chair
Professor Douglas L. Altshuler, University of British Columbia
Professor Carlos E.S. Cesnik
Professor Eric Johnsen

Christina Harvey

harveyca@umich.edu

ORCID iD: 0000-0002-2830-0844

Acknowledgements

[Research] is like being lost in a jungle and trying to use all the knowledge that you can gather to come up with some new tricks, and with some luck, you might find a way out.

– Maryam Mirzakhani

First and foremost, thank you Dr. Inman. Coming to Michigan to work with you is the reason I was able to continue to develop my passion and propelled me to pursue an academic position. I am very grateful that you've always given me the freedom and support to follow the science where it led. This thesis never would have happened without the AFOSR BRI "Avian-Inspired Multifunctional Morphing Vehicles" monitored by Dr. B.L. Lee. That grant was the reason that I met Dr. Inman and has supported both my masters and PhD studies. Thank you Doug for your support and advice throughout my career and for taking the chance on hiring an engineer into a zoology program in the first place.

Although never an official advisor, Vikram you taught me so much about, well, many things, from evolution to statistics to the fact that I use too many commas (working on it). Jasmin, thank you for your friendship and willingness to chat over a beer. I am looking forward to many more collaborations with you both. Thank you to everyone in AIMS Lab, past and present. In particular, thank you Kevin and Piper, you have made this journey a blast. Shout out to all of my incoming cohort including Leanne, Austin, and Thomas. I would go through prelims again if it meant getting to regularly spend more time with you all. Thank you Jana (and Parker and Darcy) for your support and friendship. Thank you to the members of the graduate and departmental diversity, equity, and inclusion committees. Working with you all has brought me a greater sense of purpose and joy.

Thank you Mom, Dad, Grandpa, Sam, and James for supporting me, celebrating my achievements, and checking in on me when I need it most. Finally, to Josh. You are my best friend and continually bring so much happiness into my life. I am forever grateful that I get to go through life with you as my partner and I look forward to our many future adventures together.

This work is supported in part by the US Air Force Office of Scientific Research (AFOSR) under grant number FA9550-16-1-0087, titled “Avian-Inspired Multifunctional Morphing Vehicles” and grant number FA9550-21-1-0325, titled “Towards Neural Control for Fly-by-Feel Morphing” monitored by Dr. B.L. Lee and in part by the National Science Foundation (NSF) under grant number 1935216. My studies were further supported by personal fellowships and scholarships from the National Science and Engineering Research Council of Canada (NSERC PGS-D, 2018-2021), the Francois-Xavier Bagnoud Fellowship awarded by FXB International through the University of Michigan Department of Aerospace Engineering (2019-2022) as well as the Zonta International Amelia Earhart Fellowship (2021-2022).

Table of Contents

List of Tables

List of Figures

List of Symbols

Symbol	Definition	Units
b	Wing span (wing tip to wing tip)	m
c	Chord (characteristic length)	m
c_m	Mean chord	m
c_{max}	Maximum (mean or root) chord for all morphed configurations	m
c_r	Wing root chord, i.e. $c(0)$	m
$c_{r_{max}}$	Maximum wing root chord for one specimen	m
$c(y)$	Wing chord as a function of the span position	m
e	Elbow angle	$^\circ$
g	gravitational acceleration	$m \cdot s^{-}2$
l_t	Distance from the center of gravity to tail aerodynamic center	m
m	Mass	kg
n	Sample size	varies
p	Roll rate	$rad \cdot s^{-1}$
q	Pitch rate	$rad \cdot s^{-1}$
r	Yaw rate	$rad \cdot s^{-1}$
re	Real component of the eigenvalue	varies
im	Imaginary component of the eigenvalue	varies
t	Time	s
u_g	Gust velocity	$m \cdot s^{-1}$
$\mathbf{v}$	Velocity vector	$m \cdot s^{-1}$
w	Wrist angle	$^\circ$
x	Position along the *x*-axis in the body frame	m
x_c	Position along the *x*-axis in the stability frame	m
$x_{c/4}$	*x*-axis position of the quarter chord	m
$\tilde{x}_{c/4}$	*x*-axis position of the quarter standard mean chord	m
x_{CG}	*x*-axis position of the center of gravity	m
x_{NP}	*x*-axis position of the neutral point	m
$x_{NP_{wb}}$	*x*-axis position of the wing-body neutral point	m
y	Position along the *y*-axis in the body frame	m

y_{cen}	*y*-axis position of the wing's centroid	m
y_{CG}	*y*-axis position of the center of gravity	m
z	Position along the *z*-axis in the body frame	m
z_c	Position along the *z*-axis in the stability frame	m
z_{CG}	*z*-axis position of the center of gravity	m
A	System matrix	varies
A_i	Coefficients from linear model fits	varies
B	Input coupling matrix	varies
B_i	Coefficients from linear model fits	varies
C_D	Drag coefficient	–
$C_{D_{morph}}$	Drag coefficient relative to max. wing characteristics	–
C_L	Lift coefficient	–
$C_{L_{morph}}$	Lift coefficient relative to max. wing characteristics	–
$C_{L_{\alpha_t}}$	Lift-slope of the tail	–
C_{L_α}	Lift-slope of the wing-body configuration	–
C_M	Pitch coefficient	–
$C_{M_{morph}}$	Pitch coefficient relative to max. wing characteristics	–
D	Drag	N
D_i	Coefficients from linear model fits	varies
E_i	Coefficients from linear model fits	varies
$\mathbf{F}$	Force vector	N
G_i	Coefficients from linear model fits	varies
$\mathbf{I}$	Moment of inertia tensor	$kg \cdot m^{-2}$
I_{xx}	Moment of inertia component about the *x*-axis	$kg \cdot m^{-2}$
I_{xz}	Moment of inertia component in the *x*-*z* plane	$kg \cdot m^{-2}$
I_{yy}	Moment of inertia component about the *y*-axis	$kg \cdot m^{-2}$
I_{zz}	Moment of inertia component about the *z*-axis	$kg \cdot m^{-2}$
L	Lift	N
M	Pitching moment	$N \cdot m$
$\mathbf{M}$	Moment vector	$N \cdot m$
S	Characteristic area	m^2
S_t	Tail area	m^2
S_w	Wing area	m^2
S_{max}	Maximum wing area for all morphed configurations	m^2
U	*x*-axis velocity component	$m \cdot s^{-1}$
U_∞	Freestream scalar velocity	$m \cdot s^{-1}$

$\mathbf{U}$	Input vector	varies
V	y-axis velocity component	$m \cdot s^{-1}$
W	z-axis velocity component	$m \cdot s^{-1}$
V_H	Tail volume coefficient	–
W	Weight	N
$\mathbf{X}$	State vector	varies
α	Angle of attack	rad or $^\circ$
α_{OU}	Selection strength of the OU model	–
β	Sideslip angle	rad
γ	Flight path angle	rad
ϵ	Downwash angle due to the wing	rad
ζ	Damping ratio	–
η	Effect size component (i.e., partial η^2 is the effect size)	–
η_t	Dynamic pressure ratio at the horizontal tail	–
θ	Pitch angle in the body axis	rad
θ_{CG}	Phenotypic optimum of the center of gravity	varies
θ_{SM}	Phenotypic optimum of the static margin	varies
λ	Eigenvalue	varies
ν	Inverse Wishart scalar degrees of freedom	–
μ	Dynamic viscosity	$kg \cdot m^{-1} \cdot s^{-1}$
ρ	Fluid density	$kg \cdot m^{-3}$
σ	Variance	varies
ϕ	Roll angle in the body axis	rad
ψ	Yaw angle in the body axis	rad
ω	Frequency	rad/s
$\boldsymbol{\omega}$	Angular velocity vector	rad/s
Γ	Sweep angle at the shoulder joint	$^\circ$
Λ	Dihedral angle at the shoulder joint	$^\circ$

**Note: Overdot signifies a time derivative of the variable. Subscript of 0 indicates the trim condition.*

List of Abbreviations

AIC	**A**kaike **I**nformation **C**riterion
AICc	**A**kaike **I**nformation **C**riterion with **c**orrection for small sample sizes
BM	**B**rownian **M**otion
CG	**C**enter of **G**ravity
OU	**O**rnstein **U**hlenbeck
MAC	**M**ean **A**erodynamic **C**enter
MCMC	**M**arkov-**C**hain **M**onte **C**arlo
NP	**N**eutral **P**oint
PGLMM	**P**hylogenetic **G**eneralized **L**inear **M**ixed **M**odels
ROM	**R**ange **O**f **M**otion
UAV	**U**ncrewed **A**erial **V**ehicle
VRP	**V**ehicle **R**eference **P**oint
3D	Three (**3**) **D**imensional

Abstract

Uncrewed aerial vehicle (UAV) design has advanced substantially over the past century; however, there are still scenarios where birds outperform UAVs. Birds regularly maneuver through cluttered environments or adapt to sudden changes in flight conditions, tasks that challenge even the most advanced UAVs. Thus, there remains a gap in our general knowledge of flight maneuverability and adaptability that can be filled by improving our understanding of how birds achieve these desirable flight characteristics. Although maneuverability is difficult to quantify, one approach is to leverage an expected trade-off between stability and maneuverability, wherein a stable flyer must generate larger moments to maneuver than an unstable flyer. Bird's stability, and adaptability, has previously been associated with their ability to morph their wing shape in flight. Birds morph their wings by actuating their musculoskeletal system, including the shoulder, elbow and wrist joints. Thus, to take an important step towards deciphering avian flight stability and adaptability, I investigated how the manipulating avian wing joints affect longitudinal stability and control characteristics.

First, I used an open-source low fidelity model to calculate the lift and pitching moment of a gull wing and body across the full range of flexion and extension of the elbow and wrist. To validate the model, I measured the forces and moments on nine 3D printed equivalent wing-body models mounted in a wind tunnel. With the validated numerical results, I identified that extending the wing using different combinations of elbow and wrist angles would provide a method for adaptive control of loads and static stability. However, I also found that gulls were unable to trim for the tested shoulder angle.

Next, I developed an open-source, mechanics-based method (AvInertia) to calculate the inertial characteristics of 22 bird species across the full range of flexion and extension of the elbow and wrist. This method allowed a detailed investigation of how manipulating the elbow and wrist angle changed the center of gravity and moment of inertia tensor. Leveraging the previous aerodynamic results, I developed a method to estimate the neutral point of any bird wing

configuration and derived a novel metric for pitch agility. With the neutral point and center of gravity, I found that the majority of investigated species had the ability to shift between stable and unstable flight. Further, I implemented an evolutionary analysis that revealed evidence of evolutionary pressures maintaining this capacity to shift, which transforms our understanding of avian flight evolution.

Finally, I combined the aerodynamic and inertial results to investigate the dynamic stability of a gull across a range of shoulder, elbow, and wrist angles. This analysis revealed that a positive dihedral and forward-swept wing allowed a trimmed flight condition. For trimmed configurations, I found that high wrist angles were statically unstable and exhibited a non-oscillating, divergent response to disturbances. Lower wrist angles were both statically and dynamically stable and exhibited a short period and phugoid mode like traditional aircraft. I found that most trimmed configurations exhibited short period characteristics that would be flyable by a human pilot, although with a heavily damped phugoid mode.

In summary, I found that the avian elbow and wrist joints can act as adaptive controls and permit birds to shift between stable and unstable flight. Identifying these characteristics provides a starting point for future UAV designs that hope to incorporate avian-like maneuverability and adaptability.

Chapter 1

Introduction

I saw a billboard with a bird sitting on the rim of a nest, nurturing her young fledglings into the flying world. It read, "Birds Learn to Fly. Why Can't You?" That did it.

– Janet Harmon Bragg

1.1 The rise of the uncrewed aerial vehicle

From our first successful gliders to modern supersonic jets, aircraft design has come a long way and broken through many seemingly impossible barriers. One such barrier was to remove the human pilot while maintaining control of the aircraft's flight path. In 1898, Nicola Tesla laid the necessary ground work by designing the first radio-controlled vehicle, an electric boat [1, 2]. Following the advent of this technology, the UK's Royal Aircraft Factory developed the "Aerial Target", a deceptively-named, radio-controlled, explosive-filled aircraft [3, 4]. The first flight tests for this aircraft were in 1916 [4], just 13 years after the Wright brothers made world history with the first powered, controlled (and crewed) flight. For the following two decades, most developments in radio-controlled aerial vehicles focused on, what was essentially the precursor to the modern cruise missiles, such as the Curtiss-Sperry Aerial Torpedo and the Kettering Bug [2, 5]. It was not until 1932 that De Havilland designed and flew an uncrewed target aircraft designed for training the UK's anti-aircraft defenses. Originally named the Fairey Queen, the company adjusted to a lower-cost design that was re-named the DH-82B Queen Bee [3, 4]. The Queen Bee is largely considered to be the precursor of the modern uncrewed aerial vehicle (UAV). Notably, the name of this aircraft is believed to be have been the origin of the terminology "drone", which is also a name for a male honey bee [2].

Since these early days, UAV designs have evolved drastically, ranging across multiple orders of magnitude in scale and weight. Designs have also branched out from a conventional fixed-wing design into rotorcraft and aircraft that morph the shape of their wings in flight [6]. In addition to their "morphological" diversity, modern UAVs are also no longer solely used for warfare or combat [3, 7], having become indispensable tools for many different missions. Modern uses for UAVs include environmental and climate monitoring [8, 9], assessing infrastructure [10, 11], agriculture [12, 13], humanitarian missons such as disaster management [14, 15] and public health support [16, 17], and possibly package delivery [18].

Despite the extraordinary advancements in the field, UAVs still exhibit a few key weaknesses. UAVs are often constrained by their range, endurance, and/or payload capacity. Further, UAVs struggle to operate effectively between distinct missions or disparate flight conditions. For example, a surveillance drone is not effective for maneuvering through cluttered environments and maneuverable quadcopters can be destabilized by gusty conditions. Thus, it would be beneficial for a UAV to be able to adapt to different missions and to sudden flight disturbances. It is this challenge, the concept of adaptability, that is a focus for this thesis.

UAV adaptability is limited, in part, because of an expected trade-off between aircraft maneuverability and efficiency. Since maneuverability can encompass a broad range of attributes, for the purposes of this work, I define maneuverability as the ability to change the velocity vector direction and/or magnitude [19, 20]. Conventionally, a surveillance drone with longer wings is more aerodynamically efficient and can cover a larger range than smaller designs. However, aircraft with large wingspans also have a larger moment of inertia and mass, which reduce their capacity for translational and rotational accelerations. This trade-off is one of the reasons that there is such a diversity of aircraft designs, as each aircraft needs to be intentionally designed to satisfy its particular mission constraints and goals. Therefore, with the intention of advancing adaptability and maneuverability in mind, we can now look for novel ways to improve and advance the design of adaptable and maneuverable UAVs.

1.2 Deriving inspiration from birds

There are over 10,000 species of birds [21] with body masses spanning four-orders of magnitude, from 0.002 kg to 20 kg. Avian morphology is extremely diverse with much variation in the size and shape of wings, tails, and bodies. Understanding avian diversity as well as the evolutionary pressures that have led to modern species is a major driver for some ornithological studies. To survive and procreate, different species rely on different strategies that may, or may not, require specific flight characteristics for success. In fact, flightlessness has independently evolved across and within multiple lineages of birds [22]. Thus, it cannot be assumed that birds have been evolving towards an optimal flight configuration [23].

Nevertheless, some birds exhibit flight styles that are more maneuverable and adaptable than comparatively-sized aircraft [24] such as navigating through crowded cities and forests [25] as well as performing evasive maneuvers to escape from predators [26]. For example, gulls (colloquially seagulls) are flight generalists that can perform thermal or dynamic soaring [27] as well as cleverly maneuver to steal food from other unsuspecting birds (or tourists) [28]. These flight generalists provide a promising model for adaptable UAV designs as a single bird can effectively operate at conditions that would satisfy many disparate mission profiles.

1.3 Defining comparable regimes

To this end, birds have long provided a source of inspiration for UAV design [6, 29–33]. However, it is important to understand the similarities and differences between birds and UAVs to best identify the characteristics of bird flight that are most desirable for enhancing UAV designs. Although many birds rely heavily on flapping flight as a means of transportation, in this thesis I narrowed my focus to gliding flight in particular. This allows for a more direct comparison to non-rotary and non-flapping vehicles that fall within Class I as defined by the NATO classification (i.e., UAVs with a mass less than 20 kg) [34]. Of note, the heaviest flighted bird, the great buzzard (*Otis tarda*) also weighs up to 20 kg.

To enable a comparison between two flyers, it is important to quantify two flow similarity parameters: the Mach number and the Reynolds number. As these numbers were not readily

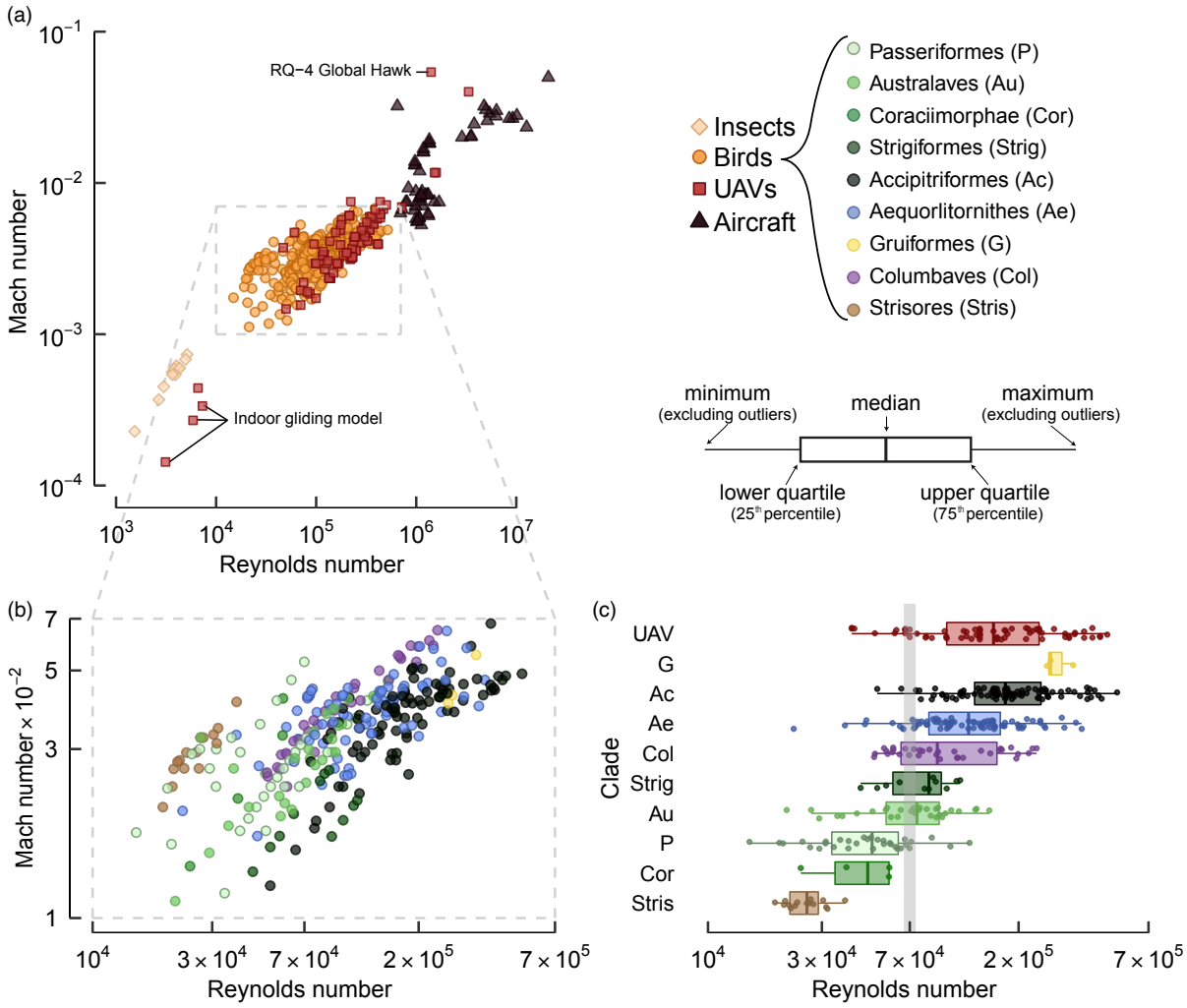

Figure 1.1: **Gliding bird Reynolds and Mach number regimes.** (a) Reynolds (Re) and Mach (M) number flight regimes. (b) Flight regime for gliding birds colored by clade. (c) Reynolds number regime for each avian clade, the transparent gray line represents approximately the critical Reynolds number $\approx 10^4$ per smooth airfoil classifications.

available for birds, I surveyed the literature to identify studies that reported both non-flapping airspeeds and wing shape parameters. With the outputs of this survey, I calculated the range of Mach and Reynolds numbers used by birds, insects, UAVs, and crewed aircraft (Fig. 1.1) [8, 25, 33, 35–114]. For birds, the ranges were computed from live measurements where birds were observed to hold their wings extended during some portion of the flight and does not include any flapping-only flights. Airspeed measurements were reported using varied techniques including global positioning system (GPS) loggers, rangefinders, radar, and wind tunnel studies.

The first important flow similarity parameter is the Mach number, which quantifies the compressibility of the flow. Mach number is the ratio of the freestream velocity to the speed of sound. Defining the Mach number regime is important when traveling close to or above the speed of sound. Gliding birds do not approach this barrier with a Mach number range of 0.01 to 0.08 (Fig. 1.1a and b). Since this range of gliding bird flight occurs well below 0.3, it can be modeled as incompressible flow [115].

The second important flow similarity parameter is the Reynolds number, which quantifies the ratio of inertial to viscous properties in a flow as defined by:

$$\text{Reynolds number} = \frac{\rho c U_\infty}{\mu} \tag{1.1}$$

where c represents the characteristic length scale, U_∞ represents the incoming freestream velocity, and ρ and μ represent the air density and dynamic viscosity, respectively.

Unlike large aircraft or small insects, birds and UAVs operate at an intermediate Reynolds number where neither viscous nor inertial effects can be neglected (Fig. 1.1a and b). Specifically, I found that gliding bird flight occurs between a Reynolds number of 1.5×10^4 to 5.2×10^5, if the characteristic length (c) is selected to be the mean projected wing chord (defined as the projected wing area divided by projected wingspan). In the aeronautical literature, the characteristic length is usually chosen as the mean aerodynamic chord, defined as a weighted average of the wing chord along the span. However, most avian studies do not publish the wing chord as a function of span and instead often publish a mean projected chord calculated from a fully extended wing. Because birds have been observed to both increase or decrease their mean projected chord as wind speeds increase, there is increased uncertainty on the upper Reynolds number bound [39, 85].

It is informative to separate the collected avian data into major clades defined by the phylogenetic classification established by Prum et. al (Fig. 1.1c and Table 1.1) [116]. A phylogeny captures how closely related different species are, in a manner similar to a family tree. Clades with large species such as seabirds (Aequorlitornithes) and raptors (Accipitriformes) tend to glide near the upper bound of the Reynolds number range whereas small birds such as swifts (Strisores) and passerines (Passeriformes) tend to glide near the lower bound (Fig. 1.1c). These

Table 1.1: **Phylogenetic grouping of avian species.**

Clade	Example species
Galloanserae	Quail, ducks, geese, chickens
Strisores	Common nighthawk, swift
Columbaves	Pigeon, Wood pigeon
Gruiformes	Common crane
Aequorlitornithes	Gulls, albatrosses, storks, pelicans
Accipitriformes	Hawks, harriers, buzzards, eagles
Strigiformes	Great horned owl, barn owl
Coraciimorphae	Lewis' woodpecker, European bee-eater
Australaves	Falcons, merlins, kestrals
Passeriformes	Starlings, jackdaws, jays, magpies

trends are largely a function of the overall size of the birds within these clades. Figure 1.2a shows Reynolds number as a function of the total mass of the bird where the increasing trend is expected because heavier birds tend to have larger mean projected chords (c, Fig. 1.2b) and fly at higher speeds (U_∞) [117].

Next, I separated the avian Reynolds number regime into four sub-regimes that Carmichael defined for smooth airfoils (Table 1.2) [118]. Birds glide within subcritical and supercritical sub-regimes . In a subcritical regime (Reynolds number $\leq 7 \times 10^4$), once the laminar boundary

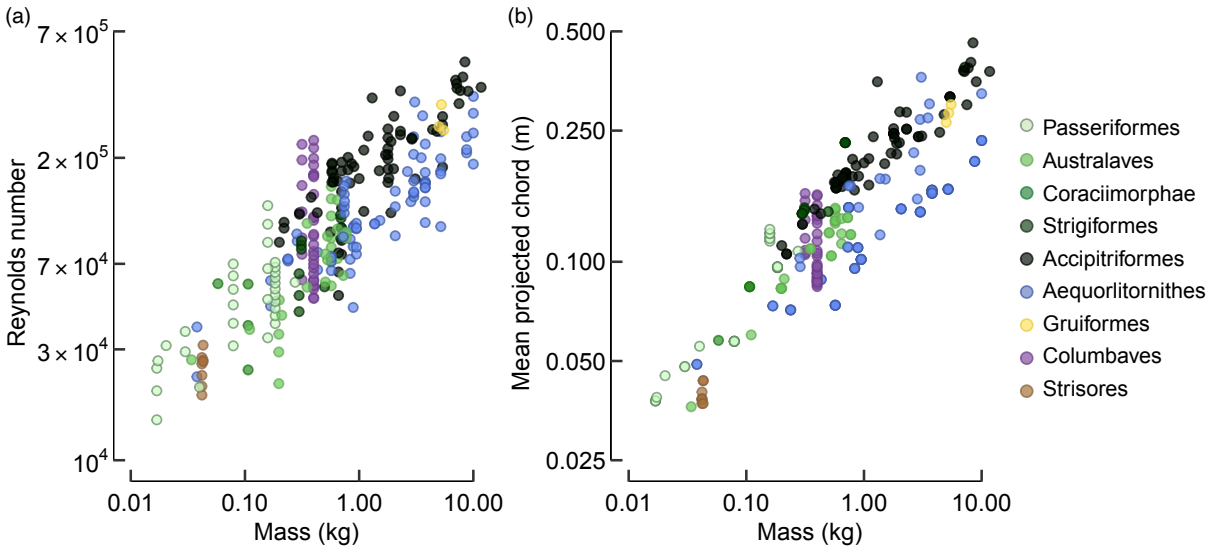

Figure 1.2: **Reynolds number and chord correlates with body mass.** (a) Reynolds number and (b) mean projected chord (c) tend to increase as body mass increases.

Table 1.2: **Reynolds number sub-regimes for gliding birds.** The bold line separates subcritical from supercritical regimes as defined for smooth airfoils by Carmichael [118].

Regime	Reynolds number	Clades	Example species
subcritical	1×10^4 to 3×10^4	Strisores	Swifts (low speed)
		Aequorlitornithes	Small petrel
		Coraciimorphae	Woodpecker
		Australaves	Common kestrel, budgerigar
		Passeriformes	Skylark
subcritical	3×10^4 to 7×10^4	Strisores	Swifts (high speed)
		Columbaves	Pigeon (low speed)
		Aequorlitornithes	Prion, small petrel
		Accipitriformes	Harris's hawk
		Strigiformes	Barn owl
		Coraciimorphae	European bee-eater
		Australaves	Kestrels, falcons
		Passeriformes	Jackdaw, magpie, woodpecker
supercritical	7×10^4 to 2×10^5	Columbaves	Pigeon (average speed)
		Aequorlitornithes	Gulls, albatross, large petrels
		Accipitriformes	Hawks, vultures, eagles, osprey
		Strigidae	Barn owl, barred owl
		Australaves	Falcons
		Passeriformes	Jackdaw, magpie
supercritical	2×10^5 to 7×10^5	Columbaves	Pigeon (high speed)
		Gruiformes	Common crane
		Aequorlitornithes	Storks, pelicans, albatrosses
		Accipitriformes	Large eagles, vultures, condors

layer separates from the surface, the airfoil chord is too short relative to the flow velocity to allow the separated boundary layer to transition to turbulent flow and reattach [118, 119]. This severely degrades performance. Carmichael noted that for Reynolds number $\leq 3 \times 10^4$ the flow is extensively laminar which results in higher aerodynamic efficiency, albeit at lower lift coefficients, than at the higher subcritical sub-regime [118].

The supercritical regimes used by birds are normally characterized by laminar separation bubbles (LSBs). LSBs occur when the laminar boundary layer separates from an airfoil, transitions to turbulent flow, and then reattaches to the airfoil as a turbulent boundary layer [119]. The region of separated flow is the "bubble" and degrades wing performance depending on its stability and length [118, 119]. LSBs can be partially or completely eliminated by artificially

tripping a laminar boundary layer to transition to turbulent flow. Introducing surface roughness can trip a boundary layer and feather roughness performs a similar function [33, 120]. For Reynolds number $\geq 2 \times 10^5$, LSBs still exist although the performance markedly improves over the lower regimes [118].

Note that Table 1.2 is meant to support a qualitative understanding, but bird wings are three-dimensional, rough, porous, flexible, and have a variable chord length. As such, a single bird wing may have airfoils simultaneously operating in multiple Reynolds number regimes that do not correspond to the Reynolds number regimes experienced by a smooth airfoil.

This survey does not encompass all avian biodiversity because some birds do not glide and not all birds that do glide have been studied. Of note, I identified only one published gliding measurement for the Galloanserae clade (Table 1.1), the barnacle goose (*Branta leucopsis*) that was gliding at an airspeed of approximately 14.2 m/s (Reynolds number = 1.5×10^5 and Mach number = 0.04) [121].

1.4 Why not discuss efficiency

Throughout the literature on bio-inspired UAVs, birds' superior aerodynamic efficiency is often cited as a source of inspiration for design. However, there is no direct comparison between the efficiency of birds and UAVs that could readily support such an assertion. Therefore, I reviewed the literature and compared the aerodynamic efficiencies of gliding birds to UAVs [122]. I quantified the aerodynamic efficiency of both flyers with the maximum lift-to-drag ratio.

First, I surveyed the aeronautical literature to identify UAVs that are comparable to birds. The UAVs included in this comparison had wing loadings and total mass on the same scale as birds (Fig. 1.3a and b) [8, 33, 40, 45, 46, 48, 53–55, 57, 64, 70, 96, 97, 104, 110]. However, multiple UAVs were lighter than birds that glided at similar Reynolds number, including Aerovironment's Black Widow and the Colorado MAV [55, 57]. One heavier exception was the URCUNINA-UAV, which weighs 16 kg and has a wing loading of 21 kg/m^2 [8]. This UAV literature survey included force measurements from wind tunnel experiments, velocity measurements from onboard equipment in free flight, and numerical predictions from CFD

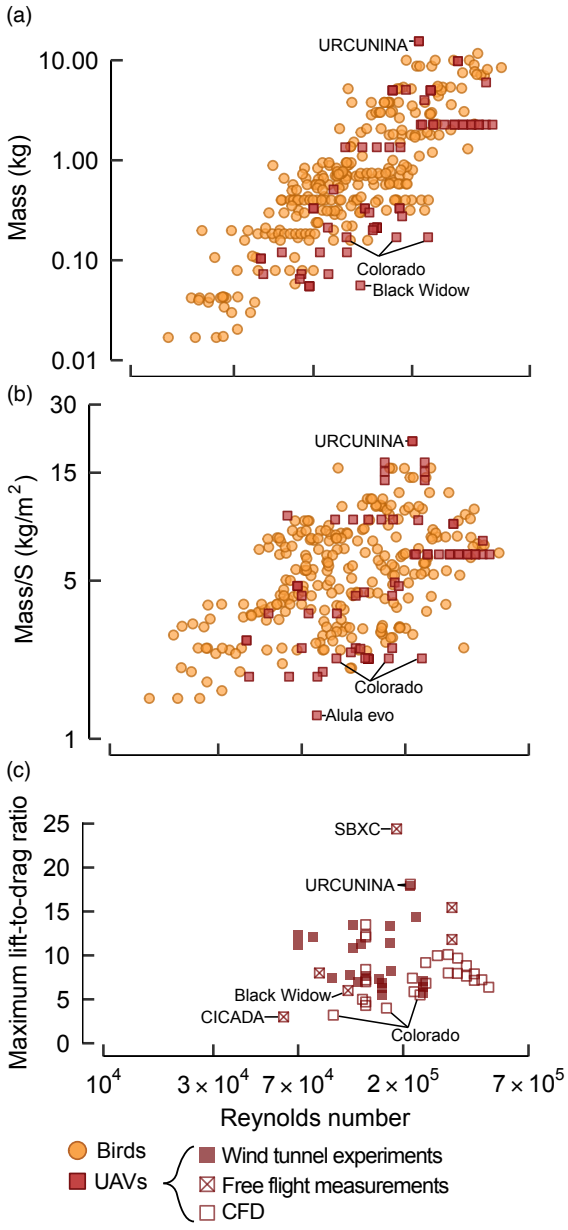

Figure 1.3: **Selected UAVs for comparison to birds.** (a) UAV and bird masses (b) UAV and bird wing loading (c) UAV aerodynamic efficiency by measurement type

methods. The uncertainty of each method can be highly variable and is discussed in more detail in [122]. I found that the maximum lift-to-drag ratio of UAVs that fly in the same regime as birds, ranges from 3–14 with a few exceptions (Fig. 1.3c). The URCUNINA-UAV and an SBXC glider have a high reported efficiency of 18 and 24, respectively [8, 53]. This is not a surprise as URCUNINA-UAV was designed for volcano monitoring and utilizes a pusher propeller configuration while the SBXC is a hand-launched unpowered glider.

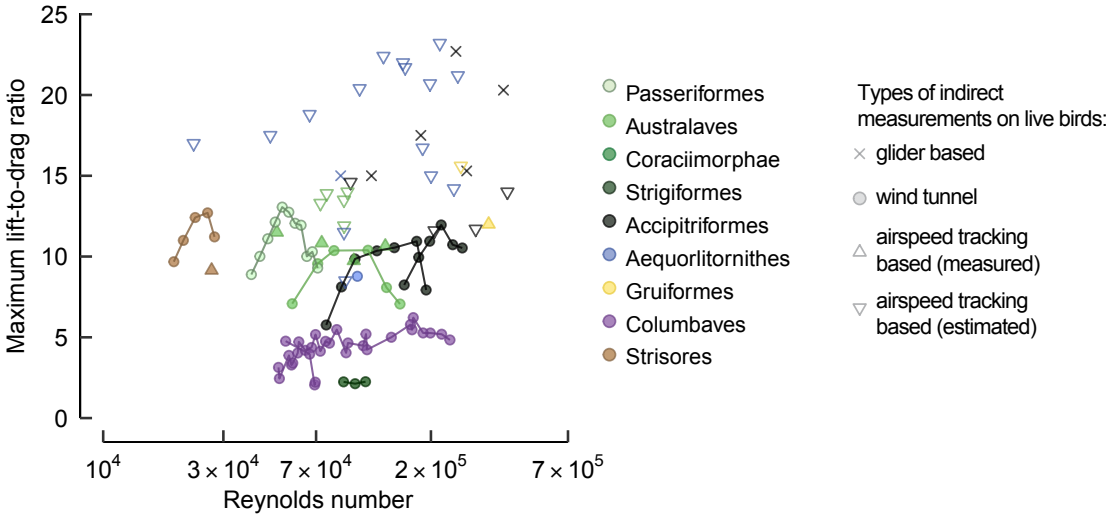

Figure 1.4: **Aerodynamic efficiency of birds.** Maximum lift-to-drag ratio of gliding birds. Solid lines connect measurements on the same individual.

Next, I surveyed the biological literature to identify measurements of the maximum lift-to-drag ratio of gliding birds (Fig. 1.4). Similar to UAVs, these results were obtained with different measurement methodologies that each have different sources of uncertainty. These are discussed in detail in [122]. Of note, I found that there was evidence of extremely high experimental uncertainty in the theoretical predictions and glider based studies (upside down triangles and crosses in Fig. 1.4). Further, measurements on live birds in steady, gliding flight in a wind tunnel were noted to represent a minimum bound on the birds' aerodynamic efficiency due to behavioral implications [122].

With this collected data it is now possible to compare the aerodynamic efficiency of gliding birds to UAVs. Figure 1.5a incorporates all published estimates of avian and UAV aerodynamic efficiency. However, due to the high experimental uncertainty in theoretical predictions and glider-based studies [122], the avian data points were limited to wind tunnel measurements (Fig. 1.5b). Note that live bird studies are affected by the individual bird's behaviour and as a result these avian data points represent a minimum bound on avian aerodynamic efficiency and it is possible that birds are physically capable of more efficient glides[122]. With this reduced data set, there was at least one UAV design that had a higher aerodynamic efficiency than any bird flying within the same supercritical Reynolds numbers sub-regime. This observation is

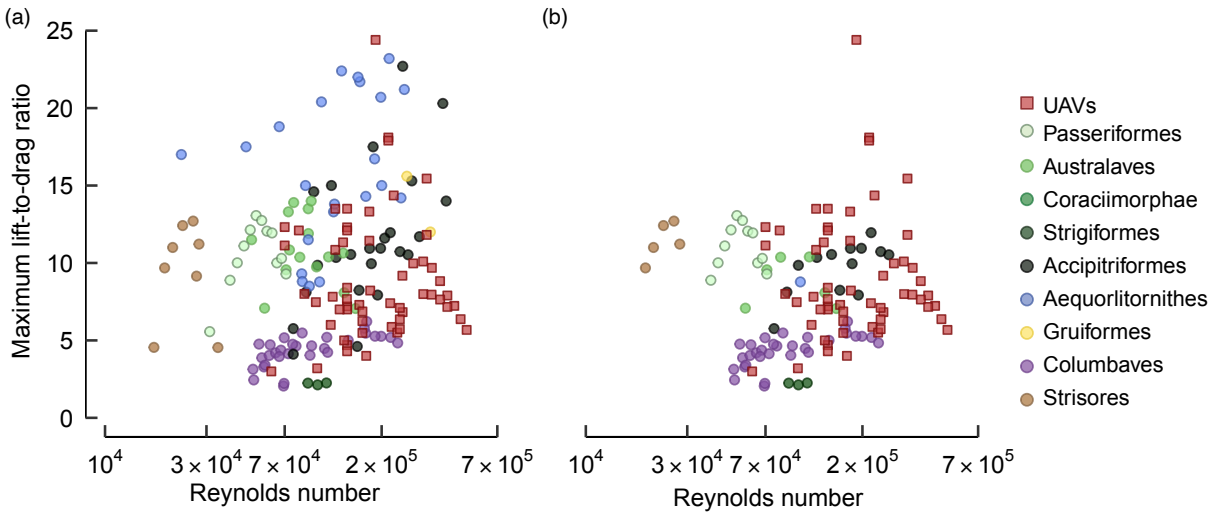

Figure 1.5: **Aerodynamic efficiency of birds compared to UAVs.** (a) All published avian efficiency metrics and (b) avian efficiency measurements from wind tunnel only.

based on the airfoil sub-regimes defined by Table 1.2 with divisions demarcated by the x-axis ticks in Fig. 1.5b [118, 119, 123].

Reconsidering the full dataset in Fig. 1.5a, it remains possible that birds can outperform UAVs operating within supercritical regimes. Note that even with that complete dataset, a UAV (the SBXC) is the most efficient glider [53]. Unfortunately, there is high uncertainty in the published avian theoretical estimates and wind tunnel results are not able to measure birds that are expected to be highly efficient (such as an albatross). Therefore, I cannot state with absolute certainty that birds are more or less efficient than UAVs in the supercritical Reynolds number regimes. At best it can be noted that the efficiency of birds and comparable UAVs in supercritical Reynolds number regimes appear to be within a similar range.

I was only able to identify one comparable UAV with a published aerodynamic efficiency metric operating in the subcritical Reynolds number regimes. This is possibly because the subcritical regimes are dominated by rotary or flapping wing designs. The CICADA UAV (a low-cost, disposable glider) had a maximum lift-to-drag ratio of 3, substantially less than the western jackdaw (*Coloeus monedula*), laggar falcon (*Falco jugger*), and common swift (*Apus apus*) that fly within this same regime (Fig. 1.5b) [39, 54, 92, 124]. Subcritical UAVs are often designed to minimize their wing loading (thus maximizing the wing area and chord for a fixed wingspan) to provide controllability and to operate close to critical Reynolds numbers to allow

sufficient chord length for flow reattachment [80, 125]. However, this leads to reduced aerodynamic efficiencies than could be achieved in the lower subcritical range [118]. In addition to controllability requirements, the CICADA and other fixed-wing UAV designs must satisfy constraints on their geometry such as the need to stack easily within a specified enclosure [54]. Unlike the CICADA, birds can morph their wings to both adjust their stability characteristics and fold their wings flat to their body when needed. It is likely that birds' adaptable wing geometry allows geometric and stability constraints to be satisfied without needing to sacrifice performance when flying in these subcritical regimes.

In all, although this literature review suggests that there are many exciting discoveries yet to be made about avian aerodynamic efficiency, my goal is to begin by analyzing the characteristics of bird flight that readily outperform comparable UAVs: maneuverability and adaptability.

1.5 How birds morph their wings

Multiple studies have identified that bird's ability to morph the shape of their wings allows adaptable and maneuverable flight [39, 85, 127–129]. Birds can morph their wings both passively and actively to adjust aerodynamic forces and moments in flight. Active wing morphing is realized by actuating the skeletal joints, predominately the shoulder, elbow, wrist, and digits (Fig. 1.6) [32, 126, 128, 130]. A bird's wing joints are homologous to other tetrapod (four-limbed animal) forearms including the human arm [131]. However, unlike our arms, the range of motion of a bird's elbow and wrist is often constrained at higher extension angles [126, 128]. This constriction was historically explained as being a result of a planar four-bar linkage system (parallelogram or "drawing parallels") [132]. However, a recent study on pigeons identified that two additional linkages were required to properly replicate the observed out-of-plane effects of wing morphing, resulting in a non-planar six-bar linkage [133]. Under this improved linkage model, the coupled motion of the elbow and wrist are prescribed while the digit and shoulder joints operate independently from the rest of the linkage. Within their available range of motion, birds use muscular control to actuate their skeleton and realize a wide range of distinct, and often non-planar, wing shapes in flight [126, 128].

The majority of the wing surface is formed by the main flight feathers (also known as

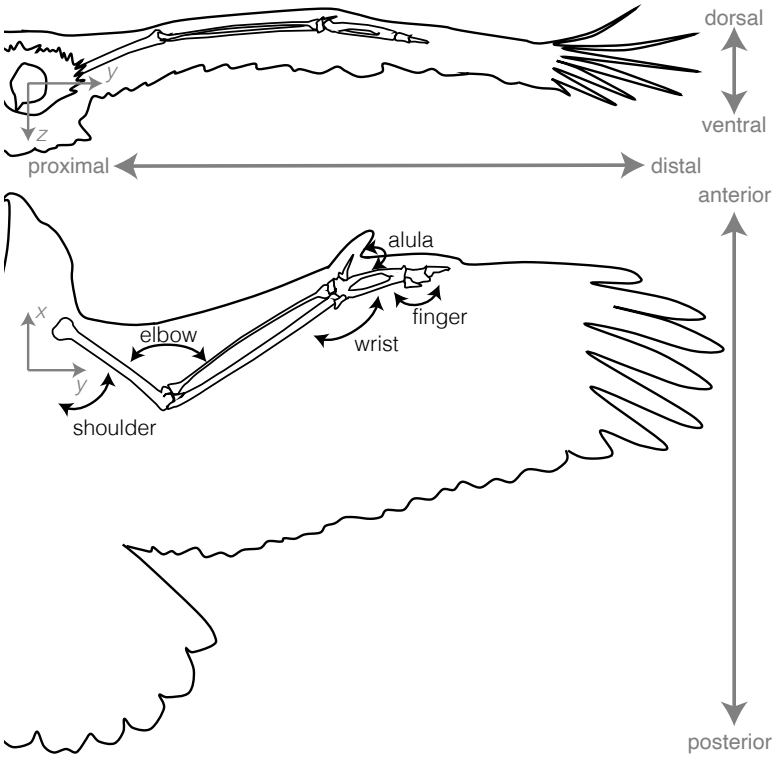

Figure 1.6: **Key bird wing morphing parameters.** Simplified view of a bird's wing highlighting the skeletal structure which can be actively controlled by activating the wing muscles. The skeletal drawing is adapted from [126].

remiges) including the primary and secondary feathers. They are attached to the bones and each other via a complex system of ligaments, tendons, and muscles [134]. Primaries are distributed along the length of the carpometacarpus and onto the digits. They are numbered from the most proximal to the most distal feather (Fig. 1.7, I - X). Secondaries are attached to, what are effectively, protrusions on the ulna and are numbered from the most distal to the most proximal feather (Fig. 1.7, 1-10). Different species of birds have different amounts of primary and secondary feathers.

The simplification of modeling the wing as a six-bar linkage does not capture that the elbow and wrist joints do have some capacity for rotation about three degrees of freedom: extension/flexion, pronation/supination (twist) and elevation/depression [126], although each joint's range of motion varies based on the species [126, 130, 135]. The shoulder joint is also important in bird flight and results in a solid body rotation of the wing shape about the root. This joint is discussed within multiple chapters of this work, but future directed studies on the

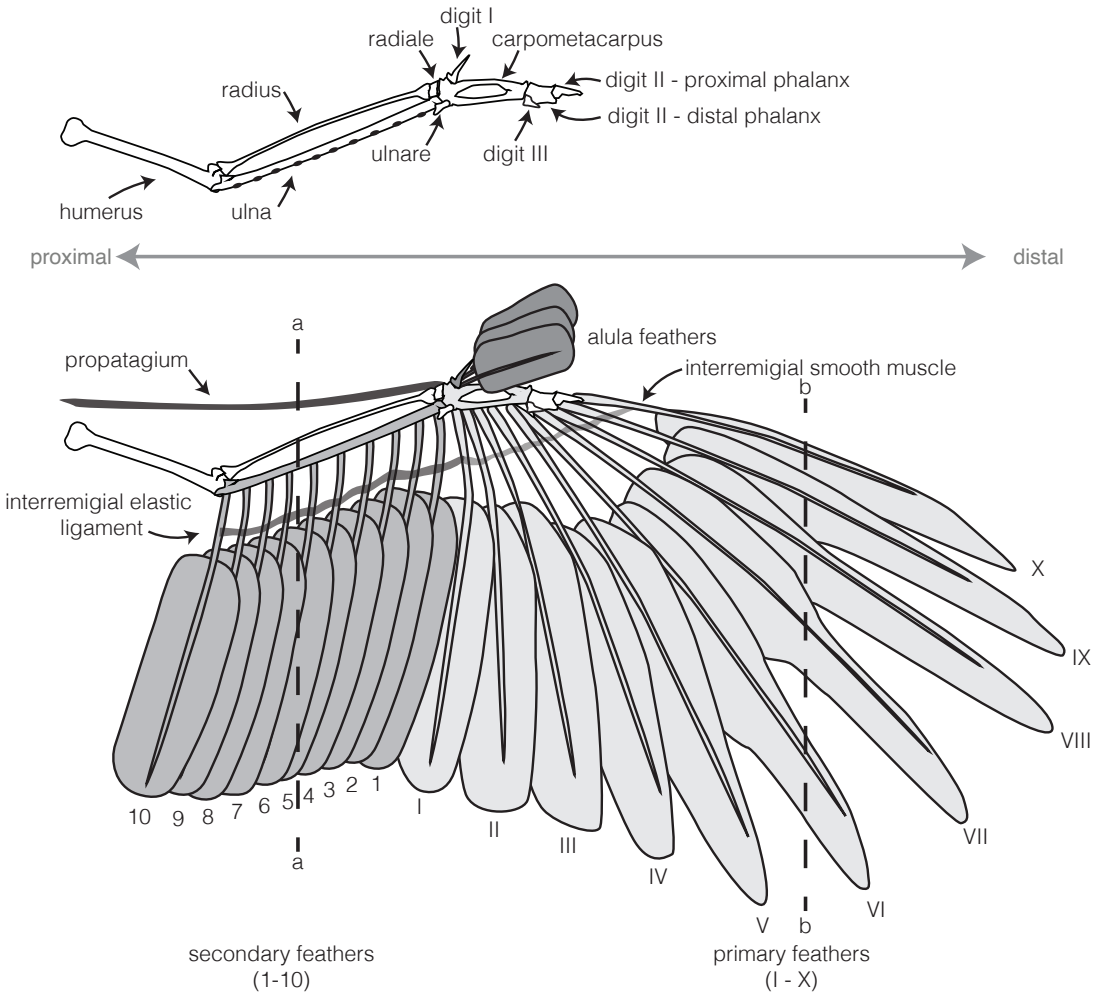

Figure 1.7: **Simplified anatomical drawings of a bird's wing bones and feather attachments.** Drawing is based on a turkey vulture (*Cathartes aura*). The musculature is not included for clarity. This anatomical view is for reference only, as there is a lot of diversity in bone and feather shapes. The proximal airfoil shape (dashed line, a-a) differs substantially from the distal airfoil shape (dashed line, b-b).

role of the shoulder joint in avian flight are required. In addition, birds can actively control two of their digits: digit I (a thumb-like appendage) and digit II (a pointer-finger-like appendage) (Fig. 1.7) [133–135]. Here, I focus on the role of the elbow and the wrist predominately as they have been shown to be responsible for the majority of wing shape variation in birds [122, 126].

1.6 Maneuverability vs. stability

Avian flight capabilities are, in part, permitted by neurological control [130, 136] combined with the physical capability to dynamically morph their wing or tail shape [127, 137]. In this thesis, I focus on deciphering the role that wing morphing plays in adaptable and maneuverable bird flight. Although I have defined maneuverability as the ability to adjust the velocity vector direction and/or magnitude [19, 20], it is still challenging to quantify maneuverability with a single metric. Therefore, throughout this work I leveraged another flight trade-off, that between stability and maneuverability.

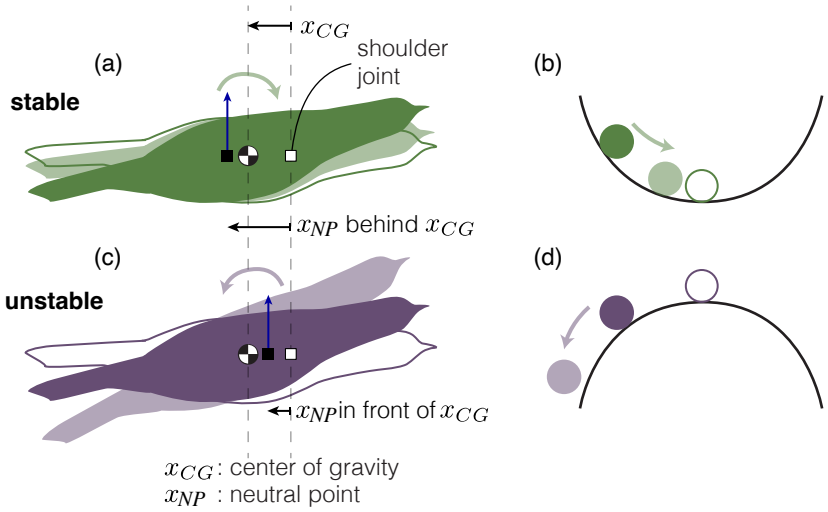

Figure 1.8: **Simplified diagram of static stability responses.** (a) A stable flyer tends to return back towards it's trim condition after a perturbation, similar to (b) a ball on a concave surface. (c) In contrast, an unstable flyer tends to move even further from it's trim condition after a perturbation, similar to (d) a ball on a convex surface. The outlined shapes represent the equilibrium condition for both the bird and the ball.

Flight stability traditionally quantifies a flyer's response to being disturbed (or perturbed) from an equilibrium condition, also known as trimmed flight. Stability is evaluated by considering both the static and dynamic response after a flyer has been disturbed from it's initial trim condition. A gust is a common example of a flight disturbance. A flyer is statically stable if, after a disturbance, the flyer initially tends back towards it's trim condition (Fig. 1.8a). This response is similar to a ball after being nudged when it is resting on a surface that is concave (Fig. 1.8b). A flyer is statically unstable if, after a disturbance, the flyer tends to move even

further from the initial condition (Fig. 1.8c), like a ball on a convex surface (Fig. 1.8d).

Static stability is often investigated for either the longitudinal or lateral degrees of freedom. This differentiation can be made for a rigid aircraft with six degrees of freedom that is given the constraints of symmetric flight and undergoes only small disturbances. In this case, the longitudinal and lateral degrees of freedom can be decoupled [138, 139]. Throughout this work, I make these assumptions to permit a focus on the longitudinal degrees of freedom specifically. Longitudinal static stability requires that the center of gravity of the flyer is behind the neutral point of the flyer (Fig. 1.8a). The neutral point is the location where the pitching moment is independent of the angle of attack. Of note, static stability is independent of time and is a necessary, but insufficient condition for complete stability.

To be completely stable, a flyer must also be stable over time, often called dynamic stability. This is the case if, after a disturbance, the flyer eventually returns to its trim condition without the use of any control inputs. The path followed after the disturbance can be quantified by calculating the eigenvalues of the resultant dynamic system [138, 139]. Once the eigenvalues (λ) are known the natural frequency and damping ratio can be calculated as:

$$\begin{aligned} \lambda &= (re) \pm j(im) \\ \omega &= \sqrt{re^2 + \ im^2} \\ \zeta &= \frac{-re}{\omega} \end{aligned} \tag{1.2}$$

Where re and im represent the real and imaginary parts of each eigenvalue respectively.

Whether the dynamic response is stable depends on the sign of the eigenvalue's real component. If the real component is positive, the flyer is unstable (Fig. 1.9c and f). If the real component is negative, the flyer is stable (Fig. 1.9a and d). If the eigenvalue has no real component, the response will be considered neutrally stable. Neutral stability indicates that there would not be any amplification or decay of the natural frequency amplitude that resulted due to a disturbance (Fig. 1.9b and e). Note that if the eigenvalue has no imaginary component, the response will be steady and non-oscillatory (Fig. 1.9d, e, f). However, most commonly in aircraft analyses the roots will be a complex pair, which signifies an oscillating response after a disturbance (Fig. 1.9a, b, c). The dynamic response associated with each eigenvalue

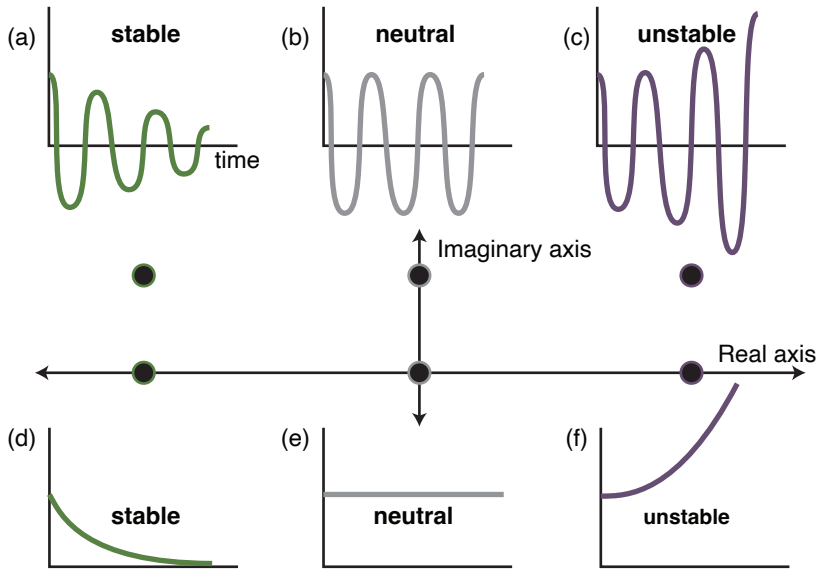

Figure 1.9: **Simplified diagram of dynamic stability responses.** The dynamic stability of a system is quantified through the eigenvalues, which can be plotted on the real (x) and imaginary (y) axes. If the eigenvalues are complex pairs, the response is oscillatory. The stability of the system depends on the sign of the real component, where (a) negative is stable, (b) zero is neutrally stable, and (c) positive is unstable. Note only the complex pair with a positive imaginary value is shown in this diagram. If the eigenvalues are real numbers, the response is steady and non-oscillatory. Again, the stability depend on the sign of the real number. The response is (d) stable if the root is negative, (e) neutrally stable if the root is zero, and (f) unstable if the root is positive.

of a linear system can be superimposed to obtain the complete response of the aircraft. For example, the longitudinal response of rigid body aircraft undergoing small disturbances will be characterized by four eigenvalues, often composed of two complex pairs.

A stable flyer inherently develops restorative moments to return to its trim position after a disturbance, whether that disturbance is accidental or purposeful. However, to perform a maneuver requires a purposeful departure from the trim condition and thus a stable flyer must generate sufficient moments that overcome the inherent restorative moments. These restorative moments lead to the expected trade-off between stability and maneuverability. It is for this reason that fighter aircraft, which prioritize maneuverability, are designed to be more unstable than passenger aircraft, which prioritize safety and fuel efficiency.

The advantage to approaching maneuverability through a stability-based analysis is that there are well-established methods to evaluate the static and dynamic stability of an aircraft

[138–140]. These approaches are implemented and discussed in detail throughout this work.

1.7 Dissertation outline

Within this thesis, I investigated the effects of manipulating the avian elbow and wrist on longitudinal gliding flight stability. This analysis was approached as three core components that support and reinforce each other. Each component is covered in a separate chapter.

First, Chapter 2 investigates the aerodynamic characteristics of the gull wing across it's complete range of flexion and extension of the elbow and wrist. Using an experimentally validated, open source numerical lifting line method, I calculated the lift and pitching moment associated with over 1000 real gull wing shapes. With the outputs from this study, I used statistical techniques to investigate the adaptive control permitted by using different combinations of the elbow and the wrist to morph the wing. This revealed that there is an extension trajectory that acts similar to a conventional flap by linearly increasing the lift and pitching moment without affecting the longitudinal static stability. A separate extension trajectory was found to linearly decrease the static stability with negligible effects to the lift and pitching moment. These two trajectories highlight the broad range of possible control that could be gained by implementing gull-inspired elbow and wrist joints in a morphing wing UAV design. Notably, I found that none of the gull wing configurations could trim at the set shoulder angle. This study focuses on a single species of gull and was limited to discussing the stability characteristics with the pitching moment origin at the shoulder joint since there was no existing method to estimate the center of gravity of a bird. A version of this chapter has been published [141].

Next, Chapter 3 addresses the lack of knowledge on inertial characteristics of birds with a comparative analysis of 22 bird species. In this chapter, I developed an open source software (AvInertia) that uses classic mechanical techniques to estimate the center of gravity and moment of inertia tensor for any flying bird with any wing configuration. With the output inertial characteristics and the aerodynamic results from Chapter 2, I investigated the complete static stability of these birds and found that modern birds have the capacity to shift between longitudinally stable and unstable flight. Further, the comparative approach allowed me to implement an evolutionary analysis, which revealed evidence of evolutionary pressures acting to main-

tain this capability to shift between stability modes. This work focused specifically on static stability characteristics. A version of this chapter has been published [142].

Finally, Chapter 4 combines the aerodynamic approach introduced in Chapter 2 with the inertial approach introduced in Chapter 3 to quantify the complete dynamic stability of an individual gull. This analysis accounts for the different wing configurations that can be achieved by manipulating the gull's shoulder, elbow, and wrist angle. I included a variable shoulder angle in this work to enable a trimmed flight condition. Of the identified configurations that could trim, those with high wrist angles had non-oscillatory, unstable responses. Within the stable configurations, I found strong interactive effects between the shoulder, elbow, and wrist angles. Compared to UAV metrics, the gull wing configurations are expected to be controllable by a human pilot, albeit with a heavily damped phugoid mode. This heavily damped response indicates that to effectively perform a given maneuver a gull may need to morph into an unstable configuration.

In all, this thesis provides the first complete investigation of the longitudinal stability associated with morphing the avian elbow and wrist. These analyses were completed in a manner that allow for comparison to traditional aeronautical metrics, which in turn allows the identification of the aspects of bird flight that may best enhance future UAV designs.

Chapter 2

Adaptive Control with Gull Wing Joints

Science is fun. Science is curiosity. We all have natural curiosity. Science is a process of investigating. It's posing questions and coming up with a method. It's delving in.

– Sally Ride

2.1 Summary

Birds dynamically adapt to disparate flight behaviors and unpredictable environments by actively manipulating their skeletal joints to change their wing shape. This in-flight adaptability has inspired many uncrewed aerial vehicle (UAV) wings, which predominately morph within a single geometric plane. In contrast, avian joint-driven wing morphing produces a diverse set of non-planar wing shapes. Here, we investigated if joint-driven wing morphing is desirable for UAVs by quantifying the longitudinal aerodynamic characteristics of gull-inspired wing-body configurations. We used a numerical lifting-line algorithm (MachUpX) to determine the aerodynamic loads across the range of motion of the elbow and wrist, which was validated with wind tunnel tests using 3D printed wing-body models. We found that joint-driven wing morphing effectively controls lift, pitching moment and static margin, but other mechanisms are required to trim. Within the range of wing extension capability, specific paths of joint motion ("trajectories") permit distinct longitudinal flight control strategies. We identified two unique trajectories that decoupled stability from lift and pitching moment generation. Further, extension along the trajectory inherent to the musculoskeletal linkage system produced the largest changes to the investigated aerodynamic properties. Collectively, our results show that gull-inspired joint-driven wing morphing allows adaptive longitudinal flight control and could

promote multifunctional UAV designs [141].

2.2 Background

A bird can begin its day foraging in a slow glide, suddenly needing to evade a predator, only to later fly home battling an incoming storm. The adaptability demonstrated by birds is in part due to their ability to morph the shape of their wings, both actively and passively [85, 127, 137, 143]. Previous research has shown that active wing morphing allows birds to dynamically adapt their aerodynamic performance and stability characteristics in response to changing flight conditions or requirements [127, 128]. In comparison, fixed-wing UAVs are often designed to satisfy specific functions, such as high altitude surveillance or long endurance flights, and efficient operation is limited to their intended mission parameters [6]. The adaptability offered by avian wing morphing is highly desirable for UAVs as it may broaden the efficient operational range, reduce operating costs as well as offer enhanced or novel capabilities [6, 143–145]. In addition, UAVs often face aerodynamic control challenges including the need to adapt to variable environmental conditions [146] or maneuver through complex territories [147], while birds complete similar tasks with apparent ease. Therefore, it is of no surprise that as engineers strive towards the objective of an adaptive, multifunctional UAV, bird wings have directly and indirectly inspired many morphing wing designs [6, 29–33].

The majority of current engineered morphing wings adjust their wing geometry discretely within one or two planes such as span, sweep, dihedral, etc. [29, 30, 32, 33]. In contrast, bird wings are composed of an underlying musculoskeletal system that can be approximated as a non-planar six-bar linkage system [133]. When the applicable muscles are activated, the non-planar musculoskeletal linkage causes three-dimensional (3D) changes to the overall wing geometry [126, 128, 133]. Active manipulation of only two skeletal joints, the elbow and wrist is responsible for the majority of this wing shape change (Fig. 2.1) [126, 128]. These joints have three degrees of freedom i.e. the ability to extend/flex, pronate/supinate and elevate/depress [126]. However, within gliding flight extension/flexion dominates the range of motion and thus we have limited our study to focus only on the range of motion of extension and flexion for the elbow and the wrist (hereafter referred to as “joint-driven wing morphing”). Therefore,

in this work the elbow and the wrist represent an approximated minimum set of coordinates that is required to define the overall wing shape. In this case, traditional geometric properties including distributions of wing twist, sweep, dihedral and the final wingspan can be approximated as functions of the joint positions [128, 148]. Further, these non-planar wing shapes likely have aerodynamic characteristics that differ from comparable planar wing aerodynamic theory [122], as highlighted by the Hyper Elliptical Cambered Span (HECS) wing inspired by gulls, which had improved aerodynamic efficiency (higher lift-to-drag ratio) compared to an equivalent planar wing [149].

Despite the physical differences, no engineered morphing wing designs have implemented biologically accurate joint-driven wing morphing. This discrepancy is likely due to the many challenges associated with implementing a non-planar morphing wing including complex manufacturing methods as well as additional mechanism weight and structural rigidity considerations [6]. In addition, because we cannot assume that a bird's wing has been optimized for flight [150], it follows that we cannot assume that a biologically accurate morphing wing will provide any advantage over a planar morphing wing. This leads to the main question of this first chapter: does avian-inspired joint-driven wing morphing provide sufficient aerodynamic benefits to warrant implementation in a future UAV wing design?

To address this question, we investigated the benefits of gull-inspired joint-driven wing morphing by quantifying longitudinal aerodynamic stability and control, which are critical for any successful flight, be it high-altitude surveillance or evasive maneuvers [137, 138, 140]. We assumed a symmetric glider with no sideslip, to permit longitudinal (pitch, motion in the x-z plane, Fig. 2.1) and lateral (roll and yaw, motion in the x-y or y-z planes) components to be decoupled [140]. In this work, longitudinal control refers to a morphing wing's ability to actively adjust its generated lift force and pitching moment. Traditional aircraft can control lift through wing flap deflections and the pitching moment through elevator deflections [138, 140]. In addition to longitudinal control, we considered the effects of joint-driven wing morphing on longitudinal stability and balance. Longitudinal stability is the tendency of an aircraft to return to its equilibrium after an external disturbance, which requires an evaluation of both the static (initial) and dynamic (time-dependent) response [140]. Here, we focused solely on static stability, a necessary but insufficient condition for full stability. Finally, longitudinal balance is

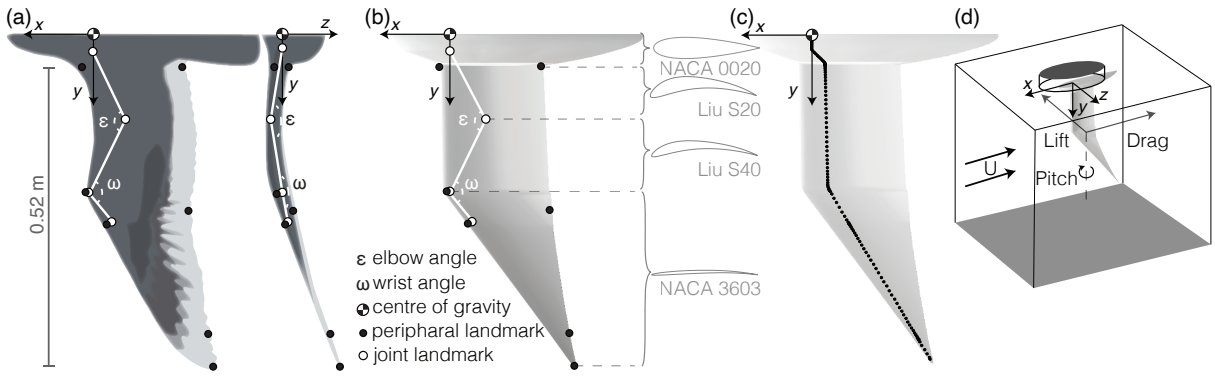

Figure 2.1: **Gull wings inspired our analyses of how avian joint-driven wing morphing affects longitudinal aerodynamic control, stability and balance.** (a) Wings from gull cadavers (n = 3) were manually manipulated throughout the range of motion of the elbow and wrist while tracking the 3D position of seven peripheral landmarks (black points) and four joint landmarks (white points). (b) The identified wing shapes were simplified using linear approximations between the peripheral landmarks. Four airfoils were used to create the wing-body configurations. (c) The simplified wing shapes were reflected about the x-z plane and investigated using MachUpX and cosine clustering to distribute the control points along the span. (d) To validate the numerical results, nine wing shapes were 3D printed and tested in a 2ft-by-2ft low-speed wind tunnel.

the ability for a glider to fly at an equilibrium, also known as trimmed flight.

To quantify the longitudinal control, stability, and balance associated with gull-inspired joint-driven wing morphing, we first identified the 3D simplified wing shapes associated with the extension and flexion of the elbow and wrist for hybrid glaucous-winged (*Larus glaucescens*) $\times$ western (*Larus occidentalis*) gulls (n = 3, Fig. 2.1a). We selected gulls as our study species because their non-planar wing shape is known to be actively controlled by elbow and wrist manipulation [128]. In addition, gulls are a good model species for multifunctional UAVs as they are generalist flyers, using a wide variety of flight styles from steady glides to sudden maneuvers [112, 151]. Next, we aligned and simplified each extracted wing shape (n = 1031) and connected these wings to a gull-shaped body (Fig. 2.1b). With each final wing-body configuration, we predicted the aerodynamic properties using MachUpX, a low-order numerical general lifting-line model (Fig. 2.1c) [152–154]. We validated the outputs from MachUpX with experimental wind tunnel measurements on 3D-printed half-span equivalent wing-body models (Fig. 2.1d). Finally, we investigated four quasi-steady joint extension trajectories within the range of motion that could be implemented to improve the adaptability of a gull-inspired joint-driven

morphing UAV wing.

2.3 Methodology

2.3.1 Determining the wing-body configurations

Wings from gull cadavers (n = 3) were manually manipulated throughout their full range of elbow and wrist extension and flexion while filming eleven key landmarks with three high speed cameras. Seven landmarks on the wing periphery (black points, Fig. 2.1a) provided an outline of the overall wing shape through the range of motion and four landmarks on the wing joints (white points, Fig. 2.1a), allowed us to calculate the elbow and wrist angle associated with each wing outline. The videos were digitized using DLTdv5 software [155] to return the 3D position of each landmark. For a detailed methodology on how the 3D landmarks were obtained please refer to Harvey et. al [128].

The final extracted 3D landmarks were reoriented using a custom R script to align the wrist joint with the humerus head on the y- and z-axis (Fig. 2.1b). We defined 0° angle of attack by rotating the wing about the y-axis until the tip of the first secondary feather (S1) was aligned with the wrist joint along the x-axis. Next, we exported the aligned landmarks into a custom Python script to ease interfacing with MachUpX and limited the configurations to those with elbow and wrist angles above the minimum angles used *in vivo* by gliding gulls [128]. Next, the wings were segmented along the x-axis at each peripheral landmark. For each segment, the custom script returned simplified leading and trailing edge points, and a value of sweep, dihedral, and twist within that segment. The last 5% of the wing segment span was linearly blended into the next segment to avoid sharp changes in wing geometry. These geometric properties were selected to minimize error between the true peripheral landmarks and the final simplified wing shapes. The maximum summed error for all landmarks was found to be 2.1mm.

There are a few key assumptions on the final wing shapes. First, we assumed that throughout elbow and wrist extension and flexion, the digits (including the alula) remain fixed. Next, we elected to not consider the capability to elevate/depress or supinate/pronate along joints within the wing or to adjust overall wing position via rotation at the shoulder joint. Addition-

ally, we neglected wing porosity, roughness, and flexibility to isolate the effects solely due to the shape change created by joint-driven wing morphing. Due to these assumptions and the alignment routine, the final wing shapes are not necessarily representative of an in-flight configuration used by live gulls.

Each final wing shape was attached to a gull-inspired body. We selected a NACA0020 airfoil based on an estimated body length (41cm) and body height that was estimated using an allometric relationship with a body mass of 0.91kg [156, 157]. The shoulder joint was positioned at the quarter-chord of the body. The body width and position of the shoulder joint along the y-axis (Fig. 2.1b) was determined from allometric relationships with the same body mass [157]. To create an avian-like body shape, we reduced the body chord from a maximum at the body's center to the wing root chord length at the body's edges using a cosine distribution.

For each wing-body configuration, we quantified a few traditional geometric properties including the total and projected wing area, as well as wing tip twist, sweep, and dihedral (Fig. 2.5c). The total wing area is the total wing-body area and the projected wing area is the wing-only area projected onto the y-x plane at 0°, the body projected area remains approximately constant. The wing tip twist, dihedral and sweep values were calculated for the most distal wing segment within our custom Python script. Note that all tested wing shapes had wing tips with some degree of backwards sweep and anhedral.

2.3.2 Airfoil properties

Next, we selected three airfoils to distribute along the wingspan. We extracted two airfoils from a previously published scan of a gull wing at 20% (Liu S20) and 40% (LiuS20) span (Fig. 2.1b) [158]. As the species was not identified in that study, we assumed that the airfoil shape is similar between different gull species. We defined the airfoils for each segment based on the locations of the skeletal joints as illustrated in Fig. 2.1b. For segments more distal than the wrist joint, we assigned a NACA 3603 airfoil because the scan did not capture the wing after 77.2% span [158]. We selected the NACA 3603 after compiling a list of measured distal avian airfoils [159–161]. All aerofoils were linearly blended to create a smooth wing surface within the MachUpX framework [152].

MachUpX requires the airfoil performance data (lift, drag and pitching moment) at an ap-

propriate Reynolds number as inputs. We used XFOIL to predict the 2D airfoil properties for each of the four selected airfoils used on the wing and body [162]. Following XFoil's implementation of the e^n method for transition prediction, we assumed a critical N-factor at transition of 9. This value is commonly used to model the turbulence intensity in an average wind tunnel. We estimated the range of Reynolds numbers that would be experienced by each airfoil and stored each data set separately. For Reynolds numbers above 100,000 we incremented by 50,000 (to a maximum of 300,000 on the body) and below 100,000 we incremented by 10,000 (to an enforced minimum of 10,000 on the wing tip). Our custom Python script predicted the Reynolds numbers experienced by each wing segment and selected the closest Reynolds numbers number file for the segment airfoil. This methodology accounts for changes in aerofoil performance at variable Reynolds numbers across the wingspan. MachUpX linearly interpolates the 2D airfoil properties across wing segments from the provided files.

2.3.3 Numerical lifting-line solution (MachUpX)

MachUpX is a Python implementation of the Goates-Hunsaker (G-H) general numerical lifting-line method, which is a modern extension of Prandtl's classical lifting-line theory [152–154]. Within the G-H method, the wing is replaced by a set of horseshoe vortices and Prandtl's lifting-line hypothesis is enforced at a single control point on each vortex to determine the aerodynamics of the wing. Wings are modelled in MachUpX using the quarter-chord distribution of sweep, dihedral, and twist. Multiple spanwise sections can also be used to incorporate viscous effects by allowing for viscous section lift, drag, and moment coefficients. The outputs from MachUpX used in this study are the total forces and moments for a given wing-body configuration. As a low-order numerical method, MachUpX is ideal for quickly performing comprehensive investigations of multi-degree-of-freedom design spaces.

We evaluated the wings as a symmetric full-span configuration at a velocity (U_∞) of 10 m/s to approximate a gull's gliding speed (density (ρ): 1.225 kg/m^3, kinematic viscosity: 1.81×10^{-5} m^2/s) [25, 128]. We specified a grid resolution of 200 cosine clustered vortices for the wing and 60 for the body (Fig. 2.1c). We used MachUpX's non-linear solver with a convergence tolerance of 10^{-6} and a relaxation factor of 1, 0.8, 0.5 or 0.01. Each wing was tested from -10° to 10° in increments of 1°. In total, we had convergence for at least one angle

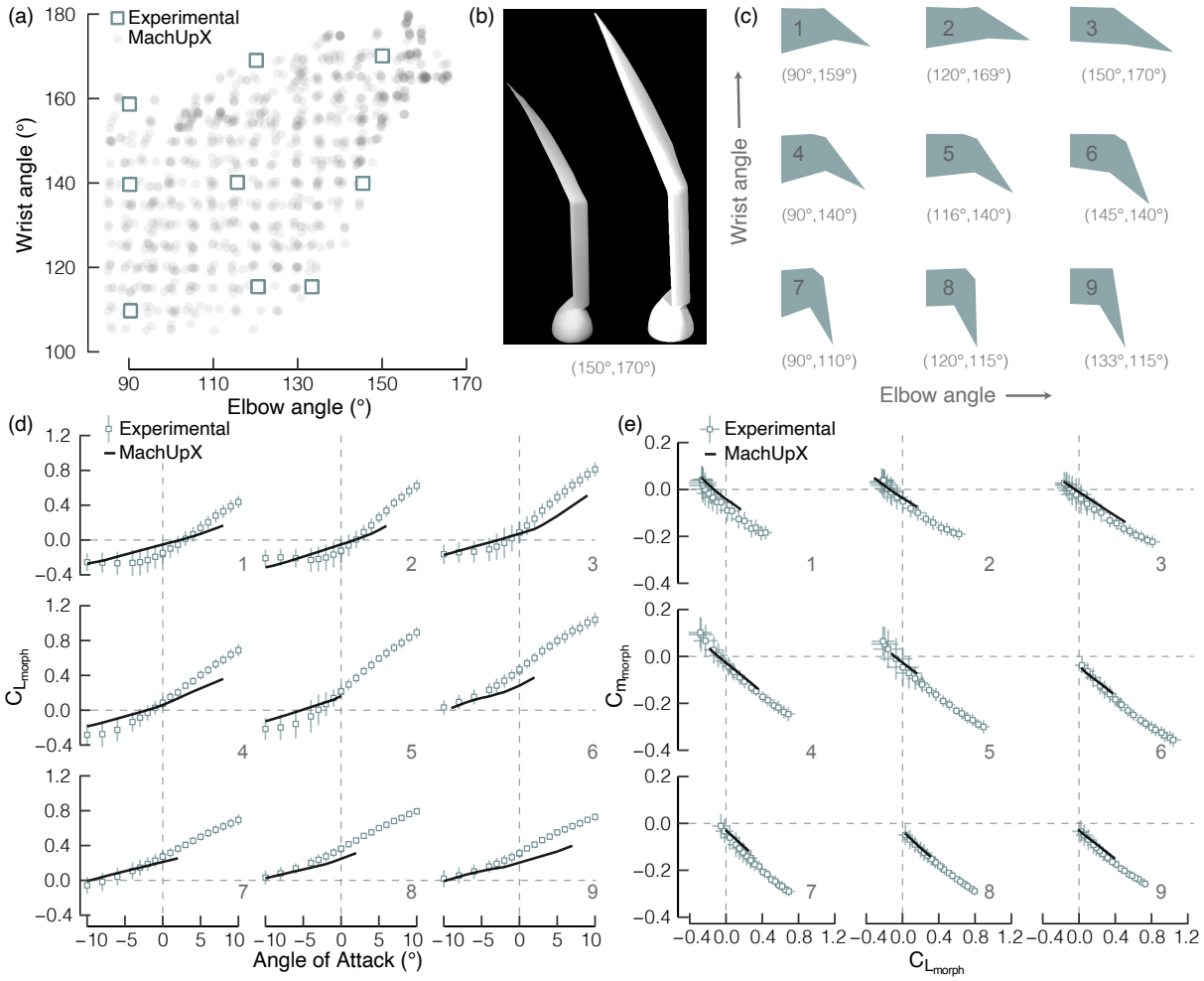

Figure 2.2: **MachUpX effectively predicted the aerodynamic forces and moments for the investigated wing shapes.** (a) The *in vivo* range of motion used by gliding gulls was investigated using MachUpX (n = 1031, translucent gray points; higher-sampled configurations accordingly appear darker) and validated with wind tunnel tests of 3D printed wing shapes distributed across the range (white squares). (b) Experimental wings (photo, left) were tested at an 80% scale from the numerical wings (front view of Fig. 2.1b, right). (c) Planform views of the 3D printed wing shapes corresponding in location/arrangement to the white squares in (a) and the plots in (d) and (e). Wing shapes in (b) and (c) are described by (elbow angle, wrist angle). (d) MachUpX predicted the lift force within the expanded uncertainty range at low angles of attack. (e) The numerical results for lift and pitching moment lie within the expanded uncertainty range on both variables. The error bars represent the expanded uncertainty range, approximately a 95% confidence interval.

of attack for 1031 wing-body configurations with a total of 9720 converged test cases. The majority of the convergence was at lower angles of attack.

We used the MachUpX outputs to investigate the lift and pitching moment for the wing-body configurations. We were not able to investigate the maximum lift produced by each configuration due to the limitations of the numerical method for the complex shapes. Additionally, we did not investigate drag as it was outside the scope of this study, but it likely plays a variable role in avian wing morphing and warrants future investigation. Note that MachUpX predicted the experimental drag within the expanded experimental uncertainty range for all wings except for configurations 6, 7, 8, and 9 (Fig. 2.2c).

To allow comparison between the experimental and numerical lift and pitching moments, we non-dimensionalized the outputs by the dynamic pressure ($\frac{1}{2}\rho U_\infty^2$), maximum total wing area (S_{max}) and maximum wing-body mean chord (c_{max}) for each specimen across all morphed configurations to obtain $C_{L_{morph}}$ and $C_{m_{morph}}$, respectively. These adjusted aerodynamic coefficients allow comparisons across different wing specimens without filtering out the wing area change due joint-driven wing morphing. As there is relatively little information about the location of a bird's center of gravity, we evaluated the pitching moment about the body's quarter-chord (aligned with the shoulder joint); this effectively assumes that the center of gravity is located at the body's quarter chord (Fig. 2.1a).

2.3.4 Wind tunnel study

To validate the numerical results from MachUpX, we 3D printed nine wing-body configurations across the range of motion (Fig. 2.2a, b and c and Fig. 2.3). The wing shapes are identical to those tested in MachUpX due to a feature that outputs the DXF files for a specified wing shape [152]. These files were prepared into a 3D model and 3D printed on a CONNEX500 printer in rigid plastic (VeroWhitePlus). We printed half-span wing-body models at 80% scale to ensure that the largest wingspan only extended to 71% of the tunnel width. The printed wings were lightly sanded to minimize surface roughness.

The final wings were tested in the University of Michigan 2ft-by-2ft low-speed wind tunnel at 12.5m/s (Fig. 2.3). This enforced a constant Reynolds number (Re) between the experimental and numerical tests of approximately 1.4-1.5$\times 10^5$ based on the maximum mean chord for

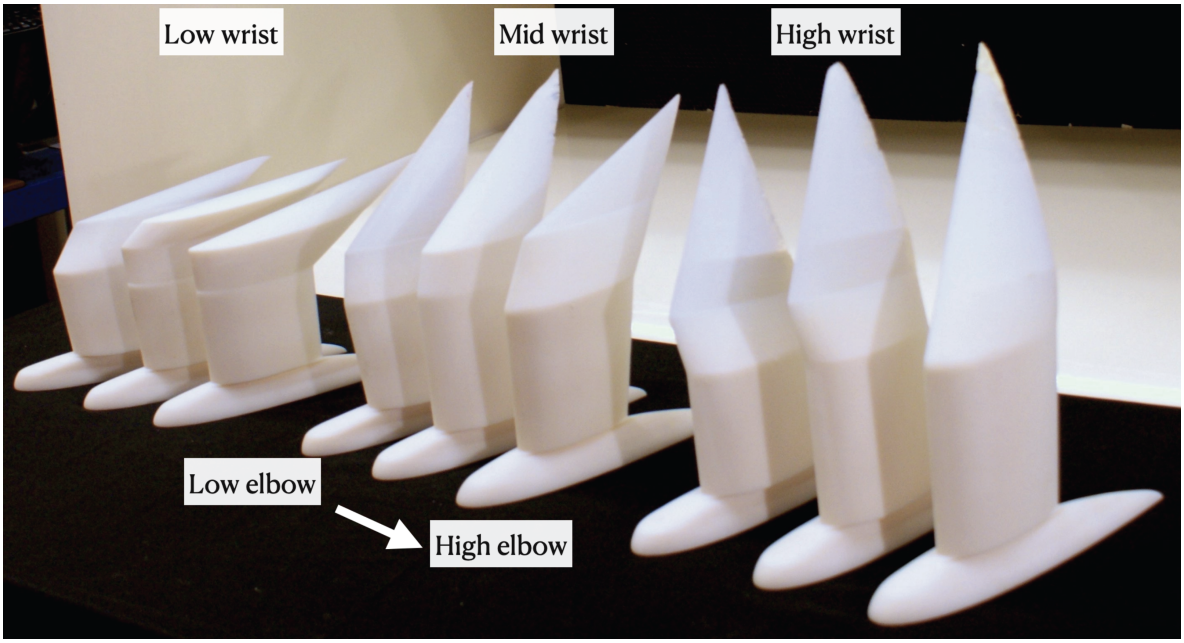

Figure 2.3: **All final 3D printed wings.** (a) Organized from left to right based on Fig. 2.2c as configuration 7, 8, 9, 4, 5, 6, 1, 2, 3.

the wing-body specimen. The wings were mounted to the top of the wind tunnel on a 6-axis load cell (ATI Delta) that sampled at 4kHz for 45 seconds. There was a 0.5-inch gap between the body and the tunnel edge. The load cell was installed on a rotary table (Parker 30012-S) connected to a motor (VEXTA PK266-03B) and a VELMAX motor controller. This installation method used the reflection plane methodology and blockage constraints were neglected due to the minimal size of the wings relative to the tunnel test section [163]. Using a custom MATLAB script, we performed an angle of attack sweep from 0° to 24° (Δ2°), 25° to 1° (Δ2°), 0° to -3° (Δ1°) and -4° to -20° (Δ2°).

To determine the experimental uncertainty, we implemented the definition and procedures outlined in the Guide to Uncertainty Measurement [164] through the R package errors [165]. The calculated uncertainties were multiplied by a coverage factor k = 2 to determine an approximate 95% confidence level on the experimental data and are included as error bars in Fig. 2.2d and e [164].

Finally, to investigate the differences between the wind tunnel and numerical results, we fit a first order linear model to the numerical and experimental results from the nine tested wing shapes. The lift and pitching moment data were the independent variables for the models and

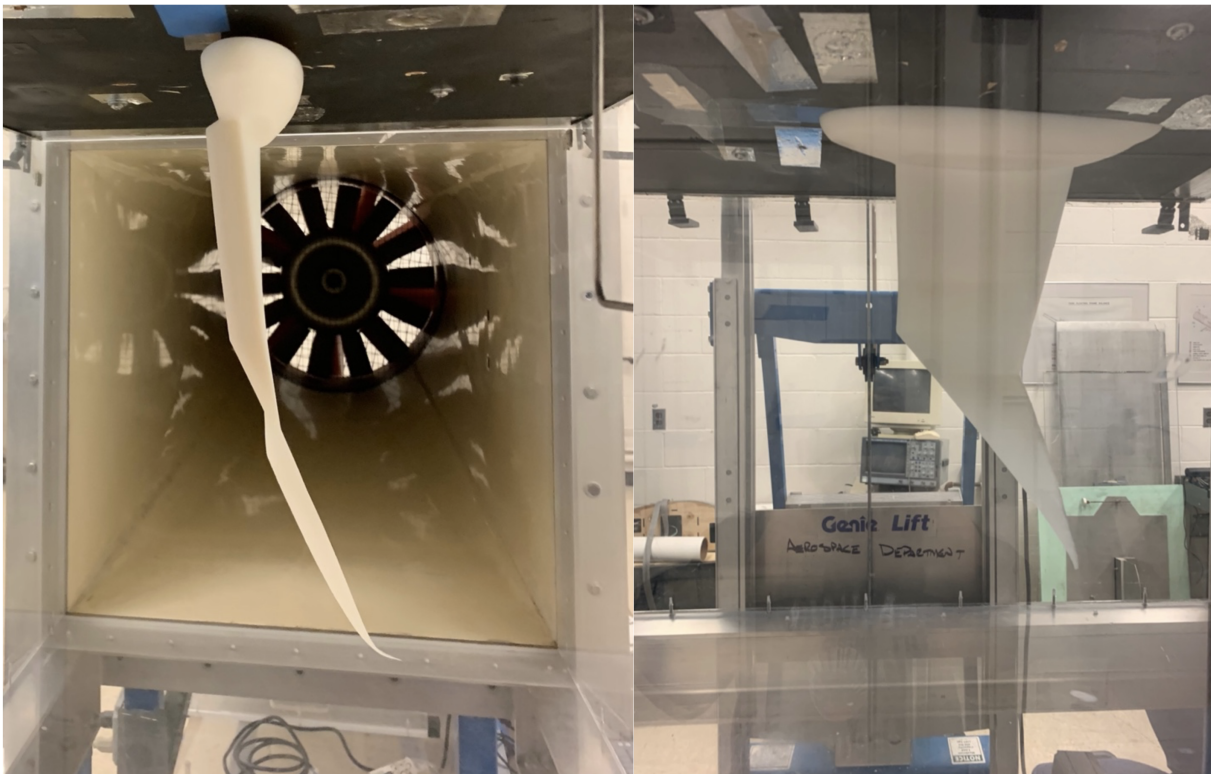

Figure 2.4: **Wings installed in the wind tunnel.** (a) Front view of configuration 6 (Fig. 2.2c) (b) Side view of configuration 1 (Fig. 2.2c).

the elbow, wrist, angle of attack (or lift for the pitching moment model) and method were the dependent variables.

Turbulence intensity

Turbulence intensity is known to affect the aerodynamic performance of wings tested at low Reynolds numbers. We quantified the free stream turbulence in the wind tunnel using a hotwire anemometer (DANTEC MiniCTA with unidirectional 55P11 probe and 55H20 probe support) located at the center line of the tunnel approximately at the location of the wing leading edge. The hotwire was calibrated against a pitot tube at 20 velocities using King's law. This test revealed a base level turbulence intensity of 0.7% of the freestream velocity at the test speed of 12.5 m/s. We found that the turbulence intensity increased towards the edges of the tunnel to approximately 1.8%. It is not simple to directly link the root-mean-square turbulence intensity result to a critical N-factor at transition per the e^n method that is implemented by XFoil [166]. As the experimental results agree well with the numerical results at low angles of

attack, we expect that the role of turbulence was relatively minor. But as the wing approaches stall, turbulent flow in the wind tunnel may have contributed to improved flow attachment and thus higher lift than was predicted by the numerical results.

2.4 Results

2.4.1 MachUpX validation

The MachUpX lift and pitching moment results fell within the expanded experimental uncertainty range for low angles of attack (Fig. 2.2d and e)[164]. Disregarding the expanded uncertainty range, there was an average absolute error in the lift and pitching moment of 0.08 and 0.04 at 0°, respectively. Note that this is largely manifested by MachUpX under predicting the lift for lower wrist angles and higher elbow angles (Fig. 2.2d, configurations 6, 8, and 9). By 5°, the error in both metrics more than doubled. We found that there was no significant effect of methodology (experimental or numerical) on the predicted coefficient of regressions for either the elbow or the wrist. However, there was a significant effect of methodology (p-value < 0.001) on the predicted coefficient of regression for the angle of attack for both the lift and pitching moment models. Specifically, at high angles of attack MachUpX either did not converge, or under predicted the magnitude of lift and pitching moment, likely due to more stalled regions. Informed by these outcomes, the rest of our analyses were limited to angles of attack less than 5°.

2.4.2 Lift force and pitching moment production

With the outputs from MachUpX, we evaluated the lift and pitching moment at a constant 0° angle of attack for all wing-body configurations (Fig. 2.5a and b). We found that the majority of the configurations produced a negative (nose-down) pitching moment and a positive lift force. Figures 2.5a and b reveal that wings with high elbow and low wrist angles had the highest lift and lowest pitching moment, representing the highest absolute loading condition. We used the R package GGally [167] to determine the normalized values of the wing tip geometry, wing area parameters (that were first normalized for each specimen's maximum wing area) and

aerodynamic forces and moments as shown in Fig. 2.5c. Unexpectedly, we found that these highly loaded wing-body configurations did not have the highest wing area (total or projected) but instead had the most positive twist angle at the wing tips (Fig. 2.5c).

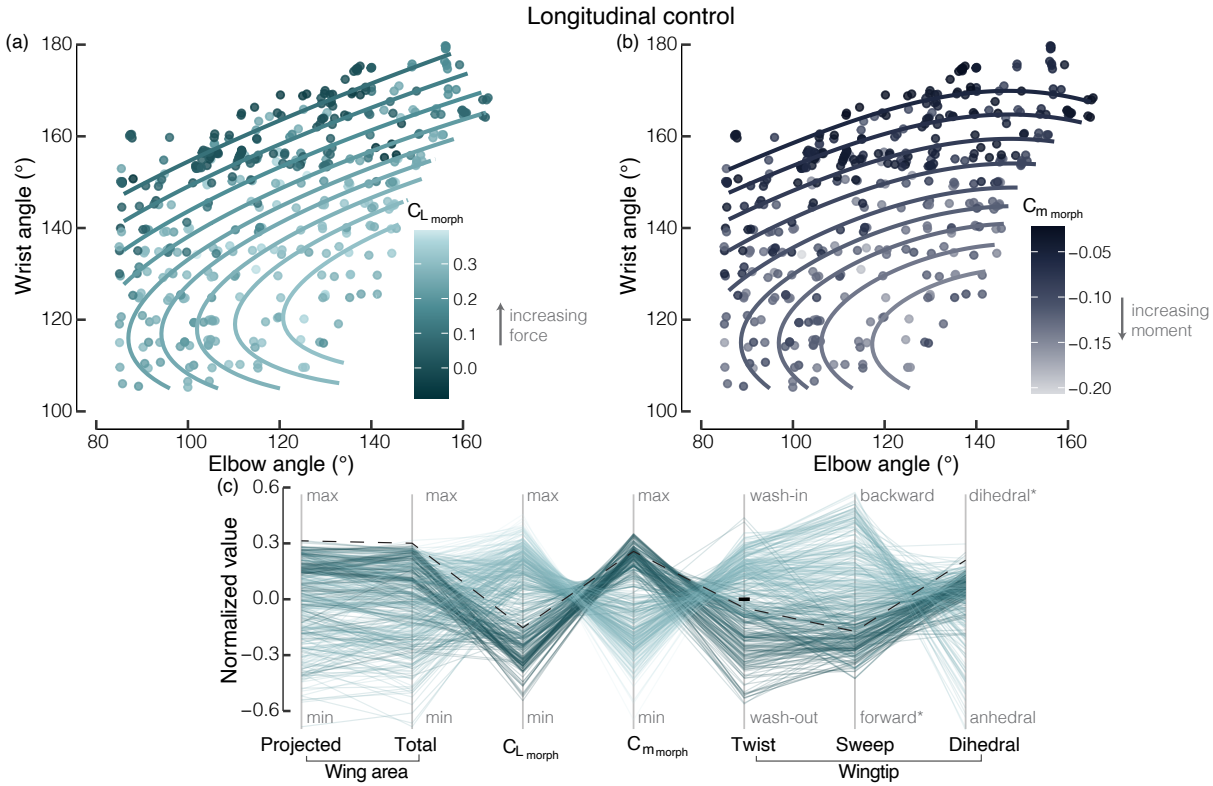

Figure 2.5: **Joint-driven wing morphing provides a reliable method to control the lift and pitching moment.** (a) and (b) Constant lift and pitching moment contour lines overlaid on the numerical results at 0° angle of attack (n = 414) highlight a region of high magnitude lift and pitching moment. (c) Normalized geometric properties, centered on 0° twist angle (black line). The black dashed line represents the wing configuration with the maximum projected wing area. The color scheme is based on the normalized value of $C_{L_{morph}}$.

Positive twist known as wash-in, occurs when the wing tips are at a higher angle of attack than the wing root. Traditional aircraft are designed with wash-out so that the wing root will stall before the wing tip, which improves the handling characteristics of the aircraft [168]. The importance of twist in lift and pitching moment production is supported by a previous experimental study that demonstrated that active wing twist morphing alone provides effective longitudinal control of a tailless aircraft [169]. For the tested configurations, we found that wash-in was associated with a highly swept wing while the less swept (extended) wings exhibited wing tip wash-out. Although wing tip twist was a good predictor of the developed

forces and moments, models informed by the elbow and wrist also successfully predicted the developed lift and pitching moment.

To quantify and visualize the longitudinal control characteristics of the wings from the MachUpX outputs, we fit linear mixed effects models with an interaction term between all the first order fixed explanatory variables to $C_{L_{morph}}$ and $C_{m_{morph}}$. The fixed explanatory variables included the elbow and wrist angle for both models, and the angle of attack for the lift model which was replaced with $C_{L_{morph}}$ for the pitching moment model. In addition, we included the wing specimen identification number as a random effect in each model. Higher order terms on each explanatory variable were included and the final polynomial forms were selected using Akaike Information Criterion (AIC) to compare the weights of each model. The goodness-of-fit of a linear mixed effects model can be assessed through the marginal R^2, which quantifies the variance explained by the fixed effects and the conditional R^2, which quantifies the variance explained by the full model [170]. We calculated the marginal and conditional R^2 using the R package MuMIN [171]. Both the lift and pitching moment models fit our numerical results well. The lift model had a marginal R^2 of 0.81 and a conditional R^2 of 0.90 while the pitching moment model had a marginal R^2 of 0.97 and a conditional R^2 of 0.98. The good model fits suggest that an engineered joint-driven morphing wing could provide a reliable method for controlling the lift and pitching moment in flight, similar to twist control.

Our results have important consequences for estimations of aerodynamic forces on live gliding birds. Specifically, the wing area may not be an effective metric to differentiate between the lift and pitching moment produced by different wing shapes used by the same bird (Fig. 2.2c). Instead, if they can be obtained the wing tip twist and sweep angle can provide improved metrics.

Next, we assessed longitudinal balance and stability using the pitch-stability derivative (slope) and zero-lift pitching moment (y-intercept) from the linear model:

$$C_{m_{morph}} = \frac{dC_{m_{morph}}}{dC_{L_{morph}}} C_{L_{morph}} + C_{m_{morph,L=0}} \tag{2.1}$$

A flyer is statically stable if the pitch-stability derivative is negative, and a flyer can be balanced while statically stable if the zero-lift pitching moment is positive. To quantify the pitch-stability derivative, we fit a linear model (Eqn. 2.1) to the outputs of each wing-body

configuration if it had converged for a minimum of four angles of attack. We verified that the data fit was linear ($R^2 > 0.99$). We then extracted the slope ($\frac{dC_{m_{morph}}}{dC_{L_{morph}}}$) and the y-intercept ($C_{m_{morph,L=0}}$) for each configuration.

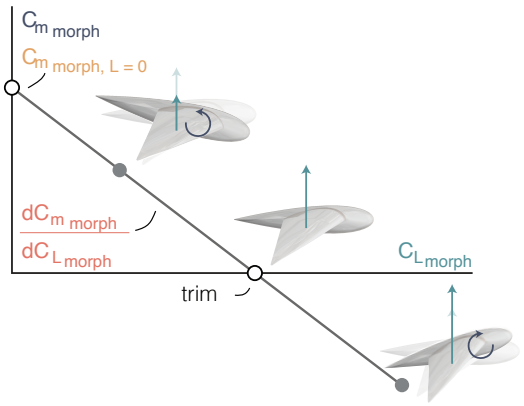

Figure 2.6: **Representative example of the relationship between lift and pitching moment for a statically stable wing.** Longitudinal static stability can be quantified with the zero-lift pitching moment and pitch-stability derivative.

2.4.3 Longitudinal static stability

First, we evaluated the static stability, which requires that a stable glider perturbed from its equilibrium by an external disturbance (Fig. 2.6) will develop a change in pitching moment with an opposite sign to the change in the lift force. This returns the glider towards its equilibrium. We found that all the investigated wing-body configurations had entirely negative pitch-stability derivatives and thus were statically stable (Fig. 2.7a). The magnitude of the static stability was higher for more folded wing configurations. Next, we evaluated the traditional aircraft static margin metric which is equal and opposite to the pitch-stability derivative:

$$static\ margin = -\frac{dC_{m_{morph}}}{dC_{L_{morph}}} = \frac{x_{CG} - x_{NP}}{c_{max}} \tag{2.2}$$

Where x_{CG} is the location of the center of gravity and x_{NP} is the neutral point of the wing-body configuration. The neutral point is the location where the pitching moment is independent of the angle of attack. The negative pitch-stability derivatives (positive static margins) for all our tested configurations indicated that x_{NP} is substantially aft of the body quarter-chord.

When we considered the magnitude of the change, our results revealed that joint-driven wing morphing permits a maximum static margin shift of 24% of c_{max}, or approximately 5.1 cm. Moreover, if the gull-inspired wing-body x_{CG} was relocated between 4.1 to 9.2 cm behind the shoulder joint, this sizable static margin shift would allow the glider to shift between stable and unstable configurations. This large static margin shift would result in significantly different handling qualities between configurations, which is usually an undesirable condition for human pilots [138].

In addition, we found that joint-driven wing morphing provides an effective method to control the static margin as the elbow and wrist angles were good predictors of the pitch-stability derivative. We fit a mixed effect model to all of our wing-body configurations following a similar procedure as used for the lift and pitching moment models with the elbow and wrist angle as fixed explanatory variables. We found that this model provided a good fit for the pitch-stability derivative with a marginal R^2 of 0.69 and a conditional R^2 of 0.83.

This analysis assumes a fixed x_{CG}, but in actuality morphing a wing can cause the center of gravity to shift. To estimate an approximate x_{CG} shift associated with joint-driven wing morphing, we investigated the solid 3D printed wings and found a maximum backwards shift of 1.3 cm. Note that this will not necessarily be comparable to an engineered morphing wing because the weight distribution will depend on the manufactured design. However, the x_{CG} shift for a real bird wing-body is likely smaller than the 3D printed wings due to the lightweight nature of feathers compared to the musculoskeletal system and body. To obtain an approximate estimate of the static margin shift, we assumed that the x_{CG} moves opposite to the x_{NP}. This situation would reduce the maximum static margin shift to 3.8 cm (18%). Note that we non-dimensionalized the static margin using c_{max}, but traditional static margin analyses use the mean aerodynamic chord which will be smaller than c_{max}. In all, we expect that our calculated static margin shift of 18% represents a conservative estimate.

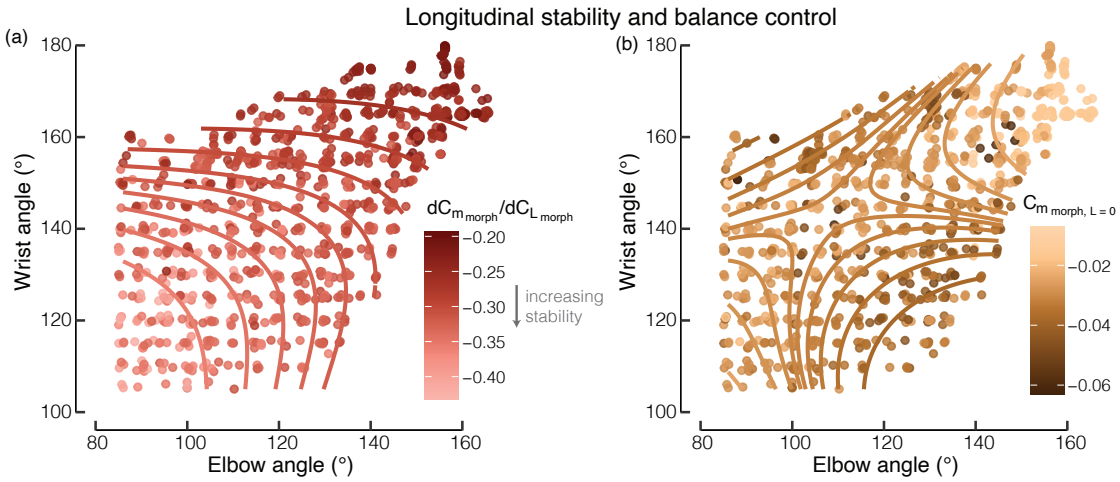

Figure 2.7: **Joint-driven wing morphing provides a reliable method to control static stability characteristics, but not the trim state.** (a) constant zero-lift pitching moment and (b) constant pitch-stability derivative contour lines overlaid on the results obtained from all wings that converged at more than four independent angles of attack (n = 1012).

2.4.4 Longitudinal balance

Next, we investigated the longitudinal balance condition which ensures that while in trimmed flight a glider can create sufficient lift to support its weight when there is no net moment (mathematically represented by a positive x-intercept of Eqn. 2.2, Fig. 2.6). Because we require a negative slope for static stability, this in turn requires the y-intercept or zero-lift pitching moment to be positive. We found that none of our wing-body configurations had a positive zero-lift pitching moment (Fig. 2.7b). As a result, a gull-inspired wing-body with the wings aligned following our convention could not be balanced at 0° while flying in a stable condition. This result is identical to a positively cambered aircraft wing which has a negative zero-lift pitching moment [140]. Furthermore, our results showed that the elbow and wrist would not provide a reliable method to control the trim position because they were poor predictors of the zero-lift pitching moment (marginal R^2 of 0.39 and a conditional R^2 of 0.42).

However, like fixed-wing aircraft a horizontal tail with control surfaces could be added to gain control. Interestingly, unlike fixed wing aircraft, birds not only have a controllable horizontal tail, but they also can rotate their wing about their shoulder joint. This is especially relevant because birds are capable of sustained flight without their tails, possibly suggesting

an alternative method can be used to maintain trimmed flight [137]. It follows that to have controllable, balanced flight for the wing-body configurations investigated, it will be necessary to investigate the possible roles of both a controllable horizontal tail and a controllable shoulder angle.

2.5 Discussion

Joint-driven wing morphing creates a two-dimensional morphing space (Fig. 2.8a, shaded region) that encompasses a wide variety of aerodynamic properties available to a single wing. In flight, a joint-driven morphing wing can follow any continuous joint trajectory through this space. We defined a joint trajectory as a specific set of elbow and wrist angles obtained by following any continuous line within the shaded region of Fig. 2.8a, and a joint extension trajectory as a specific subset of joint trajectories that progress from left to right on Fig. 2.8a. Note that it is also possible to implement these trajectories in reverse (flexion), however in this work we focus on the effects of extension alone. Each specific joint extension trajectory will be associated with differing gradients in aerodynamic properties where gradients can be visualized by considering the contour lines in Fig. 2.5a, b, and 2.7. Contour lines were extracted from the lift, pitching moment and pitch stability derivative models using the R package ContoureR [172].

2.5.1 The role of joint extension trajectories

To identify joint extension trajectories that could be useful for a gull-inspired morphing UAV, we examined four unique trajectories at a fixed 0° angle of attack while assuming a quasi-steady extension that neglects any unsteady aerodynamic effects (Fig. 2.8a). The first three trajectories were selected by individually extracting constant contour lines from the lift (number 1), pitching moment (number 2) and pitch-stability derivative models (number 3) (Fig. 2.8a). The final trajectory considered is the linkage trajectory (number 4) which is the set of coupled elbow and wrist angles that are provided by the mechanical advantage of the gull wing's six-bar linkage system (Fig. 2.8a) [126, 133]. These angles were determined in a previous study by fixing the humeral head of a specimen's wing and manually applying a point

force within an approximate *x*-*y* plane (Fig. 2.1) to a point on the wrist; this causes both the elbow and wrist joints to extend due to the linkage coupling [126]. This approach allows us to extract the kinematics of the coupled linkage system that is caused by the displacement of a single point, the point on the wrist in this case. Finally, we visualized the wing shape at the start and end of each trajectory from the ventral view (Fig. 2.8c) and head-on view (Fig. 2.8d).

We found that both the constant lift and constant pitch-stability derivative trajectories decoupled stability characteristics from load production. First, the constant lift trajectory (Fig. 2.8a, number 1) created the highest absolute change in the pitch-stability derivative, exhibiting a linear response ($R^2 > 0.99$) throughout the extension (Fig. 2.8b and e). This linear trend indicates that the control effectiveness remains constant, removing the need for a controller to know the exact position of the wing. In addition, this trajectory had a minimal effect on the pitching moment, where the instantaneous control effectiveness (instantaneous slope from Fig. 2.8e) of the pitching moment was below $5 \times 10^{-4}/^{\circ}$ until over halfway extended but increased as the wing neared maximum extension. In all, extension along the first half of the constant lift trajectory would allow a simple trajectory for a morphing UAV to adjust its static margin without affecting the lift or pitching moment. This extension trajectory could allow a gull-inspired morphing UAV to shift from a stable to an unstable configuration without affecting its longitudinal position or orientation. Decreasing static stability may be useful when a flight environment becomes gustier because lower static stability reduces the strength of the inherently developed pitching moment and may reduce path oscillations [128]. As a result, this morphing trajectory may allow an active form of gust rejection.

The second trajectory that decouples stability from load production is the constant pitch-stability derivative trajectory (Fig. 2.8a, number 3). This extension trajectory created a large magnitude increase in lift and decrease in pitching moment both with linear responses ($R^2 > 0.99$) throughout extension (Fig. 2.8b and e). This trajectory acts similar to a traditional symmetric flap deflection because a downward flap deflection increases lift and creates a nose-down pitching moment, which can be counteracted with a controllable horizontal tail. Thus, as with flaps this extension trajectory could be used to steepen the approach angle during landing. Also similar to flaps that do not change the overall wing area, this trajectory avoids the undesirable change to an aircraft's handling qualities that is caused by a static margin shift [138]. However,

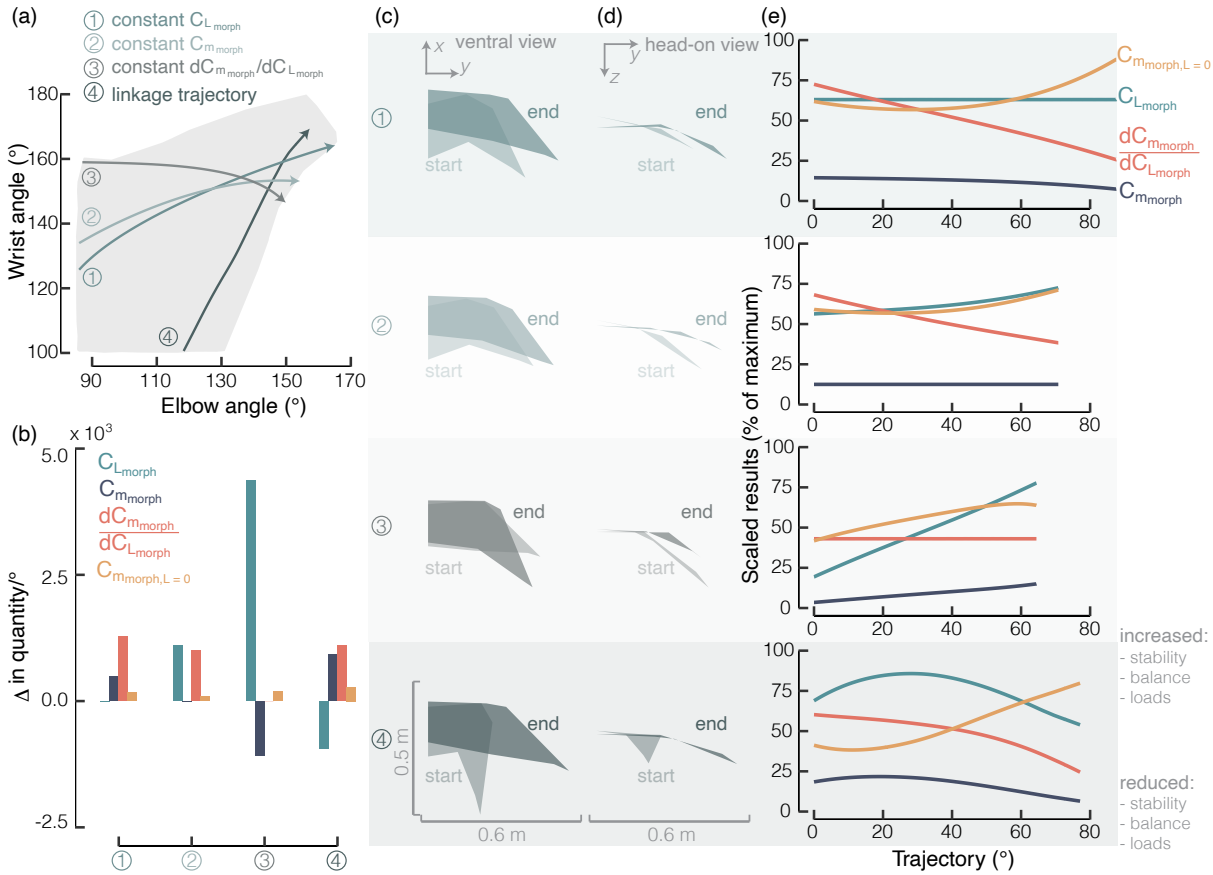

Figure 2.8: **Constant joint extension trajectories allow variable longitudinal control strategies.** (a) The entire range of motion investigated (shaded region) overlaid with the four investigated trajectories: 1) constant lift force, 2) constant pitching moment, 3) constant pitch-stability derivative, and 4) linkage trajectory. (b) The total control effectiveness of the trajectory (y-axis) is defined as the change in a parameter between the start and end per degree of extension along the entire trajectory arc length. Planform view (c) and head-on view (d) of the wing shapes at the start of each trajectory overlaid with the shapes at the end. (e) The instantaneous control effectiveness of each longitudinal quantity, represented by the instantaneous slope at each point, is highly variable. Each quantity is scaled between its absolute minimum and maximum based on the results at 0° angle of attack. 0% represents the lowest loads, least stable and least balanced configuration.

because the relationship between lift and pitching moment is directly affected by the location of x_{CG}, a successful implementation of this morphing trajectory in a gull-inspired morphing UAV will need to include a detailed trade-off study investigating the most beneficial placement of x_{CG}.

Our results showed that minor variations off the identified trajectories recouples the stability and loading characteristics. Consider the constant pitching moment trajectory (Fig. 2.8a,

number 2) which appears to be slightly askew from the constant lift trajectory (Fig. 2.8a, number 1). Yet, the constant pitching moment trajectory has a strong non-linear coupling between the developed lift and static stability (Fig. 2.8b and e). Thus, precise joint angle control will be needed for a UAV to gain the discussed benefits from the two decoupled trajectories. This required precision increases the challenge of manufacturing an effective joint-driven morphing wing.

Finally, we investigated extension along the linkage trajectory (Fig. 2.8a, number 4) and found that this extension does not cause the largest change to any individual parameter but does cause the largest magnitude change across all parameters compared to the other investigated trajectories. Interestingly, there was a non-linear response, such that the instantaneous control effectiveness differs substantially from the total control effectiveness (Fig. 2.8e and b). Specifically, at the start of the extension trajectory $C_{L_{morph}}$ increases by $6.3\times10^{-3}/°$ and $C_{m_{morph}}$ decreases by $2.2\times10^{-3}/°$, increasing the absolute load on the wing. Near the end of the extension trajectory $C_{L_{morph}}$ decreases by $4.7\times10^{-3}/°$ and $C_{m_{morph}}$ increases by $2.2\times10^{-3}/°$, decreasing the absolute load on the wing. Thus, extension alone allows a method to both increase and decrease aerodynamic loads, solely dependent on the wing's position along the extension. Note that these instantaneous control effectiveness values are a larger magnitude compared to those obtained by all other investigated trajectories (Fig. 2.8b and e). The strong variability in the response possibly allows the linkage trajectory to serve many different functions in flight such as initiating and maintaining complex manoeuvres. Moreover, due to the mechanical advantage of the linkage system, following this trajectory requires input from only a single actuator which would simplify the manufacturing process of such a wing. However, the lift and pitching moment are strongly coupled to the balance and stability characteristics for the linkage trajectory. As such, flight control using joint-driven wing morphing along the linkage trajectory would be undesirable for human pilots without an additional controller to account for the shifting static margin.

2.5.2 Comparison to existing UAV

There are few comparably-sized engineered morphing wing aircraft with published longitudinal characteristics. One great example is a goshawk-inspired drone with a maximum wing

span (1.05m) that is 87% of the scale of our largest wing (1.21m) [29]. This aircraft saw a minimal change in the lift and pitching moment produced between a swept and extended position (with a furled tail) around 0° but, at higher angles of attack the extended wing had substantially higher loads with an absolute variation up to roughly 0.5 in C_L and 0.4 in C_m. Note that C_m was non-dimensionalized by the mean aerodynamic chord which is smaller than c_{max} and thus our range of pitching moment cannot be compared directly. Our morphing wing-body numerical results showed an absolute variation of 0.48 in $C_{L_{morph}}$ and 0.18 in $C_{m_{morph}}$ at 0°. Further investigation of our experimental results indicated that the absolute variation remains relatively constant across the investigated angles of attack with the range only beginning to reduce below -5°. This suggests that a joint-driven morphing wing UAV may effectively provide lift and pitching moment control across a broader range of angles of attack when compared with planar sweep-only morphing.

2.5.3 Open loop vs. closed loop

The preceding discussions of longitudinal stability and balance have assumed that the gull-inspired morphing UAV would be controlled with open-loop stability (as is done when a glider is statically stable). Instead, it is possible to use closed-loop stability to successfully fly while in an unstable configuration [138]. For the gull-inspired morphing UAV, the x_{CG} would have to be shifted backwards by over 9.2 cm from the body quarter-chord to render the entire range of motion unstable. In this configuration, the pitch-stability derivative will be positive and thus, a negative zero-lift pitching moment would permit a trimmed position. In traditional aircraft design this is called relaxed static stability. Such an aircraft benefits from improved drag performance and maneuverability characteristics but requires a high degree of control to avoid the potentially serious consequences of an unstable response to external inputs such as gusts [138]. Our current results cannot comment on whether live birds utilize open-loop or closed-loop control, but for a gull-inspired morphing UAV, closed-loop control offers an alternative to installing a horizontal tail. In this case, the trim position would still need an effective control method. This control could possibly be provided by the shoulder angle similar to hang gliders [137, 140].

2.6 Limitations

It is important to note that our previous study of real prepared gull wings found the opposite relationship between elbow angle and the pitch-stability derivative compared to the current rigid wing results [128]. We expect that differences between the two studies may be caused by feather flexibility, feather porosity, different wing alignments, and/or the inclusion of wing-body interaction effects within the current study. Further investigation to understand the differences between a rigid 3D printed wing shape and a real gull wing will be necessary.

To this end, many assumptions were required to allow a targeted analysis of the effects of elbow and wrist morphing and will require investigation in future studies to approach a general understanding of how birds fly. For example, in this study we did not include variations in velocity or Reynolds number. Birds use an intermediate Reynolds number and it is therefore possible that shifting into a lower or higher regime could have a measurable effect on the longitudinal characteristics of an avian-inspired wing [122]. Additionally, it will be necessary to evaluate the coupled role of shoulder joint control with elbow and wrist morphing to develop a holistic understanding of flight control due to avian wing morphing. Further, our work assumed quasi-steady extension, however in reality, birds can manipulate their joints very quickly. This quick motion could result in induced flow along all major directions. A detailed mechanistic study is warranted in the future to determine the presence and the role of specific unsteady aerodynamic effects. Finally, we only investigated a single species, but birds have a broad range of species diversity, each of which may offer unique insights on how to efficiently design UAVs. In particular, we expect different control effectiveness values between different bird species due to variable wing range of motion, linkage structures and overall geometry [122, 126, 148].

2.7 Conclusion

We investigated the potential benefits of gull-inspired joint-driven wing morphing for future UAV applications. First, we determined a set of simplified wing shapes across the range of motion of the elbow and wrist used by gliding gulls. Next, we used a numerical general lifting-line model (MachUpX) validated with wind tunnel experiments to determine the longitudinal

characteristics of the wing-body configurations. Our results showed that wings with the highest load production had low wrist and high elbow angles and were associated with wing tip wash-in. Additionally, although the inherent response to an external disturbance for all wing-body configurations was stable, we found that a controllable horizontal tail or shoulder angle would be necessary to successfully provide open-loop control. Importantly, we found that the elbow and wrist angle could provide a reliable method to control the lift, pitching moment, and overall static margin but would not be sufficient to control the zero-lift pitching moment alone.

Our study revealed that the two-dimensional morphing space allowed by the elbow and wrist joints permits a wide variety of flight control strategies. In particular, we identified two trajectories that decoupled longitudinal static stability and longitudinal load production. One trajectory (Fig. 2.8a, number 1) linearly adjusts static stability without affecting the load production and the other (Fig. 2.8a, number 3) linearly adjusts the lift and pitching moment without affecting stability, in a manner similar to an aircraft flap that does not change the wing area. Moreover, the identified linear response is highly advantageous for a simplified controller design. However, we found that a unique but similar trajectory (Fig. 2.8a, number 2) recouples the loads and stability, suggesting that precise control of the elbow and wrist would be necessary to realize these aerodynamic benefits in a UAV. Finally, the linkage trajectory (Fig. 2.8a, number 4) afforded by the gull's musculoskeletal linkage system yielded the highest instantaneous control effectiveness of all our investigated trajectories and represents a simple actuation trajectory that can quickly adjust the longitudinal characteristics. However, the load production and stability are highly coupled for this trajectory and other control mechanisms would be required to negate this effect. In all, investigation of these unique trajectories highlights the multifunctional capabilities of gull-inspired joint-driven wing morphing.

Despite the identified aerodynamic benefits of a joint-driven morphing wing, a major challenge for any bio-inspired UAV is to design an efficient actuation mechanism that can realize the proposed benefits in practice. In the past, a non-planar wing design that was indirectly inspired by gulls, the HECS wing (discussed in the Section 2.2) was shown to yield minimal aerodynamic benefits when it was actively morphed into its furled configuration [173] despite promising rigid model results [149]. This emphasizes the multidisciplinary challenges associated with effective morphing wing design. Successful implementation of gull-inspired

joint-driven morphing wings will require detailed structural analyses, flight tests, and multidisciplinary investigations to determine if the benefits identified within this study could effectively and efficiently be realized in a morphing wing UAV.

Do the benefits provided by joint-driven wing morphing outweigh engineered morphing wing designs? Our results show that gull-inspired joint-driven wing morphing creates a similar magnitude of control effectiveness as an equivalent aircraft with a sweeping mechanism, but with the added multifunctional capabilities permitted by the variable joint extension trajectories. This is especially promising because we found that a joint-driven morphing wing can produce a similar aerodynamic response to traditional flaps but would not be limited to this singular functionality. Combined with future multidisciplinary investigations, we expect that gull-inspired joint-driven wing morphing could provide a future generation of UAVs the unique ability to adapt on the fly by morphing along the specific joint trajectory that realizes the desired aerodynamic characteristics.

Chapter 3

The Evolution of Avian Pitch Stability

I am among those who think that science has great beauty. A scientist in [their] laboratory is not only a technician, [they are] also a child placed before natural phenomenon, which impress [them] like a fairy tale.

– Marie Curie

3.1 Summary

Birds morph their wing shape to accomplish extraordinary maneuvers [174–177], which are governed by avian-specific equations of motion. Solving these equations requires information about a bird's aerodynamic and inertial characteristics [138]. Avian flight research to date has focused on resolving aerodynamic features, whereas inertial properties including center of gravity and moment of inertia are seldom addressed. Here, we used an analytical method to determine the inertial characteristics of 22 species across the full range of elbow and wrist flexion and extension. We find that wing morphing allows birds to substantially change their roll and yaw inertia but has a minimal impact on the center of gravity position. With the addition of inertial characteristics, we derived a novel metric of pitch agility and estimated the static pitch stability, which revealed that the agility and static margin ranges are reduced as body mass increases. Surprisingly, our results provide quantitative evidence that evolution selects for both stable and unstable flight, a result that contrasts with the prevailing narrative that birds are evolving away from stability [178]. This comprehensive analysis of avian inertial characteristics provides the key features required to establish a theoretical model of avian maneuverability.

3.2 Background

There is currently no theory that provides hypotheses to guide studies of avian maneuverability. This is not due to a lack of physical understanding; maneuverability can be broadly defined as a bird's ability to change the magnitude and/or direction of its velocity vector [19, 20]. Like comparable UAVs, a bird's flight dynamics, and thus maneuverability, are dictated by its governing equations of motion. For example, aircraft dynamics depend on a minimum of six equations; three translational and three rotational that can be derived from Newton's second law and it's rotational counterpart [138, 179]:

$$\mathbf{F} = \frac{\mathrm{d}(m\mathbf{v})}{\mathrm{d}t} \tag{3.1}$$

$$\mathbf{M} = \frac{\mathrm{d}(\mathbf{I}\boldsymbol{\omega})}{\mathrm{d}t} \tag{3.2}$$

Where $\mathbf{v}$ is the velocity vector and $\boldsymbol{\omega}$ is the angular velocity vector. These equations can be combined to solve for a flyer's acceleration (translationally: $\frac{\mathrm{d}\mathbf{v}}{\mathrm{d}t}$ and rotationally: $\frac{\mathrm{d}\boldsymbol{\omega}}{\mathrm{d}t}$), but this requires knowledge of both the aerodynamically informed external forces ($\mathbf{F}$) and moments ($\mathbf{M}$) as well as the inertial characteristics including the mass (m) and moment of inertia tensor ($\mathbf{I}$). However, avian inertial characteristics are not currently available with sufficient breadth or resolution.

Therefore, avian flight maneuverability is often evaluated experimentally by tracking individuals to measure accelerations during observed maneuvers [176, 177]. However, tracking data do not provide a bird's maximal maneuvering capabilities or allow extrapolation to unobserved behaviors. Determining these attributes requires a robust and general framework for maneuverability, equivalent to the maneuverability equations for aircraft [19, 180]. Obtaining generalizable data is further complicated because aerodynamic and inertial characteristics vary substantially within and among species, and even dynamically for an individual bird [126, 174]. For example, birds can initiate maneuvers by changing the orientation and shape of their wings, body and tail, known as morphing [20, 137, 181]. To progress towards a theoretical formulation of avian maneuverability, there has been a marked and justifiable focus on resolving the aerodynamic characteristics of a bird in flight [127, 128, 141]. However, studies often overlook

the equally essential inertial properties (Fig. 3.1a) or use static morphology approximations for individual species [51, 137, 182–184]. Here, we fill this gap by investigating the variable inertial characteristics of flying birds to provide the necessary next step towards establishing a general framework of avian maneuverability.

Another challenge to solving a flying bird's equations of motion is how to properly formulate the equations. For example, the equations can be simplified by defining the origin at the center of gravity (Fig. 3.1a), which is equivalent to the center of mass within a constant gravitational field [179]. If the center of gravity moves substantially relative to the body, additional terms in the equations are required to properly capture flight dynamics [180]. Physically shifting a bird's morphology will shift the center of gravity but, it is not currently known how much the center of gravity moves as a bird morphs. In addition, the rotational inertia, quantified by the mass moment of inertia tensor (**I**) about the origin will also be affected by morphing (Fig. 3.1a and b). This symmetric matrix describes the body mass distribution where diagonal elements quantify the distribution relative to the major axes (I_{xx}: roll, I_{yy}: pitch, I_{zz}: yaw) and off-diagonal elements quantify distribution within the three major geometric planes (only I_{xz} is non-zero for symmetric configurations, Fig. 3.1a) [179].

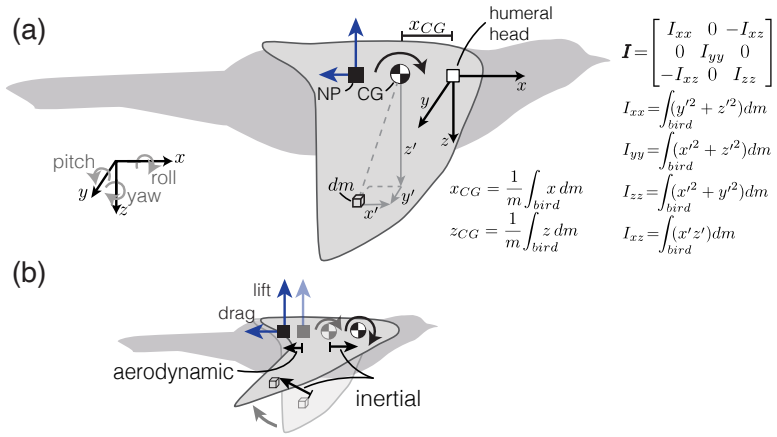

Figure 3.1: **Inertial properties must be determined to quantify avian maneuverability.** (a) A bird's center of gravity (CG) is the position about which weight is equally distributed, and the neutral point (NP) is where aerodynamics forces can be modeled as point forces and the pitching moment is independent of angle of attack. The moment of inertia components (**I**) are obtained by integrating differential mass elements (*dm*) over the entire bird. (b) Flight dynamics are affected by adjusting either inertial or aerodynamic characteristics. (c) We modeled birds as a composite of simple geometric components.

We calculated a bird's center of gravity and **I** to evaluate avian maneuverability through the lens of agility and static stability. Agility encompasses a bird's ability to perform linear accelerations (axial agility) and angular accelerations (torsional agility) [20], and depends on both the center of gravity and **I** [138]. In contrast, static stability refers to the initial tendency to return towards an equilibrium after a disturbance [128]. We quantified static pitch stability with the static margin, which is the distance between the center of gravity and neutral point (NP, Fig. 3.1a) [138, 141]. If the neutral point is aft of the center of gravity, the static margin will be positive and thus stable. Often, stability is inversely related to agility because larger maneuvering forces and moments are sometimes necessary to overcome stabilizing forces and moments [128].

3.3 Methodology - Inertial characteristics

To determine how inertial characteristics vary during wing morphing, we developed a general analytical method to quantify any flying bird's center of gravity and **I**, and used a comparative analysis to investigate 22 species spanning the phylogeny defined by Prum et al. [116] except for Palaeognathae as this clade contains largely flightless birds. First, we measured geometric and mass properties of cadavers (Section 3.3.1) and used motion tracking on cadaveric wings to extract the range of extension and flexion for the elbow and wrist (Fig. 3.2e, Section 3.3.2). We limited our study to solely investigate the role of wing morphing due to elbow and wrist flexion and extension because previous studies have shown that this range of motion (ROM) allows a substantial shift in the neutral point [128, 141]. The investigated ROM defines a bird's physical capability to adjust its inertial characteristics and includes wing configurations outside of those likely used in flight. In addition, we assumed that the shoulder was set to allow a comparable wing orientation (see Section 3.3.3) and that the tail is furled, but these degrees of freedom play an important role in avian flight control [185] and warrant future morphing studies. Finally, we developed an open-source R package (AvInertia) that models birds as a composite structure of simple geometric objects and uses morphological data to calculate the center of gravity and **I** for any bird using any wing configuration (Fig. 3.2a, b, c, d, Appendix A, Section 3.3.3). We validated this methodology with previous static wing measurements

(Fig. 3.3, Section 3.3.4).

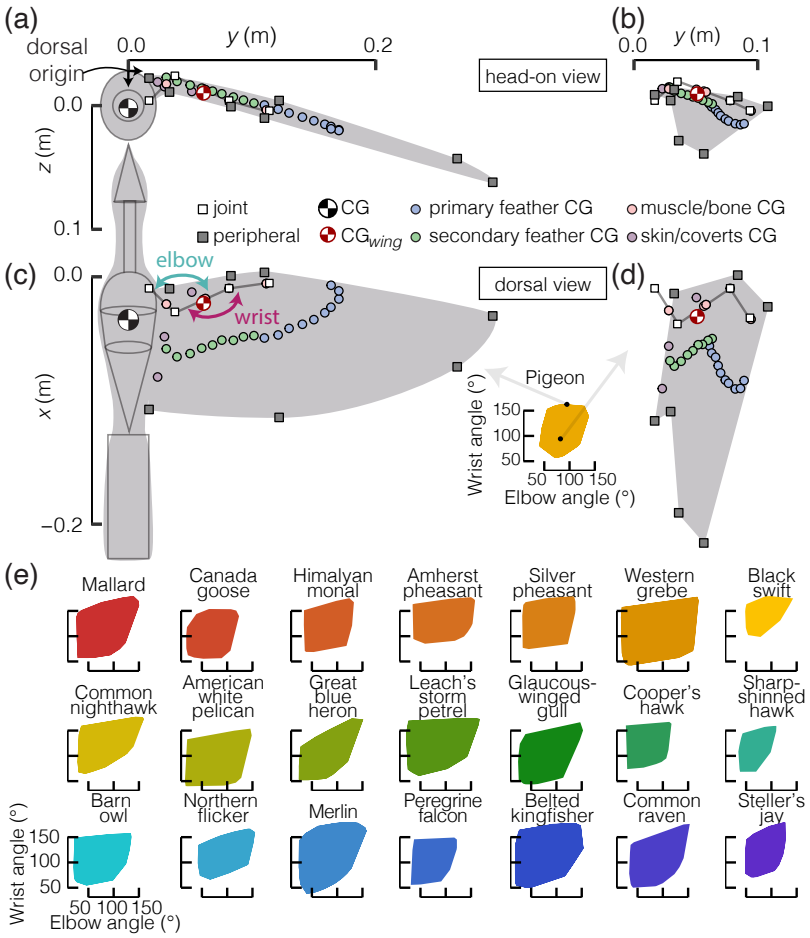

Figure 3.2: **Elbow and wrist joint range of motion informed our analysis.** (a) We modeled birds as a composite of simple geometric components. Each component's center of gravity varies as a wing morphs from an extended (a and c) to a folded (b and d) configuration. (e) Convex hulls showcase the range of motion (ROM) of the elbow and wrist for 22 species.

3.3.1 Collecting morphological data

We obtained morphological data for 36 adult specimens representing 22 species (Fig. 3.4a) from frozen cadavers acquired from the Cowan Tetrapod Collection at the Beaty Biodiversity Museum (University of British Columbia, Vancouver, Canada). Sample size was a function of the availability and quality of specimens from the museum as we could only rely on fully-intact, well-preserved specimens. The cadavers were inspected to ensure adequate condition and completeness, after which we measured the full body mass, wingspan, and body length.

Next, we disarticulated the wing at the shoulder joint, taking care to ensure that each wing's skin, propatagial elements, and feathers remained intact. One wing from each cadaver was used to determine wing ROM and corresponding wing shape change (see following section). The cadaver was further dissected to obtain length and mass measurements for the head, neck, torso, wing components, legs, and tail. We obtained the center of gravity coordinates for the torso (body without head, neck, tail, wings) by manually balancing the torso and measuring the distance from the clavicle reference point to the balanced position. Note that because of the preservation of the storm petrel specimens, we estimated the mass based on humerus bone length and the torso center of gravity as being proportional to that of the gull. Finally, we individually weighed and photographed each flight feather allowing geometric parameters to be extracted using ImageJ software [186]. Refer to the publicly available data repository for details on all assumptions used for extracting the morphological measurements. This study consisted of a single experimental group and thus randomization and blinding was not necessary.

3.3.2 Determining the elbow and wrist range of motion

To determine the wing ROM and corresponding shape change, we actuated the cadaver wings throughout the full range of extension and flexion of the elbow and wrist joints by hand (following methods established by Baliga et. al [126], Fig. 3.2e). We tracked the location of ten 4-mm diameter, reflective markers (gray and white points in Fig. 3.2a-d) with automated 3D data capture at 30 frames per second via a four- or five-camera tracking system (OptiTrack: NaturalPoint, Inc.). Using NaturalPoint, Inc. tools, each recording was calibrated to have less than 0.5 mm overall mean reprojection error. Joint angles were calculated as the interior angle defined by three key points: points 1, 2 (vertex), and 3 for the elbow, and points 2, 3 (vertex), and 4 for the wrist (Appendix A).

3.3.3 Developing AvInertia

We developed an open-source R package (AvInertia) to calculate the center of gravity and moment of inertia tensor ($\mathbf{I}$) for any flying bird (Fig. 3.1a) in RStudio (version 1.3.1093)[187]

running R (version 4.0.3) [188]. A high-level overview of the code methodology follows in this section. Further details are provided in Appendix A, as each individual component of the avian models required specific procedures and approximations.

To allow a generalized approach, we used a common methodology from mechanics to estimate the center of gravity and inertia components using simple geometric shapes [179]. We elected to use as many elements as possible to allow the best resolution. For each species, we first modeled the bird's body without the wings as a composite of five components: head, neck, torso, legs, and tail. To determine the inertial properties of the wings, we aligned each wing configuration extracted from the ROM measurements so that the wrist joint was in line with the shoulder joint along the y- and z-axes and so that the wrist joint was aligned with the first secondary feather (S1) along the x-axis (extended wing: Fig. 3.2a and c; folded wing: Fig. 3.2b and d). Note that this positioning results in a different shoulder angle between each wing configuration and wings with extremely low elbow angles and high wrist angles may be at substantially different incidence angles than the body. Each wing was then modeled as a composite of twelve components: bones (humerus, radius, ulna, carpometacarpus/digit, radiale and ulnare), muscles (brachial, antebrachial and manus groups), skin, coverts, and tertiary feathers. In addition, each primary and secondary feather was modeled and positioned individually as a composite structure of five components: calamus, rachis (cortex exterior and medullar interior), and distal and proximal vanes. AvInertia permits a variable number of flight feathers. With our methodology, a bird with 10 primaries and 10 secondaries that flies with an extended neck will be represented by a composite model with 232 individual simple geometric shapes. In our study, we investigated only symmetric wing configurations for a full bird and considered the effects of a single wing independently. We assumed that anisotropic effects such as the air space within the body would have a minimal impact on the overall center of gravity [189].

To calculate the final inertial characteristics of this composite bird, each component's shape, mass, and positioning was informed by its corresponding morphological measurements. We began by determining the center of gravity and $\mathbf{I}$ for one of the basic geometric shapes with respect to an origin and frame of reference that simplified the formulation of the center of gravity and $\mathbf{I}$ for that shape. Next, AvInertia computed the mass-weighted summation of the center of gravity of each object and shifted the origin to the bird reference point, located at the

center of the spinal cord when cut at the clavicle. The center of gravity was then transformed into the full bird frame of reference, which is defined by Fig. 3.2a-d. We used the parallel axis theorem and the appropriate transformation matrices to transform **I** to be defined about the final center of gravity within the full bird frame of reference.

3.3.4 Validating AvInertia

We validated our methodology by comparing the maximum rotational inertia about the roll axis for a single wing (I_{xxwing}, origin at the humeral head) to data from previous experimental studies that measured I_{xxwing} by cutting an extended wing into strips (Fig. 3.3) [190, 191]. Our 95% confidence intervals on the exponent of body mass marginally overlapped with Berg and Rayner's predictions [190] but were significantly lower than Kirkpatrick's predictions [191]. However, Kirkpatrick used 10 wing strips while Berg and Rayner later found that at least 15 strips were necessary to minimize systematic error [190, 191]. Next, we directly compared results for the pigeon (*Columba livia*), the only species in common between the studies, and found $I_{xxwing}(\times 10^4)$ was between 1.42 to 1.92 kg-m^2, which encompasses results from previous studies (1.72 and 1.83 kg-m^2) [190–192]. The pigeon wing's maximum center of gravity position along the *y*-axis ($\overline{y_{CG}}_{wing}$) was only 3% of the half span more proximal than Berg and Rayner's measurement [190]. We expect minor differences because strip methods enforce that all wing mass is contained within the *x*-*y* plane while AvInertia accounts for out-of-plane

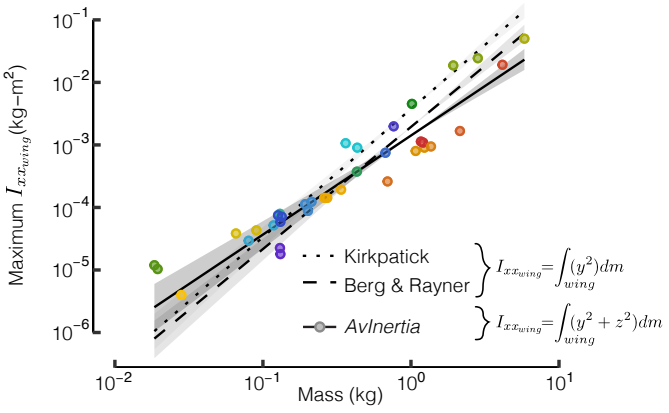

Figure 3.3: **Our results agreed with previous estimates of the wing's moment of inertia.** The computed maximum $I_{xx_{wing}}$ was comparable to published estimates. 95% confidence intervals visualized by transparent ribbons (n = 36 individual specimens).

morphology (Fig. 3.3).

3.3.5 Statistical analyses

All phylogenetically informed analyses were carried out using the time-calibrated Maximum Clade Credibility tree from Baliga et al.[126], which was pruned to the 22 focal taxa in this study (Fig. 3.4a). To determine the linear trends with body mass, we fit first-order phylogenetic generalized linear mixed models (PGLMM) to the data using the R package MCMCglmm [193] where the random effects are informed by the phylogeny (Table 3.1). These results will be discussed in further detail in the following sections. All PGLMM models had priors specified with the inverse Wishart scaling parameters V = 1 and $\nu = 0.02$ and used 1.3×10^7 Markov chain Monte Carlo (MCMC) iterations. To determine the significance and effect of the elbow and wrist on the center of gravity and $\mathbf{I}$ components, we independently fit first order interactive models to each specimens' data with a constant scaling on the elbow and wrist angle. We calculated the effect size of the elbow and wrist using the R package effectsize [194] and independently fit first order interactive models to each specimens' data with scaled and mean centered elbow and wrist angles.

3.4 Results - Inertial characteristics

3.4.1 Center of gravity

With our validated results, we first asked: what effect does the elbow and wrist ROM have on a bird's center of gravity when its wings are held symmetrically? Our results revealed that the ROM had a minimal effect on the center of gravity position (Fig. 3.4b, opaque polygons). The maximum shift along the x-axis and z-axis ($\overline{x_{CG}}$ and $\overline{z_{CG}}$, normalized by the full bird's length) was 3% (great blue heron, *Ardea herodias*, 2.0 cm) and 2% (barn owl, *Tyto alba*, 0.7 cm), respectively (Fig. 3.4b). Despite the small magnitude, wrist extension consistently shifted $\overline{x_{CG}}$ forwards (p-values < 0.002) and the wrist angle explained a high amount of variance in the data leading to a high effect size, quantified by partial eta-squared (η^2) [194, 195]. We found partial η^2 was greater than 0.34 for all species (Fig. 3.4e). Similarly, elbow extension

Table 3.1: **MCMCglmm outputs for inertial phylogenetic generalized linear mixed models (PGLMM).**

Dependent variable	Independent variable	Slope 95% credible intervals	*p*-value
$\log(-\overline{x_{CG}})$	log(body mass)	-0.007, 0.174	0.062
$\log(\overline{z_{CG}}*)$	log(body mass)	-0.06, 0.19	0.314
$\Delta\overline{x_{CG}}$	wingspan to length ratio	0.02, 0.09	0.002
$\log(\overline{y_{CG}}_{wing})$	log(body mass)	-0.01, 0.07	0.166
$\Delta\overline{y_{CG}}_{wing}$	arm to hand ratio	0.05, 0.24	0.016
$\Delta\overline{x_{CG}}$	arm to hand ratio	-0.09, 0.09	0.952
$\Delta\overline{z_{CG}}$	arm to hand ratio	-0.08, 0.11	0.954
$\log(I_{xx})$	log(body mass)	1.51, 1.83	< 0.001
$\log(I_{yy})$	log(body mass)	1.46, 1.77	< 0.001
$\log(I_{zz})$	log(body mass)	1.50, 1.76	< 0.001
$\log(I_{xxwing})$	log(body mass)	1.37, 1.81	< 0.001

tended to shift $\overline{x_{CG}}$ forwards, but its effect size varied across species. Both elbow and wrist extension predominately shifted $\overline{z_{CG}}$ dorsally, but the magnitude and effect size varied. We could not differentiate the log-transformed mean $\overline{x_{CG}}$ or $\overline{z_{CG}}$ position from those expected if birds were simply scaled by preserving all length scales, known as isometry (Fig. 3.4f, Table 3.1). As visualized by Fig. 3.4f, we cannot definitively exclude the possibility that the lower 95% confidence interval on $\overline{x_{CG}}$ may be positive, which would indicate that $\overline{x_{CG}}$ scales greater than isometric predictions. However, multiple MCMCglmm runs returned an insignificant result.

The small effect of the elbow and wrist on the center of gravity location led us to question if this would carry over to shoulder joint motion as well. To obtain a conservative estimate, we assumed that wings could rotate about the humeral head by 90° forwards, aft, up, and down (Fig. 3.4b, transparent squares). This revealed that the maximum $\Delta\overline{x_{CG}}$ and $\Delta\overline{z_{CG}}$ shift was 18% (10.9 cm) for the great blue heron, approximately sixfold greater than that achieved with elbow and wrist morphing alone. Such a large center of gravity shift likely could not be neglected when formulating the equations of motion. At the other extreme, the Lady Amherst's pheasant (*Chrysolophus amherstiae*) had a negligible shift of 1% (1.4 cm) with shoulder joint motion. Across the full range of taxa, we found a significant positive relationship between $\Delta\overline{x_{CG}}$ due to shoulder motion and the ratio of maximum wingspan to body length (Fig. 3.4d,

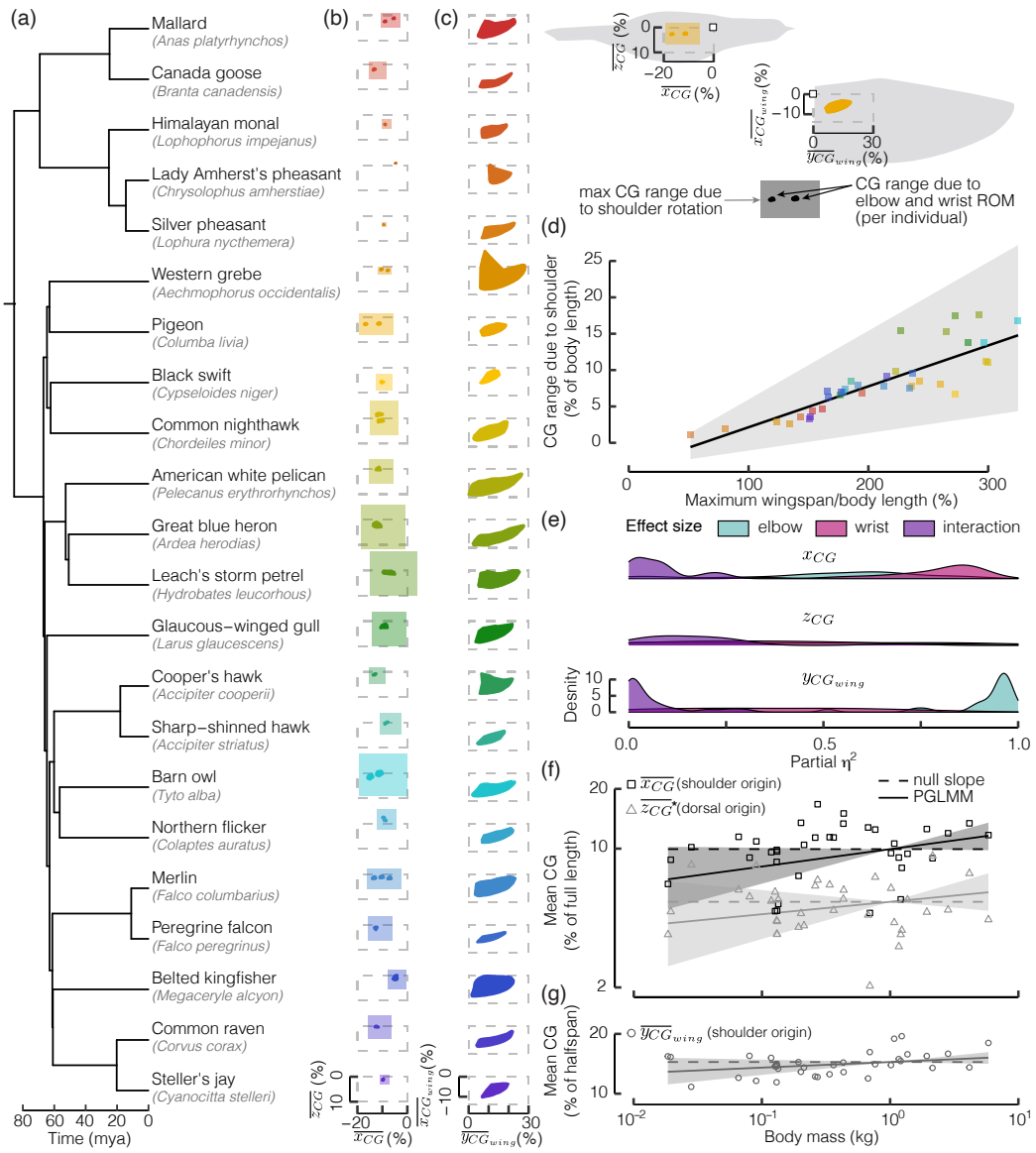

Figure 3.4: **A bird's center of gravity is minimally affected by elbow and wrist flexion and extension.** (a) Time-calibrated phylogeny for 22 species (mya, million years ago). The elbow and wrist ROM (opaque polygons, convex hulls) affect (b) $\overline{x_{CG}}$ and $\overline{z_{CG}}$ (over bar indicates normalization by body length), and (c) $\overline{yCG_{wing}}$(over bar indicates normalization by maximum half span). The center of gravity range is overlaid with the maximum bounds due to 90° shoulder rotation (transparent polygons), which (d) increase with increasing ratio of wingspan to body length. e, Effect size (partial η^2) of elbow, wrist, and interaction on each center of gravity component per specimen. The log-transformed mean values of (f) $\overline{x_{CG}}$, $\overline{z_{CG}}*$ ($*$ denotes the z position relative to the dorsal origin defined by Fig. 3.2a) and (g) $\overline{yCG_{wing}}$ did not scale with body mass as the phylogenetic generalized linear mixed model (PGLMM; solid line) did not differ significantly from the null slope (dashed line). 95% confidence intervals visualized on d, f, and g by transparent ribbons (n = 36 individual specimens).

Table 3.1). This trend suggests that proper modeling of flight dynamics for birds with wings substantially longer than their body length will require an estimation of the expected center of gravity shift to verify if a fixed center of gravity is an appropriate assumption.

Although the full bird's center of gravity defines its symmetric flight dynamics, the wing-only parameters can give insight into asymmetric configurations. We found that the elbow and wrist ROM caused the center of gravity to shift along the *y*-axis ($\overline{y_{CG}}_{wing}$, normalized by the maximum half span) from 10% (black swift, *Cypseloides niger*) to 27% (American white pelican, *Pelecanus erythrorhynchos*) (Fig. 3.4c), where the most distal $\overline{y_{CG}}_{wing}$ was 28% (western grebe, *Aechmophorus occidentalis*). Additionally, $\Delta\overline{y_{CG}}_{wing}$ was positively associated with the arm-to-hand wing ratio (Table 3.1), such that birds with longer hand wings than arm wings (like the swift) would have a reduced capacity to shift the wing's CG. The center of gravity shift was largely driven by elbow extension (p-values < 0.001, partial $\eta^2 > 0.51$, Fig. 3.4e) whereas the effect of the wrist varied across species. These results highlight a well-conserved proximal location of the wing center of gravity across species. Contrary to a previous study [190], we did not find that the log-transformed mean $\overline{y_{CG}}_{wing}$ differed from isometric expectations (Fig. 3.4g, Table 3.1).

3.4.2 Moment of inertia

The center of gravity is crucial to formulating the governing equations, but their solution depends on a bird's rotational inertia. Like the CG, we found that a bird's rotational inertia (log-transformed mean diagonal components of $\mathbf{I}$) scaled isometrically with body mass (Fig. 3.5a, Table 3.1). However, we found that elbow and wrist extension provided over an 11-fold I_{xx} increase (heron) and 3-fold I_{zz} increase (heron and owl, Fig. 3.5c). This capability was largely driven by elbow extension (Fig. 3.5b), which had a significant effect on both I_{xx} (p-values < 0.001, partial $\eta^2 > 0.23$; except Leach's storm petrel, *Hydrobates leucorhous*) and I_{zz} (p-values < 0.009, partial $\eta^2 > 0.45$). The absolute values of I_{yy} and I_{xz} were minimally affected by joint extension and the effect size varied substantially across species (Fig. 3.5b). We next computed the contribution of each major body part to the overall rotational inertia for birds with wings at maximum elbow and wrist extension (Fig. 3.5d, e, and f). Because the wings were extended along the *y*-axis, this captures approximately the lowest wing contribution to I_{yy}

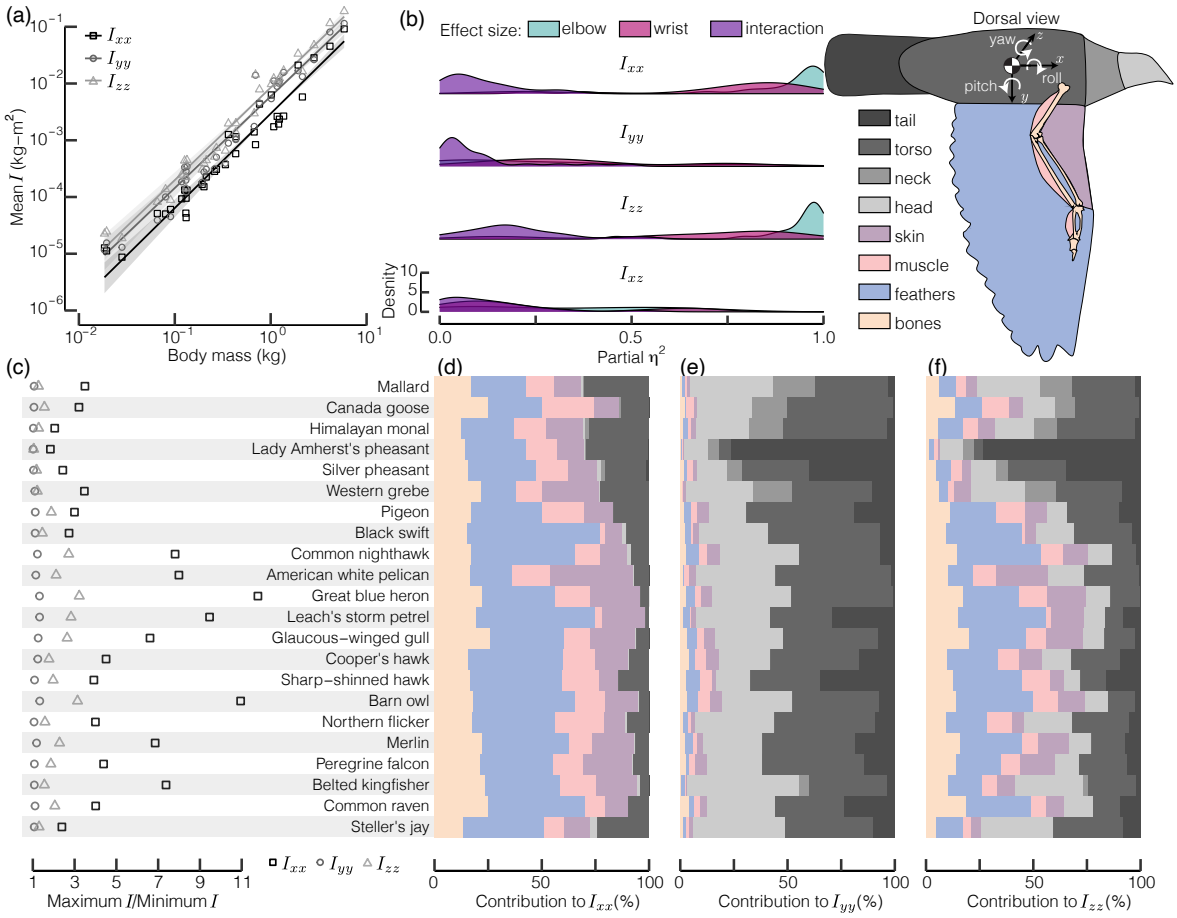

Figure 3.5: **Wing morphing, specifically driven by the elbow, has a strong effect on roll and yaw inertia components.** (a) All log-transformed mean diagonal components scaled isometrically with body mass (PGLMM model for each component; solid line). 95% confidence intervals visualized by transparent ribbons (n = 36 individual specimens). (b) Elbow extension has the largest effect on I_{xx} and I_{zz} but joint angles were not strong predictors of I_{yy} or I_{xz}. (c) The ability to adjust **I** varies substantially across species. At maximum wing extension, the wing components (bones, feathers, muscle, skin) had the largest contribution to (d) I_{xx} while body components (head, neck, torso, tail) played a larger role for (e) I_{yy} and (f) I_{zz}. Components are colored following the bird schematic.

but the highest wing contribution to I_{xx}. The percentage contribution of each body part varied substantially across the species, but as expected the wings were responsible for the majority of I_{xx}. These results indicate that elbow and wrist ROM provides substantial inertial control over the roll and yaw axes (I_{xx}, I_{zz}), but less so for the pitch axis (I_{yy}), although species-specific differences were also apparent in our results. Incorporating the shoulder joint ROM would increase the wing's contribution to inertial pitch control.

3.5 Methodology - Aerodynamic characteristics

Next, to obtain information about the static stability of the birds, we investigated the aerodynamic characteristics associated with wing morphing. To estimate the neutral point of a bird's wing-body configuration, we leveraged our previous study on rigid gull wing-body configurations across the *in vivo* range of motion of elbow and wrist flexion and extension (Chapter 2)[141]. In this previous study, we extracted the neutral point of the wing-body configurations by fitting a linear model to the change of the pitching moment with the lift force [138, 140] and provided the morphological information about the associated wing shapes. We used the same wing orientation as the current chapter. The aerodynamic results were calculated using a numerical lifting line model which was validated with wind tunnel tests on 3D printed wings. As it was not feasible to replicate this analysis for each species in this study, we investigated if there was a metric that could be used to appropriately estimate the neutral point using morphology alone. We assumed that the bird's neutral point could be approximated by the wing-body configuration neutral point. This approximation is appropriate if the wing produces the majority of the lift as is expected with a furled tail [196], but Section 3.7.5 discusses the implications of incorporating the tail.

3.5.1 Estimating the neutral point

Our approach was informed by traditional aerodynamic theory which predicts that the aerodynamic center of a 2D thin airfoil will be at the quarter-chord location [197]. This result can be extended to lifting line theory for steady flight conditions (commonly used in gliding flight) or blade element theory for revolving airfoils (commonly used in flapping flight). However, 2D thin airfoil approximations do not hold for the thick airfoils known to be used on the proximal wing sections of bird wings[158] nor for 3D wing shapes [197]. Although advances in analytical methods have resulted in mathematical relationships that account for constant taper ratios or sweep [198, 199], little information exists for wing shapes as complex as bird wings that have substantial and often nonlinear distributions of geometric twist, taper, sweep, and dihedral. Therefore, we investigated six different chord-based metrics[140, 199, 200] to establish

which would best approximate the neutral point. The origin for all metrics within this study was set at the shoulder joint. This investigation included:

1. **Root chord.** A simplistic approach that estimates the neutral point to be at the quarter chord of the root chord. This approach cannot account for a neutral point shifting forwards of the root leading edge.

2. **Mean chord.** The mean chord (c_m) is first found as [199]:

$$c_m = \frac{S_w}{b}, \tag{3.3}$$

   Where S_w is the total wing area and b is the wingspan. Next, we located the most interior span section that had a chord equal to c_m. At that span section we extracted the leading edge position along the *x*-axis and added it to the quarter chord of c_m while accounting for any wing twist at this span section. This final value was taken as the quarter chord position of the mean chord.

3. **Mean projected chord.** A similar approach as the mean chord but the wing area used is that calculated by projecting the wing periphery onto the *x*-*y* plane.

4. **Mean aerodynamic chord.** A similar approach as the mean chord but the mean aerodynamic chord is calculated as [199]:

$$MAC = \frac{\int_0^{b/2} c(y)^2 dy}{\int_0^{b/2} c(y) dy}, \tag{3.4}$$

   Where $c(y)$ is the chord length along the span as a function of the location on the *y*-axis. The mean aerodynamic chord is calculated numerically by disctretizing each wing along the *y*-axis into 1000 segments. All integral equations that follow used the same discretization.

5. **Centroid area chord.** In this approach we first numerically calculated the position of

the wing's centroid along the *y*-axis as [199]:

$$y_{cen} = \frac{\int_0^{b/2} c(y) y dy}{\int_0^{b/2} c(y) dy} \tag{3.5}$$

Then, at this span location we calculated the chord of the wing. Similar to the approach in the mean chord we next determined the quarter chord and leading edge position.

6. **Standard mean chord.** This method numerically calculates the quarter chord position directly as [199]:

$$\tilde{x}_{c/4} = \frac{\int_0^{b/2} c(y) x_{c/4}(y) dy}{\int_0^{b/2} c(y) dy}, \tag{3.6}$$

Where $x_{c/4}(y)$ is the quarter-chord location as a function of the location on the *y* axis.

For each of the output quarter chord positions from the six different metrics, we normalized by the maximum root chord ($c_{r_{max}}$) of the specimen. This normalization ensures that the result could be scaled for different sized individuals. To assess the fit of each normalized metric to the gull's measured neutral point we fit log-transformed linear models in R:

$$\ln\left(\frac{|x_{NP_{wb}}|}{c_{r_{max}}}\right) \sim \mathbf{A} \ln\left(\frac{|x_?|}{c_{r_{max}}}\right) + \mathbf{B}. \tag{3.7}$$

Note that for all configurations investigated in our previous study, the neutral point had a negative position on the *x*-axis (aft of the shoulder joint), which allowed us to take the absolute value of the data. Surprisingly, the best fit to our data was the standard mean chord (metric 6) as shown by a low model offset (B) and higher adjusted R^2 (Table 3.2). The other mean chord parameters (metrics 2 and 3) were a particularly bad fit to our data because often the mean chord was located distally. In that case, folding the wrist caused a substantial aftward shift of the estimated quarter-chord location. With this information, we calculated the relationship for every other species in our study with the exponent of 0.8 and assuming that $e^{-0.052} = 0.949 \approx 1$ as:

$$\frac{|x_{NP_{wb}}|}{c_{r_{max}}} \approx \left(\frac{|\tilde{x}_{c/4}|}{c_{r_{max}}}\right)^{0.8}. \tag{3.8}$$

We imported this relationship into our comparative analysis and computed the quarter chord position of the standard mean chord for each specimen and configuration. We checked if the

Table 3.2: **Linear model fit results for each investigated chord metric.**

Chord metric name	**Metric**	**A** (95% CI)	**B** (95% CI)	**Adjusted R^2**
root	1	0.833 (0.764, 0.902)	-0.997 (-1.015, -0.980)	0.358
mean projected	2	0.083 (0.062, 0.105)	-1.102 (-1.127, -1.077)	0.053
mean	3	0.054 (0.033, 0.074)	-1.115 (-1.145, -1.084)	0.025
mean aerodynamic	4	0.152 (0.135, 0.169)	-0.930 (-0.960, -0.900)	0.235
centroid area	5	1.349 (1.285, 1.414)	1.436 (1.310, 1.562)	0.624
standard mean	6	0.812 (0.789, 0.835)	-0.052 (-0.084, -0.021)	0.832

quarter-chord position was in front of the shoulder and if so we switched the signs of the output. This essentially reflects the exponential trend that was established for the gull wings into the positive neutral point region.

In all, this result provides insight into the aerodynamic implications of morphing however this was informed by an aerodynamic analysis of only one species for rigid wing-body configurations. It will be important for future studies to account for inter-specific differences as well as a neutral point shift due to flexibility and porosity.

3.5.2 Defining agility and stability metrics

We next asked if inertial characteristics could be used to estimate a bird's pitch agility. However, because both inertia and aerodynamics are fundamental to flight dynamics, we first used aerodynamic theory and data from a rigid gull wing [141] to obtain an estimate for the neutral point, and thus the static margin for each configuration. We developed a pitch agility metric that estimates the change of the angular acceleration about the *y*-axis ($\Delta\dot{q}$, known as the time rate of change of the pitch rate) due to a degree change in the angle of attack ($\Delta\alpha$) as:

$$\frac{\Delta\dot{q}}{\Delta\alpha} \propto \frac{\left[\left(\left(\frac{\widetilde{x}_{c/4}}{c_{r_{max}}}\right)^{0.8} c_{r_{max}}\right) - x_{CG}\right] (m^{0.12})^2 \, S_{max}}{I_{yy}}. \tag{3.9}$$

Where m is the body mass, $c_{r_{max}}$ is the maximum root chord for the specimen, S_{max} is the maximum single wing area for the specimen and x_{CG} is the center of gravity position on the *x*-axis measured from the humeral head. This equation was derived beginning from the rigid aircraft *y*-axis rotational equation of motion assuming a symmetric configuration undergoing

small disturbances [138]:

$$\Delta M = I_{yy}\Delta\dot{q}. \tag{3.10}$$

From this equation, we estimated the change in pitching moment (ΔM) with a Taylor series expansion method assuming that the largest effect is due to angle of attack and then non-dimensionalized as follows [138]:

$$\Delta M = \frac{\partial M}{\partial \alpha}\Delta\alpha \tag{3.11}$$

$$= \frac{1}{2}\rho U_\infty^2 (2S_{max}) c_{r_{max}} \frac{\partial C_M}{\partial \alpha}\Delta\alpha \tag{3.12}$$

$$= \frac{1}{2}\rho U_\infty^2 (2S_{max}) c_{r_{max}} \frac{\partial C_M}{\partial C_L}\frac{\partial C_L}{\partial \alpha}\Delta\alpha. \tag{3.13}$$

Where U_∞ is the freestream scalar velocity, and C_L and C_M are the coefficients of lift and pitching moment, respectively. Because the pitching moment slope ($\frac{\partial C_M}{\partial C_L}$) is proportional to static margin [141, 197], we estimated each configuration's neutral point using equation 3.8 (see Section 3.5). With the estimated neutral point, we calculated the static margin as:

$$static\ margin\ = -\frac{\partial C_M}{\partial C_L} = \frac{x_{CG} - \left(\left(\frac{\widetilde{x}_{c/4}}{c_{r_{max}}}\right)^{0.8} c_{r_{max}}\right)}{c_{r_{max}}}. \tag{3.14}$$

For the pitch agility metric, we incorporated a previously established allometric scaling [117] of cruise velocity ($U_\infty \propto m^{0.12}$). We assumed a constant air density (ρ) and constant lift slope ($\frac{\partial C_L}{\partial \alpha}$) across species to obtain the final proportional relationship as:

$$\Delta M \propto \left[\left(\left(\frac{\widetilde{x}_{c/4}}{c_{r_{max}}}\right)^{0.8} c_{r_{max}}\right) - x_{CG}\right]\left(m^{0.12}\right)^2 S_{max}\Delta\alpha. \tag{3.15}$$

This result was then returned to equation 3.10 and rearranged to obtain the pitch agility metric as seen in equation 3.9. Note that agility in a stable configuration indicates that the developed acceleration would tend to return the bird towards an equilibrium position.

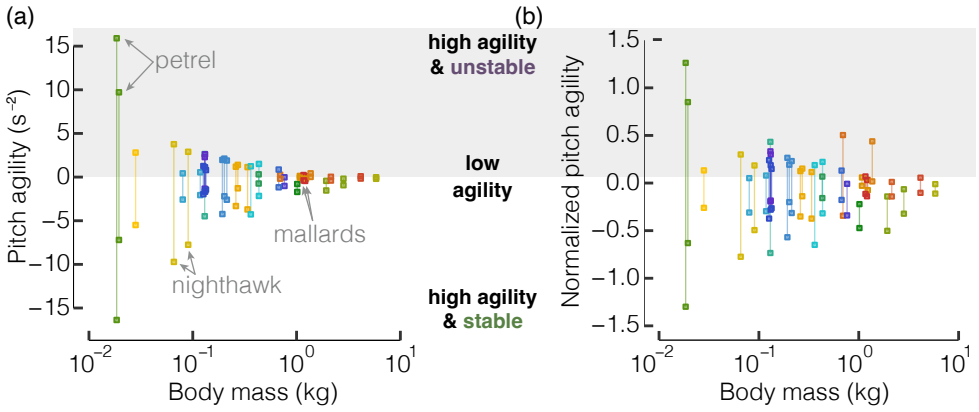

Figure 3.6: **Modern birds exhibit highly variable pitch agility characteristics.** We derived a pitch agility metric that highlights (a) that heavier birds are less agile even when (b) normalized as if the birds are flying at the same speed and have the same body length. Maximum and minimum values for each individual due to elbow and wrist ROM are plotted.

3.6 Results - Aerodynamic characteristics

We found that the pitch agility range decreases as body mass increases, which was expected because flight speed and body size scale positively with mass [117] (Fig. 3.6a, Table 3.3). These results are further driven by the static margin whose range also decreases as mass increases (Fig. 3.8a, Table 3.3). Because the pitch agility metric had units of s^{-2}, we non-dimensionalized this metric by multiplying by the square of the full bird's length divided by U_∞^2 that was approximated by $(m^{0.12})^2$. This normalization allows us to compare birds as if they are the same length and flying at the same speed, similar to non-dimensional approaches implemented in traditional aircraft studies (Fig. 3.6b) [201]. We found that the normalized agility range decreases as body mass increases (Table 3.3). Note that the linear trend of the pitch agility range with body mass remains significant even if the storm petrels are removed from the data. Incorporating the shoulder joint ROM would broaden the static margin range because the resultant neutral point shift is likely larger than the center of gravity shift as evidenced by morphing UAVs with shoulder-inspired joints [30, 202].

Table 3.3: **MCMCglmm outputs for agility and stability phylogenetic generalized linear mixed models (PGLMM).**

Dependent variable	Independent variable	Slope 95% credible intervals	*p*-value
pitch agility range	body mass	-3.50, -0.35	0.018
normalized pitch agility range	body mass	-0.29, -0.03	0.018
static margin range	body mass	-0.15, -0.02	0.010

3.7 Investigation of the evolutionary implications

Next, we asked if there is evidence of selective evolutionary pressures on avian pitch agility and stability. We investigated the static margin specifically because it is both a component of the pitch agility metric and dictates the static stability of a flying bird. We identified the configurations with the maximum and minimum static margin for each individual (Fig. 3.7) and then calculated the mean of each trait for each species (Fig. 3.8b).

3.7.1 Evolutionary modeling results

To investigate the phenotypic optimum of the pitch agility and stability traits, we independently fit both Brownian motion (BM) and Ornstein Uhlenbeck (OU) models to the absolute data using the R package geiger [203]. We assumed that all species belong to the same regime

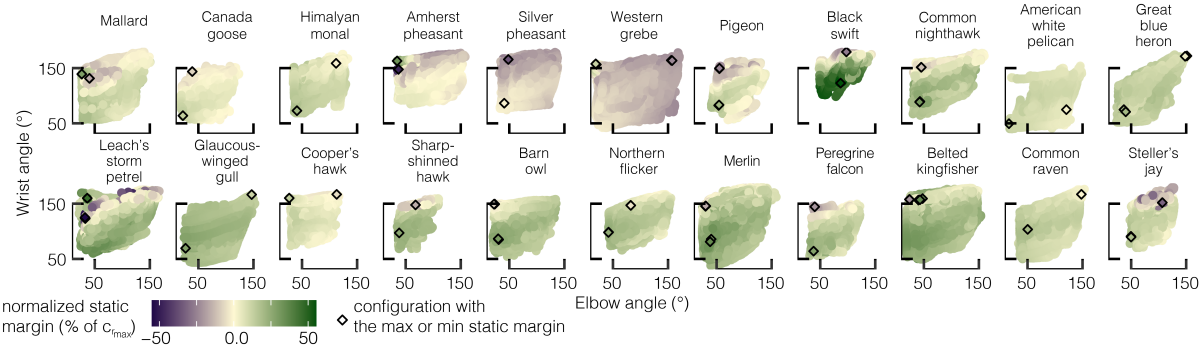

Figure 3.7: **The elbow and wrist angle configurations that yielded the maximum and minimum static margin for each species.** The ROM investigated for each species with the maximum static margin and minimum static margin identified with a black diamond on each species. Note that the diamonds are colored by the static margin.

and thus, fit single-peak evolutionary models. We found that four species were entirely stable, one species was entirely unstable, and 17 species had the capacity to shift between stable and unstable flight (Fig. 3.8b and e). Using these data, we found that an Ornstein Uhlenbeck (OU) model was significantly favored over a Brownian motion (BM) model, for both the maximum (ΔAICc = -8.24, Fig. 3.9b) and minimum static margin (ΔAICc = -5.01, Fig. 3.9c), where

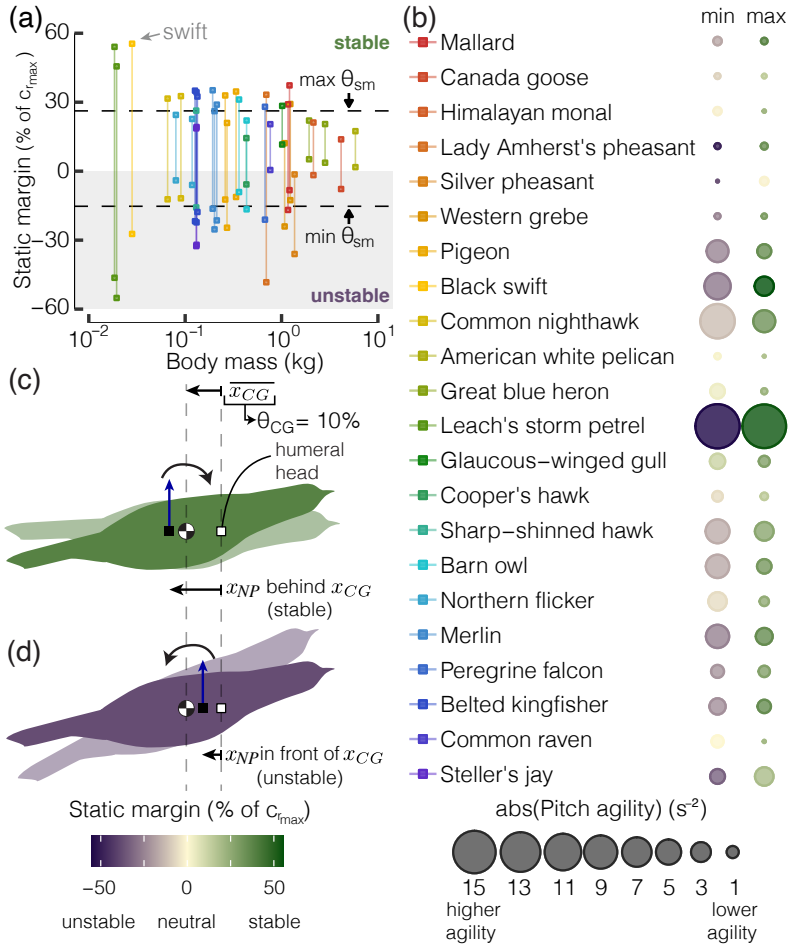

Figure 3.8: **Evolution selects for both pitch stability and instability, but modern birds exhibit highly variable pitch agility and stability characteristics.** (a) We found that heavier birds have a reduced static margin range. Maximum and minimum values for each individual due to elbow and wrist ROM are plotted. (b) The investigated species exhibited a wide variety of static margins and absolute pitch agility. Dot color and size represents the mean maximum and minimum value for each species. An Ornstein Uhlenbeck model provided evidence of selection pressures acting on an unstable minimum (dashed line: min. θ_{sm}) and a stable maximum (dashed line: max. θ_{sm}) static margin, and $\overline{x_{CG}}$ (θ_{CG}). This $\overline{x_{CG}}$ position is (c) stable if the neutral point is behind this position and (d) unstable if the neutral point is in front of this position.

AICc is the Akaike information criterion with correction for small sample sizes. Further, we found that the optimal static margin phenotype (θ_{sm}) was stable for the maximum static margin (26% of $c_{r_{max}}$, strength of selection (α_{OU}) $= 0.53$, variance (σ^2) $= 14.2 \times 10^{-3}$) whereas the optimal phenotype for the minimum static margin was unstable (-15% of $c_{r_{max}}$, $\alpha_{OU} = 0.06$, $\sigma^2 = 2.7 \times 10^{-3}$) (Fig. 3.8b). This suggests that evolutionary pressures act to maintain birds' ability to transition between stable and unstable flight. The strength of selection (α_{OU}) was relatively low, but our results were robust to measurement errors (details in Sections 3.7.2 and 3.7.3) and to a preliminary estimation of a neutral point shift due to the tail (details in Section 3.7.5). Further, an OU model was a good fit for the mean $\overline{x_{CG}}$ such that the phenotypic optimum (θ_{cg}) was 10% of the body length aft of the humeral head (ΔAICc= -8.23, $\alpha_{OU} = 0.11$, $\sigma^2 = 0.1 \times 10^{-3}$, Fig. 3.9a). The stability of this center of gravity position depends on the location of the neutral point (Fig. 3.8c and d).

3.7.2 Power analysis

Because of the smaller sample size of our study [204], we ran a Monte Carlo simulation (n = 5000) with the R package pmc [205] to validate that selecting the OU model over the BM model was appropriate (Fig. 3.9). This method returned a distribution of likelihood ratios (twice the difference of the maximum log likelihood for each model) when the traits have been simulated n times under each model. These distributions are then compared to the observed likelihood ratio (black dashed vertical lines in Fig. 3.9). For details refer to Boettiger et. al [205]. We found that the likelihood ratio predicted by a BM model was more extreme than the observed ratio for the minority of simulations ($\overline{x_{CG}}$: 0.2%, maximum static margin: 0.1%, minimum static margin: 1%). Further we had sufficient power to differentiate the two models as the majority of the simulations under the OU model fell outside of 95th percentile of the BM distribution ($\overline{x_{CG}}$: 73.8%, maximum static margin: 77.2%, minimum static margin: 67.2%). 95% confidence intervals were constructed for each reported metric of each trait (Table 3.4). Together these results provide confidence that the observed likelihood ratio of each trait is more likely to occur under an OU model than a BM model.

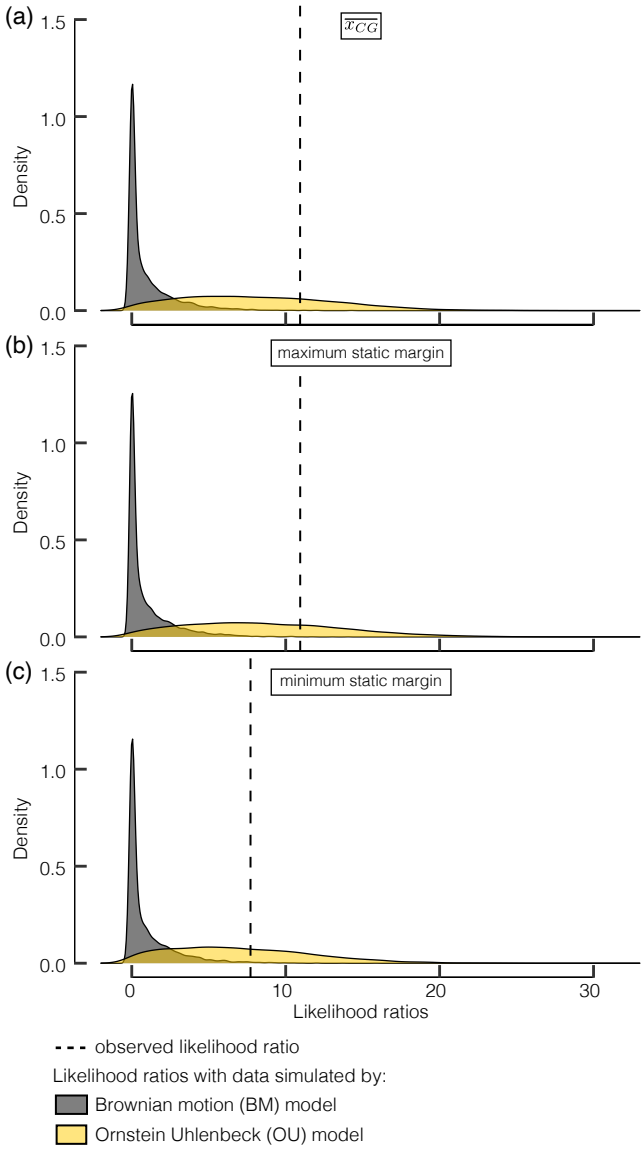

Figure 3.9: **A power analysis confirmed the validity of Ornstein Uhlenbeck (OU) models for three key traits.**We used a Monte Carlo-based method to investigate if our phylogeny provides support for the use of the OU model. This returns the distribution of likelihood ratios under each model for (a) $\overline{x_{CG}}$, (b) maximum static margin, and (c) minimum static margin. Comparing the likelihood ratios distributions produced under both a Brownian motion (BM) model (gray) and OU model (yellow) to the observed likelihood ratio (dashed black line) revealed that the OU model was a better fit for our three key traits (see methods).

3.7.3 Sensitivity analysis

Because both the pitch agility and stability metrics directly depend on x_{CG}, we investigated the sensitivity caused by shifting the combined torso and tail center of gravity forwards and aft

Table 3.4: **95% confidence intervals on the OU metrics reported for each investigated trait.**

Trait	Phenotypic optimum (θ_{trait})	Selection strength (α_{OU})	Variance (σ^2) $\times 10^{-3}$
$\overline{x_{CG}}$	-11.1%, -9.3% (of full length)	0.016, 2.718	0.02, 3.77
max. static margin	22.2%, 30.4% (of $c_{r_{max}}$)	0.017, 2.718	0.41, 81.39
min. static margin	-21.0%, -9.6% (of $c_{r_{max}}$)	0.013, 2.718	0.60, 132.86

by up to 15% of the torso. Note that for some species there was a physical limit to the ability to relocate the center of gravity while maintaining the known morphological properties and if the shifted distance was larger than 4cm we removed it from the analysis as that was assumed to be an overestimate. The final estimated shift of the relative maximum and minimum static margin is shown in Fig. 3.10. This sensitivity analysis revealed a minor effect on the parameters.

In addition, we wanted to investigate the potential effect of error in our measured center of gravity metric on our key evolutionary results. To this end, we used a custom bootstrapping

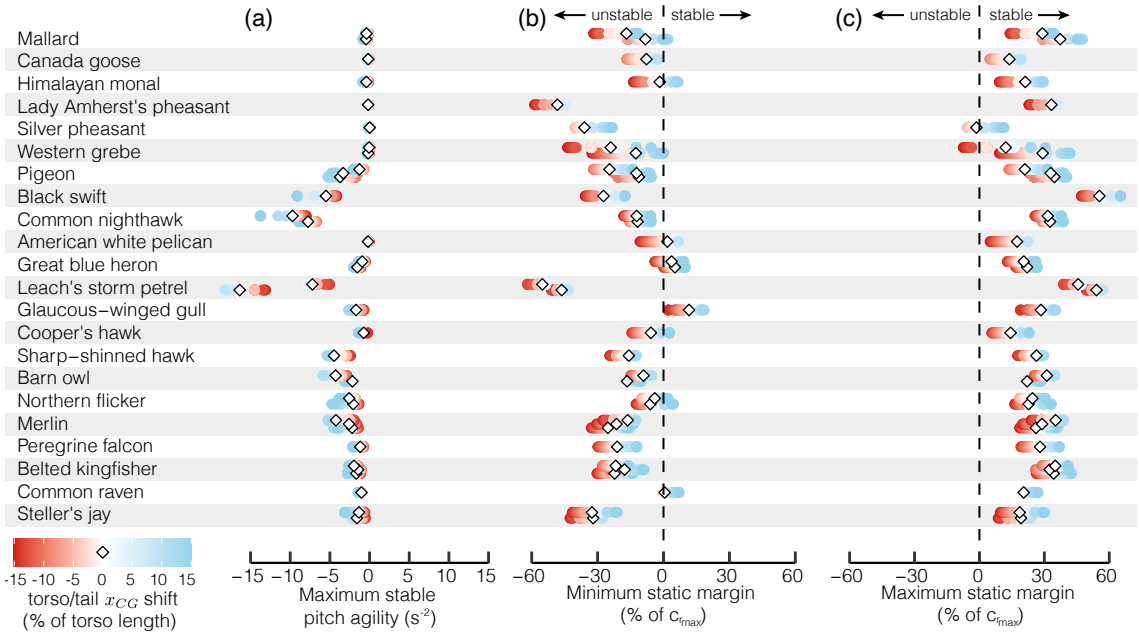

Figure 3.10: **Conservative measurement sensitivity analysis revealed a minimal effect on pitch stability and agility metrics.** We assumed that experimental error on the center of gravity measured for the torso and tail was $\pm$15% of the torso length (up to a maximum of 4cm) and recalculated the (a) maximum pitch agility for stable flight (most negative values in Fig. 3.8 a), (b) minimum and (c) maximum static margin. The estimated error ranges from panels b and c informed the bootstrapping analysis in Fig. 3.11.

code (n = 5000) and randomly sampled (with replacements) from each specimen's center of gravity error range used for the sensitivity analysis to recalculate the mean value of the minimum and maximum static margin for each species. With each of these new trait distributions, we re-fit an OU model and extracted the optimal phenotype (Fig. 3.11). We found that even allowing for this substantial center of gravity error, all minimum static margin cases had an unstable optimum and all maximum static margin cases had a stable optimum (Fig. 3.11). Note that this analysis is equivalent to accounting for the same magnitude shift in the neutral point with a fixed center of gravity as well as accounting for possible inter-specific variation within the error bounds shown in Extended Fig. 3.10.

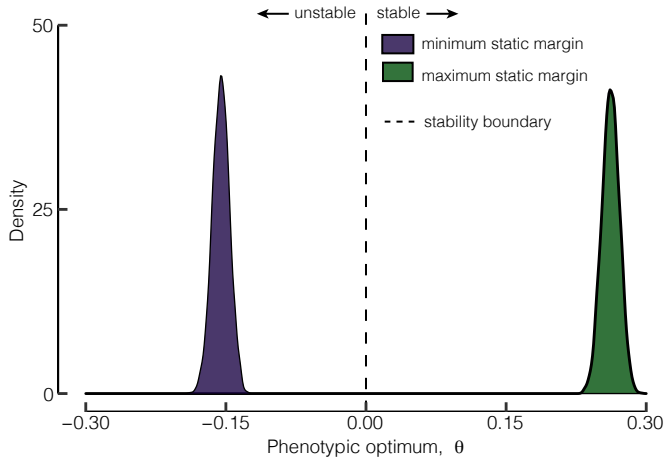

Figure 3.11: **Bootstrapping our results within the conservative center of gravity measurement error supported our results.** We used a Monte Carlo method to investigate the impact of center of gravity measurement error on the phenotypic optima for the maximum static margin (green) and minimum static margin (purple). Our results for a stable maximum and an unstable minimum are confirmed with over a 95% confidence interval.

3.7.4 Sensitivity of the neutral point approximation

We verified that our key static margin findings were not substantially affected by the exponent selected for the neutral point (Eqn. 3.8) by performing a sensitivity analysis. We found that despite varying the exponent from 0.7 to 1.1, all the optimal phenotypes for maximum static stability were stable whereas the optimal phenotypes for minimum static stability were unstable. Specifically, as the scaling parameter increased, we found that the optimal phenotype for the maximum static margin shifted from 31% to 15% of the maximum root chord and the

minimum static margin shifted from -13% to -19%. Thus, increasing the exponent effectively serves to shift the results towards instability but our evolutionary findings remain supported. As the gull represents the only species with which we are able to estimate the relationship between geometric parameters and the neutral point across the full range of flexion and extension, we selected to proceed with the gull-informed exponent of 0.8.

3.7.5 Effects of including a furled tail

In Section 3.5, we established a morphological-based metric to estimate the neutral point of the wing-body configuration. The neutral point of the wing-body configuration is assumed to be a close approximation to the total flyer's neutral point because in our study we assumed that the tail is furled and thus generates minimal lift. In practice, any additional surface area on a flyer will affect its aerodynamic properties. Further, on traditional aircraft the tail is a major contributor to the overall stability due to the tail aerodynamic center always remaining aft of the CG. Proper estimation of the tail contribution requires a detailed analysis of the aerodynamics of the tail and body-wing-tail interactions, but it is possible to make a preliminary estimation the tail contribution with aerodynamic theory. We used a standard equation [138, 140, 206] to estimate the tail's effect on the neutral point to the wing-body configurations ($x_{NP_{wb}}$) as:

$$x_{NP} = x_{NP_{wb}} - \frac{C_{L_{\alpha_t}}}{C_{L_\alpha}} \left(1 - \frac{d\epsilon}{d\alpha}\right) \eta_t V_H c_m \tag{3.16}$$

Where the tail volume coefficient is defined as:

$$V_H = \frac{l_t S_t}{c_m S_w} \tag{3.17}$$

Note that mean chord (c_m) introduced in equation 3.17 is canceled out in equation 3.16. For plotting purposes, we selected to use each individual specimen's mean value of c_m across all morphed configurations. This allows a comparable metric to the traditional aircraft metrics published by Raymer [206]. We estimated that the tail aerodynamic center was at 25% of the tail length, although future work will need to account for the expected shift due to low tail aspect ratio. Figure 3.12 shows the estimated tail volume per individual as a function of the

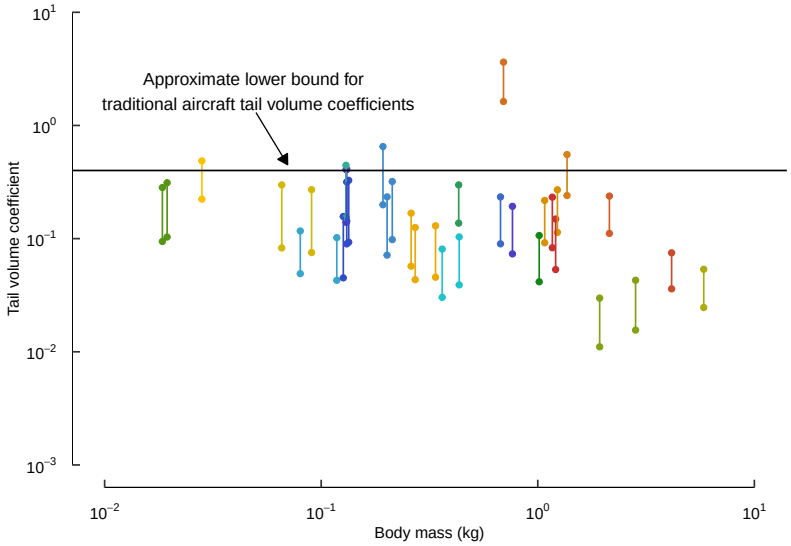

Figure 3.12: **Tail volume coefficients as a function of the body mass for the investigated specimens.**

overall body mass. The range for each specimen is largely caused by the changes in the total wing area (S_w). Of note, traditional aircraft tail volume coefficients usually vary between 0.4 (black horizontal line, Fig. 3.12) to 1 and many of these bird tail volumes are substantially lower [206, 207].

Next, we must estimate the factors that multiply the tail volume coefficient in equation 3.16. First, it is known that the dynamic pressure at the tail will be lower than that at the wing due to the resultant wing wake, which indicates that η_t is less than one [138]. Next, because the tail will have a substantially lower aspect ratio than the wing while it is furled, we estimated that the lift-slope of the tail will be lower than that of the wing (i.e. $\frac{C_{L_{\alpha_t}}}{C_{L_\alpha}}$ is less than one). Finally, $\frac{d\epsilon}{d\alpha}$ is also always below one due to the downwash from the main wing [138, 206]. For traditional aircraft in subsonic flight, this value decreases as the wing aspect ratio and taper ratio increase and as the distance between the tail aerodynamic center and the center of gravity increases [206]. Each of these characteristics varies substantially across bird species. Because $\frac{d\epsilon}{d\alpha}$ is subtracted from one in equation 3.16, decreasing $\frac{d\epsilon}{d\alpha}$ will effectively increase the tail contribution to the neutral point shift. Collectively, because all three discussed multiplying factors are expected to be less than one, we selected each value to be 0.9 for birds: $\frac{C_{L_{\alpha_t}}}{C_{L_\alpha}}(1-\frac{d\epsilon}{d\alpha})\eta_t \approx 0.73$. We selected 0.9 as it is expected to overestimate this multiplying factor,

which will return the most aft neutral point shift and provide a highly conservative view on the validity of our evolutionary results.

With these inputs we solved equation 3.16 and 3.14 to obtain the maximum and minimum static margin for each specimen and then calculated the mean value for each species. Next, we fit a Ornstein Uhlenbeck (OU) model to the data following the similar procedure detailed in Section 3.7. This analysis revealed that even when accounting for the tail's effect on the neutral point there is evidence that evolution selects for a stable maximum static margin (38% of $c_{r_{max}}$, $\alpha_{OU} = 2.718, \sigma^2 = 0.255$) and an unstable minimum static margin (-6% of $c_{r_{max}}$, $\alpha_{OU} = 0.395, \sigma^2 = 0.022$). As expected, the phenotypic optimum values of both the maximum and minimum static margin models shifted towards increased stability, but there was evidence of stronger selection pressure (α_{OU}) than in the wing-body configurations alone. As with our key results, this again suggests that birds have the ability to shift their neutral point in front of their center of gravity to balance the positive tail lift that is required for weight support in slow gliding flight [208]. It is important to highlight that we expect inter-specific variation within the multiplying parameters and that the selected value substantially overestimates the tail's contribution and likely results in a more stable output. In all, these results are expected to provide a preliminary estimation of the tail's contribution.

3.8 Limitations

It is important to highlight that further work is required to incorporate the inter- and intra-specific aerodynamic capabilities, shoulder and tail ROM, and *in vivo* configurations to definitively confirm the optimal phenotype(s) for static pitch stability. We expect that the shoulder joint will enhance the available pitch control and the ability to shift between modes due to an increased static margin range; the extent of this enhancement will depend on each species' shoulder ROM [30, 138, 202]. Future work is also required to extend this analysis into the roll and yaw axes to discuss lateral agility and stability, which will need to account for aerodynamic and inertial coupling [138]. Finally, 23% of the species in our study were unable to shift between stable and unstable modes with the elbow and wrist alone, and thus there are many combinations of stability characteristics within modern birds.

3.9 Conclusion

Although studies have suggested that modern birds may be capable of stabilized flight [128, 137, 141], it is widely believed that birds have evolved to be unstable in pitch to enhance maneuverability [178]. Our results offer a new perspective on the evolution of avian flight: *evolutionary pressures may be maintaining the ability to shift between stable and unstable configurations*. Elbow and wrist flexion and extension alone offers birds the capacity to shift between these pitch stability modes. But, if and when a flying bird does shift between these modes remains to be seen. As highlighted by Thomas and Taylor [137], dynamically switching between stable and unstable modes likely requires substantially different control algorithms and thus, switching between these modes would necessitate a complex flight control system. Further, our findings offer insight on how birds perform slow glides with positive tail lift [208]. By maintaining the capacity to relocate the wing-body neutral point in front of the CG, birds may achieve an equilibrium, albeit unstable, flight condition.

In summary, our results revealed that elbow and wrist ROM had a small relative effect on the center of gravity location and pitch inertia, but had a substantial effect on the roll and yaw inertia. Although inter- and intra-specific variation was apparent, we found that the measured range of wrist and elbow motion alone is sufficient to enable switching between stable and unstable flight in 17 out of 22 bird species. Further, an evolutionary analysis showed that the phenotypic optimum maximum and minimum static margin supports the ability to transition between stable and unstable flight, suggesting the need for a complex flight control system. Collectively, investigating the inertial characteristics of flying birds throughout elbow and wrist ROM brings us one step closer to establishing a fundamental theory to quantify and then evaluate avian maneuverability.

Chapter 4

Gull Wing Joints Control Dynamic Stability

Flying may not be all plain sailing, but the fun of it is worth the price.

– Amelia Earhart

4.1 Summary

Birds perform astounding aerial maneuvers by actuating their shoulder, elbow, and wrist joints to morph their wing shape. This maneuverability is desirable for similar-sized UAVs and can be analyzed through the lens of dynamic flight stability. Quantifying avian dynamic stability is challenging as it is dictated by aerodynamics and inertia, which must both account for birds' complex and variable morphology. To date, avian dynamic stability across flight conditions remains largely unknown. Here we fill this gap by quantifying how a gull can use wing morphing to adjust its longitudinal dynamic response. We found that it was necessary to adjust the shoulder angle to achieve trimmed flight, and that most trimmed configurations were longitudinally stable, except for configurations with high wrist angles. Our results showed that as flight speed increases, the gull could fold its wings or sweep its wings backwards to trim. Further, a trimmed gull can use its wing joints to control the frequencies and damping ratios of the longitudinal vibrational modes. We found a more damped phugoid mode than similar-sized UAVs, possibly reducing speed sensitivity to perturbations such as gusts. Although most configurations had controllable short period flying qualities, the heavily damped phugoid mode indicates a sluggish response to control inputs, which may be overcome while maneuvering by morphing into an unstable flight configuration. Our study shows that gulls use their shoulder, wrist, and elbow joints to negotiate trade-offs in stability and control and highlights the path forward for designing UAVs with avian-like maneuverability.

4.2 Background

Imagine UAVs performing social aerial aerobatics like ravens [209], rapidly diving like gannets [210], and skillfully maintaining their position in high wind and gusty conditions like kestrels and gulls [37, 211]. These nature-documentary-worthy feats often exceed the maneuverability of modern comparable UAVs, especially non-rotary designs [129]. The ability for UAVs to effectively maneuver is becoming increasingly important as UAVs are more often operating close to or within crowded environments, such as urban centers [31, 212].

To determine how to best improve UAV maneuverability based on insights from birds, we must first quantify maneuverability. Maneuverability is broadly defined as the ability to change the magnitude and/or direction of a flyer's velocity vector [19, 20]. Although, there are multiple ways to evaluate flight maneuverability, many traditional methods quantify an aircraft's stability and control characteristics across relevant flight conditions [138, 213]. This is often done by linearizing the governing equations of motion about an equilibrium condition (trim state) and solving the resultant eigenvalue problem to extract information about the aircraft's response to small perturbations [138, 139].

For complete stability, the flyer must be both statically and dynamically stable. A flyer is statically stable if after a disturbance, the flyer's initial tendency is to return towards its trim state (time-invariant), while a flyer is dynamically stable if it eventually returns to its trim state after a disturbance (time-variant). Static stability is a necessary but insufficient condition for dynamic stability. In the longitudinal plane (x-z plane, Fig. 4.1), the dynamic response is commonly characterized by two superimposed modes: the short period and phugoid. For traditional aircraft, the short period mode is a heavily damped, high frequency vibration in the angle of attack and pitch rate (Fig. 4.1a), while the phugoid mode is a lightly damped, low frequency response in the flight speed and pitch angle (Fig. 4.1b) [138]. The associated damping ratio and natural frequency of these modes dictate how "sluggish" or "sensitive" an aircraft is to control inputs, and are used to define an aircraft's flying qualities [139, 214–218].

This stability-based approach to quantifying maneuverability requires knowledge of the aerodynamic and inertial characteristics across all flight conditions and configurations. Obtaining this data for birds is challenging because of their complex and variable geometries. As

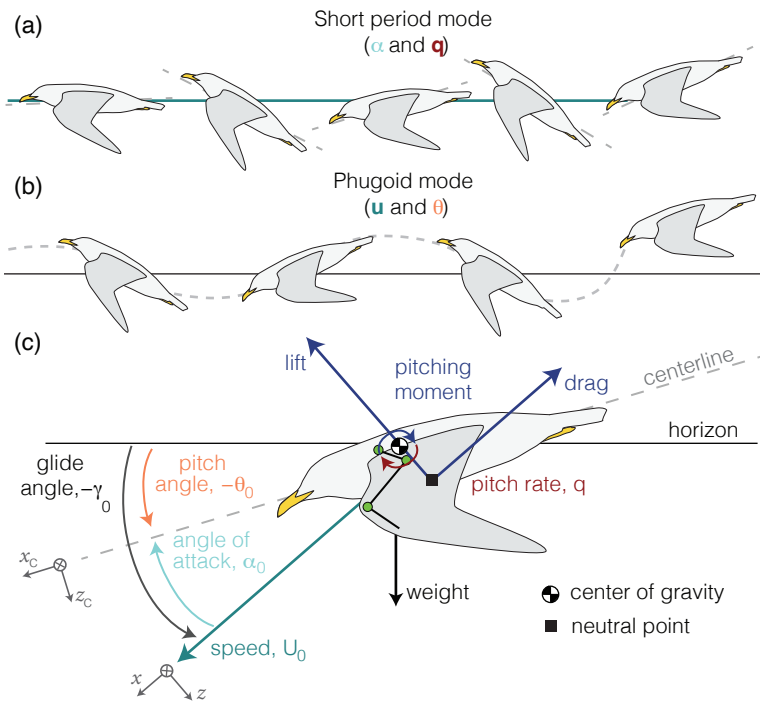

Figure 4.1: **In the longitudinal plane, gliding flight dynamics are usually dominated by the short period and phugoid modes.** (a) The short period mode largely affects the angle of attack (α) and pitch rate (q) and is visualized by the oscillation of the center line (dotted grey line) about the fixed velocity vector (solid green line). (b) The phugoid mode largely affects the flight speed (u) and pitch angle (θ) and is visualized by the oscillation of the centre line (dotted grey line) about the fixed horizon (solid black line). (c) Side view of gull with key flight parameters illustrated.

a result, there are few studies that have quantified the dynamic flight response of gliding birds throughout wing morphing. Instead, studies of gliding maneuverability often leverage observations of live birds by tracking and analyzing their morphology and flight path [177, 219, 220]. For example, in their thesis Durston [219] used live birds, 3D printing techniques, and X-ray computed tomography (CT scanning) to show that three species of raptors are dynamically unstable in the longitudinal axis while gliding towards their handler. Although this work provides the first detailed investigation of avian dynamic stability, the results are limited to the wing shapes and behaviors that the birds used during the recorded flights.

Here, we investigated a gull's longitudinal dynamic stability across the full range of elbow and wrist flexion and extension used in gliding flight. Our dynamic analyses were informed our two previous studies on hybrid glaucous-winged (*Larus glaucescens*) $\times$ western (*Larus*

occidentalis) gulls. The aerodynamic results were obtained with an open-source numerical lifting line method (MachUpX) following similar procedures to Chapter 2 [141] and the inertial characteristics were obtained with an open-source method that models birds as a composite of simple objects (AvInertia) [142] following similar procedures to Chapter 3. As Chapter 2 showed that gull wing-body configurations were unable to trim at a fixed shoulder angle with no sweep or dihedral, we incorporated a furled (unspread, Fig. 4.2b) tail and two new degrees of freedom: shoulder dihedral (Fig. 4.2a) and sweep angle (Fig. 4.2b). By coupling these extended aerodynamic and inertial results with the traditional stability-based dynamic analysis framework, we derived the small perturbation equations of motion across the *in vivo* range of motion of the elbow and wrist for a gliding gull [128]. Next, we investigated the free vibrational response of the gull with its wings in each morphed configuration, which allowed us to extract the natural frequencies and damping ratios of the system. Finally, to visualize the effect of wing morphing on the gull's time response, we investigated two types of simplified gusts: 1) a simplified transverse-gust modelled by an initial offset in the angle of attack and 2) a simplified streamwise-gust modelled by an increase in the forward speed with a 1-cosine profile [214].

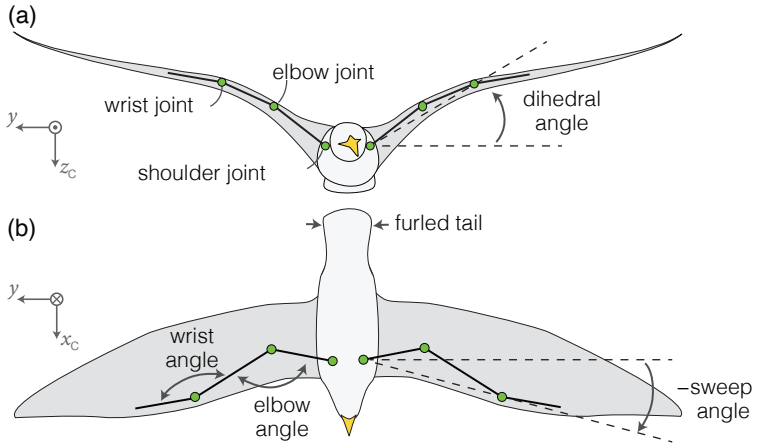

Figure 4.2: **Gulls can morph their wings to adjust key flight parameters.** (a) Front view of gull, visualizing the shoulder dihedral angle where a positive angle is an upwards deflected wing. (b) Dorsal view of gull, visualizing the shoulder sweep angle where positive is a backwards swept wing. Elbow and wrist angles are always positive with higher angles as the wing extends.

4.3 Methodology

We developed the governing equations of motion for a gliding gull in the longitudinal plane. We assumed a rigid, non-porous, symmetric gull undergoing small perturbations in a quasi-steady state. These assumptions allowed us to evaluate longitudinal (i.e., pitch) characteristics separate from the lateral (i.e., roll and yaw) characteristics and obtain a state-space representation of the longitudinal governing equations. We formulated the equations of motion following procedures similar to those outlined in aeronautical texts [138, 139]. Any deviations from these texts are due to assumptions on the aerodynamic derivatives and are detailed in the following sections. Note that although we modeled the bird as a rigid body, we accounted for a change in the aerodynamic and inertial characteristics between each different wing configuration. This approach of solving the dynamic response for each fixed configuration independently is similar to the approach used to establish the operating parameters for aircraft across different flight conditions independently [139].

4.3.1 Frames of reference

There are four frames of reference to consider when discussing traditional aircraft dynamics. First, we require an inertial frame to resolve the applicable equations of motion. We selected an earth-fixed frame as our inertial frame due to the slow gliding speeds of birds [122, 138]. Next, the body-fixed frame is often defined so that the origin is fixed on the center of gravity of the glider with the x-axis pointing out of the nose of the aircraft, the z-axis pointing downwards from the aircraft's ventral surface and the y-axis pointing towards the right wing tip (Fig. 4.1c, x_c-y-z_c axis). This body-fixed frame is defined relative to the inertial frame by the traditional 3-2-1 Euler angles $\phi, \theta,$ and ψ. Within this body axis, the traditional angular velocities are defined: roll rate (p), pitch rate (q) and yaw rate (r).

From the body axis, we can define a stability frame of reference which is defined by a rotation about the body's y-axis (known as the angle of attack, α) so that the new stability x-axis is in line and opposite to the incoming wind velocity (Fig. 4.1c, x-y-z axis). Finally, we can define a wind frame of reference by rotating about the stability z-axis (known as the

sideslip angle, β) until the new wind x-axis is directly in line and opposite to the incoming wind velocity. It is within the wind frame of reference that the resultant aerodynamic loads can be decomposed into lift (L), drag (D), side force, pitch (M), roll, and yaw.

To simplify the formulation of the equations, we made a few key assumptions. First, we assumed that when trimmed and at $t = 0$, the body-fixed frame of reference is aligned with the stability axis (i.e. x_c is parallel to x). This ensures that the entire incoming velocity is equal and opposite to the x-axis. Next, to properly implement a rigid body dynamic analysis, we assumed that the bird maintains a constant configuration as it undergoes perturbations, which ensures a constant moment of inertia and center of gravity. In addition, we modeled only a single gull specimen. We selected to use the specimen that was used to extract inertial measurements for Chapter 3 [142].

4.3.2 Defining the dynamic response

With these initial assumptions, we implemented a Newton-Euler approach [138, 139] to obtain the classic equations for a symmetric configuration of a rigid body aircraft within the body axes:

$$\begin{aligned}
F_x &= m(\dot{U} + qW - rV) \\
F_y &= m(\dot{V} + rU - pW) \\
F_z &= m(\dot{W} + pV - qU) \\
M_x &= \dot{p}I_{xx} - I_{xz}(pq + \dot{r}) + qr\left(I_{zz} - I_{yy}\right) \\
M_y &= \dot{q}I_{yy} + I_{xz}\left(p^2 - r^2\right) + rp\left(I_{xx} - I_{zz}\right) \\
M_z &= \dot{r}I_{zz} - I_{xz}(\dot{p} - qr) + pq\left(I_{yy} - I_{xx}\right)
\end{aligned} \tag{4.1}$$

To investigate the dynamic stability about the equilibrium condition, we assumed a symmetric flight condition (i.e., $V = p = q = r = \phi = \psi = \beta = 0$) and that the gliding bird would only experience small perturbations about a given equilibrium condition, known as the

trim point (notified with a subscript of 0), defined as:

$$\begin{aligned} U &= U_0 + \Delta U & q &= \Delta q & F_x &= \Delta F_x \\ V &= \Delta V & r &= \Delta r & F_z &= \Delta F_z \\ W &= \Delta W & p &= \Delta p & M_y &= \Delta M_y \end{aligned}$$

For this small disturbance model any higher order terms (such as $\Delta q \Delta W$) are assumed to be negligible. These assumptions reduced equation 4.1 to:

$$\begin{aligned} \Delta F_x &= m(\Delta \dot{U}) \\ \Delta F_z &= m(\Delta \dot{W} - U_0 \Delta q) \\ \Delta M_y &= \Delta \dot{q} I_{yy} \end{aligned} \tag{4.2}$$

Note that decoupling the longitudinal equations from the lateral equations is only an appropriate assumption if we limit the glider to symmetric flight and low magnitude maneuvers within the longitudinal axis [138]. Next, the translational velocity components can be rearranged to simplify their formulation as:

$$\begin{aligned} u &= \frac{\Delta U}{U_0} \\ w &= \frac{\Delta W}{U_0} = \sin(\Delta \alpha) \approx \Delta \alpha \end{aligned}$$

This leads to the final form of the small disturbance longitudinal equations as:

$$\begin{aligned} \Delta F_x &= m(U_0 \dot{u}) \\ \Delta F_z &= m(U_0 \Delta \dot{\alpha} - U_0 \Delta q) \\ \Delta M_y &= \Delta \dot{q} I_{yy} \end{aligned} \tag{4.3}$$

Because there is a dependence of the forces on the pitch angle (θ) there are effectively four unknowns and only three equations. Therefore, these equations are traditionally supplemented by the definitional relationship:

$$\Delta \dot{\theta} = \Delta q \tag{4.4}$$

The final steps now include determining the inertial and aerodynamic characteristics that are required prior to solving the system represented by equations 4.3 and 4.4.

4.3.3 Determining the trim states

The solution of this linear dynamic system requires an equilibrium condition or trim point. Trim is defined so that $F_{x_0} = F_{z_0} = M_{y_0} = 0$. Evaluating the free body diagram shown in Fig. 4.1c assuming the stability axis is aligned with the body-fixed axis at $t = 0$, allows us to write the full trimmed equations as:

$$\begin{aligned} F_{x_0} &= -D_0 - mg\sin(\gamma_0) = 0 \\ F_{z_0} &= -L_0 + mg\cos(\gamma_0) = 0 \\ M_{y_0} &= 0 \end{aligned} \tag{4.5}$$

These equations show that to trim while supporting the glider's weight during flight, there must be a positive lift force to balance out the opposing body weight when the pitching moment is equal to zero. However, in Chapter 2 we found that wing-body configurations were unable to trim when the wings were held at a shoulder angle with 0° dihedral and 0° sweep [141] (Fig. 4.2). These configurations could not trim because they generated a negative zero-lift pitching moment and a negative pitch stability derivative, thus there was no angle of attack that generated positive lift while the pitching moment was zero, which is necessary to trim.

However, the existence of a trim state is necessary for most stability analyses. To address this issue, we first adjusted the model to include a furled, static tail (Fig. 4.2b). The tail was modeled as a flat, thin, rectangular wing behind the body with a NACA 0006 airfoil and dimensions based on previously obtained furled tail measurements from the same gull species [142]. We found that the tail had a minor stabilizing effect but alone was not sufficient to trim. We expect that the tail will have a larger impact when spread and/or if it is rotated at an incidence angle relative to the body, like an aircraft's elevator.

As gulls are capable of gliding with their tail furled, we next included two new degrees of freedom: the sweep and dihedral angle at the shoulder joint (Fig. 4.2). We investigated setting the shoulder dihedral angle at 0°, 10°and 20° and the shoulder sweep angle at -20°, -10°, 0°,

10°, and 20°. Because these new parameters required 15-fold more configurations to be tested, we sub-sampled the elbow and wrist configurations that we ran in MachUpX to 200, down from 1031 in the previous aerodynamic study [141]. We ensured that the configurations were equally distributed by binning in increments of 5° of elbow angle by 5° of wrist angle and randomly selecting one configuration from each bin. In addition, to increase the convergence speed for these complex wing shapes, we implemented a custom line search that leverages an inverse parabolic interpolation [221] to calculate the optimal relaxation factor for each iteration of MachUpX's Newton method [152, 154]. We verified that this update returned the same converged result as MachUpX's fixed relaxation factor. In addition to the updated aerodynamic results, we used outputs from our previous inertia study [142] to recompute the center of gravity and moment of inertia of each wing configuration allowing for the new degrees of shoulder motion (see Section 4.3.4 for details).

Estimating aerodynamic coefficients

Because the modeled gull was not the same individual used to estimate the aerodynamic parameters, we extracted the coefficient of lift (C_L) and pitching moment (C_M) from the numerical lifting-line method. Note that these are similar to the coefficients calculated in Chapter 2 but we decided to not use the "morph" subscript for brevity. Further in this chapter, the coefficient of pitching moment was non-dimensionalized with the specimen's maximum root chord rather than the wing-body mean chord. In Chapter 2, we found that the numerical results best agreed with experimental data within the expanded uncertainty range for angles of attack below 5° [141]. Therefore, in this work we limited our aerodynamic analysis to configurations that could achieve a trimmed configuration below 5°. In addition, numerical results were limited to angles of attack greater than or equal to -10° to reduce the amount of models.

To extract the aerodynamic coefficients for the lift and pitching moment, we used linear models fit to the outputs from MachUpX as:

$$C_L = A_0 + A_1 e + A_2 w + A_3 \alpha + A_4 ew + A_5 e\alpha + A_6 w\alpha + A_7 ew\alpha + A_8 \alpha^2 + A_9 \alpha^3 + A_{10} e^2 + A_{11} w^2 + A_{12} w^3 + A_{13} \Lambda + A_{14} \Gamma + A_{15} \Lambda\alpha + A_{16} \Gamma\alpha \quad (4.6)$$

$$C_M = B_0 + B_1 e + B_2 w + B_3 C_L + B_4 ew + B_5 eC_L + B_6 wC_L + B_7 ewC_L + B_8 \Lambda + B_9 e\Lambda + B_{10} w\Lambda + B_{11} ew\Lambda + B_{12} e\Lambda C_L + B_{13} w\Lambda C_L + B_{14} ew\Lambda C_L + B_{15} \Lambda C_L + B_{16} e^2 + B_{17} e^3 + B_{18} w^2 + B_{19} \Gamma + B_{20} \Gamma C_L \quad (4.7)$$

Where α is the angle of attack, e is the elbow angle, w is the wrist angle, Γ is the shoulder dihedral angle, and Λ is the shoulder sweep angle. These models allow for interactive effects between the key joint angles. The linear model coefficients (A_i and B_i) were determined using a linear model fit in R and exported into the Python dynamic analysis code. The models had an adjusted R^2 value of 0.87 and 0.91, respectively. The linear models agree with the forms determined in Chapter 2 [141] but were updated to include the effects of the shoulder sweep and dihedral angle.

Note that the coefficient of pitching moment was adjusted to be calculated about the center of gravity for each specific configuration. This required the center of gravity location for the specimen used for the aerodynamic results. Thus, we assumed that the center of gravity of the aerodynamic specimen would be located at the same distance from the shoulder joint as the gull specimen used in the data analysis. This value ranged between 2.7 to 5.8 cm backwards, and 0.00 to 0.02 cm downwards from the shoulder joint, depending on the wing joint angles. This location was then used as the origin for recalculating the pitching moment coefficient.

We validated the fit of these models by estimating the lift and pitching moment of the experimental data. We found that the average absolute error between the linear model prediction and the experimental measurement was 0.015 for the coefficient of pitching moment and 0.082 for the lift coefficient. In addition, we found that the average absolute error between the linear model prediction and the numerical result was 0.012 for the coefficient of pitching moment and 0.058 for the lift coefficient. These results highlight that there is error between our model fit and both the experimental and numerical results. We investigated using machine learning regression techniques to improve the model predictions however, there was no significant reduction in the error. As the overall error is relatively low, we decided to proceed with our analysis, however improved model fits will improve the accuracy of our methods for future work.

Next, we used a different approach for the drag because MachUpX drag predictions did

not agree well with our experimental results for wing configurations that were heavily swept backwards [141]. Therefore, we estimated the coefficient of drag (C_D) directly from the experimental data as:

$$C_D = D_0 + D_1 e + D_2 w + D_3 \alpha + D_4 \alpha^2 + D_5 e\alpha + D_6 w\alpha + D_7 e\alpha^2 + D_8 w\alpha^2 \tag{4.8}$$

This model had an adjusted R^2 value of 0.89 and was used to estimate the drag for each wing configuration. We found that the average absolute error between the linear model prediction and the experimental measurement was 0.014 for the drag coefficient. Note that we did not include the effect of shoulder sweep and dihedral in this model. This is because the experimental results were only obtained for nine wings with a single fixed shoulder configuration. Therefore, throughout this work we effectively assumed that the effect of the shoulder sweep and dihedral angles on the drag force is negligible. For this reason, we limited the maximum angles for the shoulder to 20° to minimize the effects on the drag production. Future research is necessary to investigate the role of how the shoulder angle variation on complex gull wing shapes will affect the drag force.

Trimmed configurations

With the linear models for each aerodynamic coefficient (equations 4.6, 4.7, and 4.8), we reformulated equation 4.5 to equation 4.9. This system of equations allowed us to calculate the trim angle of attack (α_0), trim speed (U_0), and trim glide angle (γ_0) (Fig. 4.1c). We iterated through all possible combinations of elbow, wrist, and shoulder angle in the *in vivo* gull gliding range to calculate the trim position of each configuration (23). The elbow angle was varied from 86° to 164° (Δ2°), wrist angle from 106° to 178° (Δ2°), sweep angle from -20° to 20° (Δ5°), and dihedral angle from 10° to 20° (Δ5°).

$$\begin{aligned} 0 &= -\frac{1}{2}\rho {U_0}^2 S C_D - mg\sin(\gamma_0) \\ 0 &= -\frac{1}{2}\rho {U_0}^2 S C_L + mg\cos(\gamma_0) \\ 0 &= \frac{1}{2}\rho {U_0}^2 S c C_M \end{aligned} \tag{4.9}$$

Where ρ is the air density, S is the maximum wing-body area across all morphed configura-

tions, c is the maximum wing root chord across all morphed configurations, and m is the mass. To ensure compatibility across all metrics, the reference area, chord, and mass are all from one gull specimen with 0° shoulder sweep and dihedral angle that was investigated in our previous inertial study [142]. Similar to the derivation of the linear models, we limited our outputs to configurations that could trim at $\alpha_0 < 5°$ because MachUpX best matched the experimental data at low angles of attack [141]. If a configuration with a given combination of joint angles could not trim within our set parameter space, it was not included in the analysis.

We found that increasing the shoulder dihedral angle and sweeping the wings forward allowed more wing configurations to trim due to an increased zero-lift pitching moment. Because we found that the majority of elbow and wrist configurations could trim at 20° dihedral with forward swept wings, we limited our results to these shoulder angle parameters for the remainder of the study. Note that higher dihedral angles would allow all combinations of elbow and wrist angles to trim, but we limited our analysis to 20° to minimize the effects on drag estimation. Even with these limitations some of the configurations required extremely steep trim glide angles (γ_0), likely closer to terminal velocity than true gliding flight. Therefore, we limited our results to configurations that had $\gamma_0 < 45°$. In total, 1457 configurations both satisfied our imposed limitations and were able to trim (Fig. 4.3F).

4.3.4 Inertial characteristics

The key inertial characteristics for the longitudinal dynamic response are the mass (m), center of gravity, and moment of inertia about the y-axis (I_{yy}). We determined these inertial characteristics using the gull specific outputs from Chapter 3 [142] and expanded the results to account for the shoulder sweep and dihedral angle of each tested configuration. To do this, we first recalculated the location of the center of gravity relative to the shoulder joint for each morphed wing configuration. This location is important as it must be used as the new origin for the pitching moment and moment of inertia.

Next, to adjust the moment of inertia, we extracted the wing-only inertial value, rotated the wing about the shoulder joint to the appropriate dihedral and sweep angles and added it back to the rest of the body moment of inertia. We then shifted the resultant moment of inertia so that the origin was at the newly determined center of gravity.

Because we wanted to investigate any general wing configuration, we fit a linear model to the final moment of inertia calculated about the center of gravity. The elbow, wrist and shoulder sweep and dihedral angles were the explanatory variables within this model and interaction terms were included. This model was used to extract the final moment of inertia for each wing configuration and had an adjusted R^2 of 0.999. We found that the average absolute error between the linear model prediction and the numerical estimates was 6.12×10^{-5} kg-m^2 for the moment of inertia.

4.3.5 Aerodynamic characteristics

The key aerodynamic characteristics are encapsulated by the left-hand side of equation 4.3. Following traditional aeronautical methods we recast these variables using a Taylor series expansion as follows:

$$\begin{aligned}
\Delta F_x &= \frac{\partial F_x}{\partial u}u + \frac{\partial F_x}{\partial \alpha}\Delta\alpha + \frac{\partial F_x}{\partial \dot{\alpha}}\Delta\dot{\alpha} + \frac{\partial F_x}{\partial q}\Delta q + \frac{\partial F_x}{\partial \theta}\Delta\theta + \cdots \\
\Delta F_z &= \frac{\partial F_z}{\partial u}u + \frac{\partial F_z}{\partial \alpha}\Delta\alpha + \frac{\partial F_z}{\partial \dot{\alpha}}\Delta\dot{\alpha} + \frac{\partial F_z}{\partial q}\Delta q + \frac{\partial F_z}{\partial \theta}\Delta\theta + \cdots \\
\Delta M_y &= \frac{\partial M_y}{\partial u}u + \frac{\partial M_y}{\partial \alpha}\Delta\alpha + \frac{\partial M_y}{\partial \dot{\alpha}}\Delta\dot{\alpha} + \frac{\partial M_y}{\partial q}\Delta q + \frac{\partial M_y}{\partial \theta}\Delta\theta + \cdots
\end{aligned} \tag{4.10}$$

Note that we have only incorporated the stability derivatives within this expansion, but control derivatives are normally also included [138, 139]. In this work, we selected not to treat the elbow, wrist, and shoulder angles or the tail as control inputs, but rather to investigate each possible configuration independently as a rigid-body flyer. This simplified approach was intended solely to provide an initial understanding of the dynamic stability of each morphological configuration. Future work is warranted to investigate the role of the control derivatives associated with each degree of freedom and to capture the dynamics of morphing between configurations.

To investigate the flight dynamics, each of the aerodynamic stability derivatives in equation 4.10 must be estimated. This can be simplified by investigating the free body diagram of the configuration in question under a perturbed condition. From this perturbed aerodynamic state we can next estimate the key derivatives.

Forward speed, u

If we assume a perturbation in the forward speed from the equilibrium (Eqn. 4.5) [138], we obtain:

$$\begin{aligned} F_x &= \Delta F_x = -\Delta D \\ F_z &= \Delta F_z = -\Delta L \end{aligned} \tag{4.11}$$

This equation allows us to calculate the effect of a change in the flight speed on the initial equations [138]:

$$\begin{aligned} \frac{\Delta F_x}{\Delta u} \approx \frac{\partial F_x}{\partial u} &= \frac{1}{2}\rho U_0^2 S_{max}(-2C_{D_0} - \frac{\partial C_D}{\partial u}) \\ \frac{\Delta F_z}{\Delta u} \approx \frac{\partial F_z}{\partial u} &= \frac{1}{2}\rho U_0^2 S_{max}(-2C_{L_0} - \frac{\partial C_L}{\partial u}) \\ \frac{\Delta M_y}{\Delta u} \approx \frac{\partial M_y}{\partial u} &= \frac{1}{2}\rho U_0^2 S_{max} c_{max} \frac{\partial C_M}{\partial u} \end{aligned}$$

During our experimental analysis in Chapter 2 we tested the gull-inspired wings at two different biologically relevant Reynolds numbers (approximately 1.5×10^5 and 2.2×10^5) and found a statistically insignificant effect of velocity on the coefficient of lift, drag and pitching moment for angles of attack used within the analysis ($-10^\circ < \alpha < 5^\circ$) [141]. This outcome was expected since the testing was limited to speeds that birds are known to fly at, which are well within the subsonic regime [122]. These simplifications led to the final form of the speed derivatives:

$$\begin{aligned} \frac{\partial F_x}{\partial u} &\approx \frac{1}{2}\rho U_0^2 S_{max}(-2C_{D_0}) \\ \frac{\partial F_z}{\partial u} &\approx \frac{1}{2}\rho U_0^2 S_{max}(-2C_{L_0}) \\ \frac{\partial M_y}{\partial u} &\approx 0 \end{aligned} \tag{4.12}$$

Angle of attack, α

Next, we assumed a perturbation in the angle of attack and a small angle assumption to obtain the perturbed equations as:

$$\begin{aligned} \Delta F_x &\approx L_0 \Delta\alpha - \Delta D \\ \Delta F_z &\approx -\Delta L - D_0 \Delta\alpha \end{aligned} \tag{4.13}$$

From here, the angle of attack derivatives can be estimated as:

$$\begin{aligned} \frac{\partial F_x}{\partial \alpha} &\approx \frac{1}{2}\rho U_0^2 S_{max}(C_{L_0} - \frac{\partial C_D}{\partial \alpha}) \\ \frac{\partial F_z}{\partial \alpha} &\approx \frac{1}{2}\rho U_0^2 S_{max}(-\frac{\partial C_L}{\partial \alpha} - C_{D_0}) \\ \frac{\partial M_y}{\partial \alpha} &= \frac{1}{2}\rho U_0^2 S_{max} c_{max} \frac{\partial C_M}{\partial \alpha} \end{aligned} \tag{4.14}$$

To estimate the derivatives with the angle of attack we took the derivative of our linear model fits for the coefficient of lift (Eqn. 4.6), coefficient of pitching moment (Eqn. 4.7) and coefficient of drag (Eqn. 4.8). It is possible that these angle of attack derivatives of the coefficient of lift have a lower magnitude than expected due to error between the numerical and experimental results [141]. By limiting our analysis to lower angles of attack, we expect this error to be reduced but additional studies are required to improve the angle of attack relationship with lift. Note that for the pitching moment derivative, we assumed that:

$$\frac{\partial C_M}{\partial \alpha} = \frac{\partial C_M}{\partial C_L} \times \frac{\partial C_L}{\partial \alpha} \tag{4.15}$$

This approximation is valid at low angles of attack within the linear region of the pitching moment and lift relationship.

Rate of change of the angle of attack, $\dot{\alpha}$

Because our gull is modeled with a furled tail, we neglected all of the aerodynamic derivatives related to the rate of change of the angle of attack ($\dot{\alpha}$). This is equivalent to assuming that the flow remains attached over the wings and is an acceptable assumption for a gliding

configuration at small angles of attack. Note that for the force equations, this is commonly done in large scale aircraft due to the small contribution of this term even with a tail [139].

Pitch rate, q

Following Pamadi's derivation [138], it can be shown that:

$$\begin{aligned}
\frac{\partial F_x}{\partial q} &\approx -\frac{1}{2}\rho U_0^2 S_{max}\frac{\partial C_D}{\partial q} \\
\frac{\partial F_z}{\partial q} &\approx -\frac{1}{2}\rho U_0^2 S_{max}\frac{\partial C_L}{\partial q} \\
\frac{\partial M_y}{\partial q} &\approx \frac{1}{2}\rho U_0^2 S_{max} c_{max}\frac{\partial C_M}{\partial q}
\end{aligned} \tag{4.16}$$

We directly calculated $\frac{\partial C_L}{\partial q}$ and $\frac{\partial C_M}{\partial q}$ from numerical results for the same nine wings configuration that were tested in the wind tunnel. This was done by running MachUpX for each wing held at each shoulder sweep and dihedral angle configuration while varying q from -0.5 to 0.5 rad/s. Given our problem formulation in MachUpX, while we estimated the stability derivatives q was defined to be about the shoulder joint. Therefore in this work, we implicitly assume that the change in the pitching moment coefficient about the center of gravity due to a pitch rate at the shoulder joint is approximately equal to that due to a pitch rate about the center of gravity. Similarly, we implicitly assume that the change in the lift coefficient due to a pitch rate at the shoulder joint is approximately equal to that due to a pitch rate about the center of gravity. With these outputs we then fit a linear model that predicted the pitch rate derivatives for each joint angles as:

$$\frac{\partial C_L}{\partial q} = E_0 + E_1 e + E_2 w + E_3 \Lambda + E_4 e w + E_5 e \Lambda + E_6 w \Lambda + E_7 \Gamma \tag{4.17}$$

$$\frac{\partial C_M}{\partial q} = G_0 + G_1 e + G_2 w + G_3 \Lambda + G_4 \Gamma + G_5 \frac{\partial C_L}{\partial q} \tag{4.18}$$

The linear models had adjusted R^2 values of 0.93 and 0.80, respectively. We assumed that the effect of q on the drag ($\frac{\partial C_D}{\partial q}$) was negligible following traditional aircraft studies [138].

Flight path angle, θ

Finally, we assumed that the pitch angle had been perturbed. Using trigonometric identities and a small angle approximation on the pitch angle the following equations are obtained:

$$F_x = \Delta F_x = -mg\cos(\gamma_0)\Delta\gamma$$
$$F_z = \Delta F_z = -mg\sin(\gamma_0)\Delta\gamma$$

Further, because $\gamma = \theta - \alpha$ and the change in the pitch angle (θ) is independent from the angle of attack (α), $\Delta\gamma = \Delta\theta$. This leads to:

$$\begin{aligned} \frac{\partial F_x}{\partial \theta} &= -mg\cos(\gamma_0) \\ \frac{\partial F_z}{\partial \theta} &= -mg\sin(\gamma_0) \\ \frac{\partial M_y}{\partial \theta} &= 0 \end{aligned} \tag{4.19}$$

4.3.6 Complete formulation

Finally, all of the above stability derivatives can be integrated into equation 4.10 and equation 4.3. We can write the final small perturbation state-space representation of each bird configuration as:

$$\dot{\mathbf{X}} = A\mathbf{X}$$

$$\mathbf{X} = \begin{bmatrix} u \\ \Delta\alpha \\ \Delta q \\ \Delta\theta \end{bmatrix}$$

$$A = \begin{bmatrix} -2\tilde{m}C_D & \tilde{m}(C_L - \frac{\partial C_D}{\partial \alpha}) & 0 & -\frac{g}{U_0}\cos(\gamma_0) \\ -2\tilde{m}C_L & \tilde{m}(-C_D - \frac{\partial C_L}{\partial \alpha}) & 1 - \tilde{m}\frac{\partial C_L}{\partial q} & -\frac{g}{U_0}\sin(\gamma_0) \\ 0 & \tilde{I_{yy}}\frac{\partial C_M}{\partial \alpha} & \tilde{I_{yy}}\frac{\partial C_M}{\partial q} & 0 \\ 0 & 0 & 1 & 0 \end{bmatrix} \tag{4.20}$$

Where:

$$\tilde{m} = \frac{\rho U_0 S}{2m} \qquad\qquad \tilde{I_{yy}} = \frac{\rho U_0^2 S c}{2I_{yy}}$$

These equations model the longitudinal dynamics of the fixed-wing gull as a fourth-order system under the simplifications outlined above.

4.3.7 Free response characteristics

To determine the longitudinal dynamic stability characteristics, we began by solving the eigenvalue problem ($\lambda I - A = 0$) associated with the free response of the system, where I is the identity matrix and λ represents the eigenvalues of the system. This returns a characteristic equation that can be solved to extract the associated roots of the system. In aeronautical studies, it is possible to make additional assumptions on the system to return the short period and phugoid mode approximations, but we instead solved the complete fourth order system for improved accuracy [138]. With these outputs, we calculated the damping ratio and frequency of the short period and phugoid mode of each configuration [138] from equation 1.2.

4.3.8 Gust response

Next, we used the Python Control Systems Library [222] to solve for the time response of the gull for two simplified gusts.

Transverse gust

First, to model a simplified transverse gust, we solved the free response of the system given an initial angle of attack of 2°. This is mathematically equivalent to an impulse in the angle of attack. Due to the rigid body assumption, we did not model the joints as independent controls and thus the input vector (**U**) is zeros for this case. To extract the time response, we solved the following system for each trimmed wing configuration:

$$\dot{\mathbf{X}} = A\mathbf{X}$$

With the following initial condition:

$$\mathbf{X}_{t=0} = \begin{bmatrix} 0 \\ 2\frac{\pi}{180} \\ 0 \\ 0 \end{bmatrix}$$

Streamwise gust

Second, to model a streamwise gust, we solved for the forced response of a discrete gust model as implemented within MIL-F-8785C, which uses a 1-cosine velocity profile [214]. We assumed that the gust velocity was in the positive *x* direction such that:

$$u_a = u - u_g \tag{4.21}$$

Note that the gust velocity will be subtracted from the body velocity as the governing equations were developed with motion relative to the atmosphere [139]. This results in the following state space system:

$$\dot{\mathbf{X}} = A\mathbf{X} + B\mathbf{U}$$

Where:

$$B = \begin{bmatrix} 2\tilde{m}C_D \\ 2\tilde{m}C_L \\ 0 \\ 0 \end{bmatrix}$$

$$\mathbf{U} = \begin{bmatrix} u_f(t) \end{bmatrix}$$

The initial condition was set to zero for all inputs. Finally, we solved the system by discretizing in time (following methods outlined in the Python Control Systems Library [222]), so that the

gust was modeled as:

$$u_f(t) = \begin{cases} 0 & t = 0 \\ \frac{u_g}{2}(1 - \cos(\frac{\pi t}{t_m})) & 0 < t \leq t_m \\ u_g & t > t_m \end{cases}$$

Where u_g is the gust amplitude, which was set as 2% of the trim speed (U_0) and t_m was 5 seconds. This model is similar to that introduced by MIL-F-8785C [214], although we defined the gust relative to time rather than distance traveled.

4.4 Results

4.4.1 Trim states

With the aerodynamic coefficients for each wing configuration, we solved for the trim angle of attack (α_0), trim speed (U_0), and trim glide angle (γ_0) (Fig. 4.3a, see Section 4.3.3). For the configurations capable of trimmed flight (n = 1457), we found that the trim speed ranged from 11.8 to 29.8 m/s and the shallowest trim glide angle was -12.2°. In-flight measurements of gulls gliding past an urban environment by Shepard et. al [25] showed an airspeed range from 8.1 to 19.9 m/s, which includes approximately half of our configurations (n = 768). This previous study investigated gulls in transient flight and did not include behaviors with high glide angles such as those used in landing flight. As such, we expect that gulls have the capability to trim at the higher speeds as predicted by our model. Note that due to our imposed limits on the angle of attack and dihedral angle, it is likely and probable that gulls can also trim at lower speeds and shallower glide angles. Our identified trim states permit an initial evaluation of dynamic stability in gull gliding flight.

To determine how the three different wing joints affect the trim state, we fit linear models where the trim speed and glide angle were the dependent variables and the elbow, wrist, and sweep angles were independent variables. This analysis revealed strong interactive effects between the joint angles for both the trim speed and glide angle. Folding the wrist, increased the trim glide speed for over 80% of tested configurations and folding the elbow, increased the trim glide speed for 60% of tested configurations. Because there is evidence that many

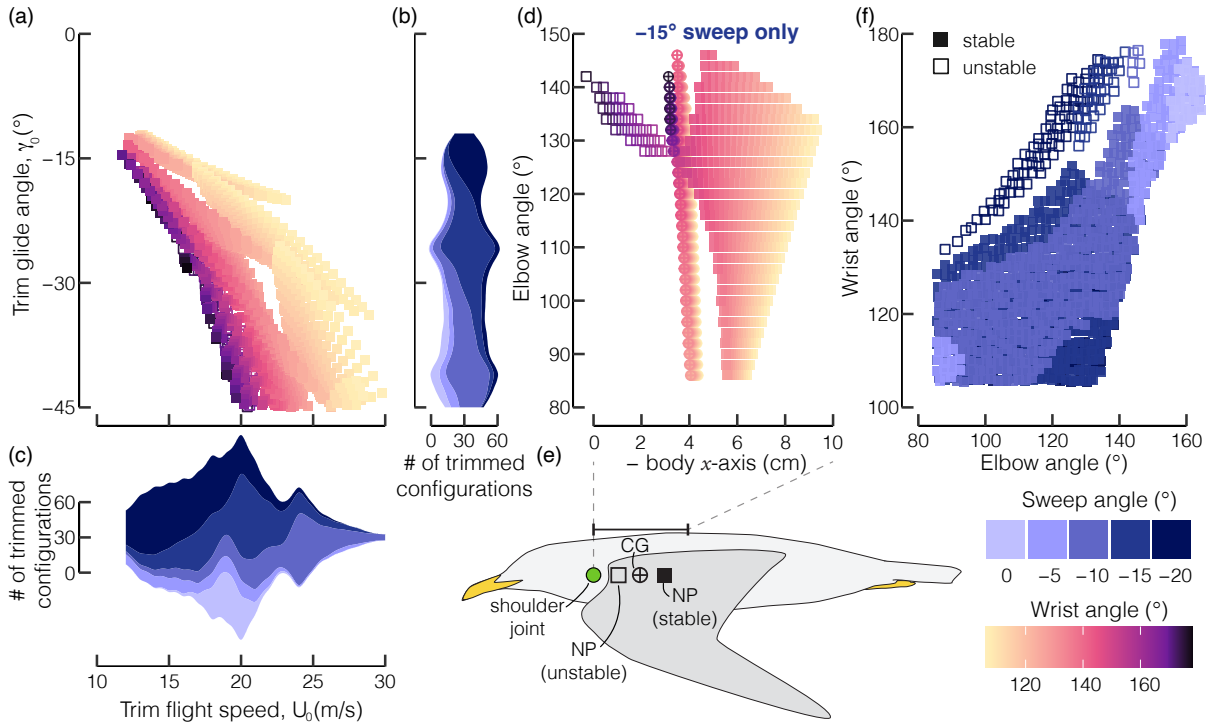

Figure 4.3: **Wing morphing allows gulls to switch between statically stable and unstable configurations.** (a) The gull can fold its wrist to trim as speeds increase. The configurations capable of trimmed flight (n = 1457) include multiple forward sweep angles (b and c). (d) Gull wing morphing allows a substantial shift in the static margin largely due to neutral point control as the motion of the center of gravity remains relatively small. (e) The gliding gull is unstable if the neutral point is in front of the center of gravity and stable if it is behind. (f) Adjusting the forward sweep angle ensures that the majority of elbow and wrist configurations at 20° dihedral angle can trim, but most configurations with high wrist angles become statically unstable (hollow squares).

bird species, including gulls, fold their wing joints as wind speeds increase [39, 52, 82, 85, 92, 100, 124, 128, 223], our results suggest that this wing morphing behavior allows gliding birds to adjust their trim condition to adapt to different flight conditions. In addition, we found that reducing the forward sweep at the shoulder joint caused the trim glide speed to increase (and the glide angle to decrease) for each tested configuration as expected from traditional aeronautical results [129]. Yet, there is little documented evidence of birds sweeping their wings backwards at the shoulder joint in response to increased wind speeds. Therefore, it is possible that to trim, birds preferentially fold their wings rather than just changing the shoulder joint sweep angle. One benefit to folding the elbow and wrist over sweeping the entire wing would be that folding the wing both reduces the total wing lifting area and moves the wings closer to the body. These

two effects would reduce the wing bending moment, whereas adjusting the shoulder sweep angle would not change the wing area and only marginally move the wings closer to the body. A directed study is required to determine if and how birds balance trade-offs between structural constraints and aerodynamic loading in trimmed flight.

4.4.2 Static stability about the trim state

With the known trim state for each configuration, we next investigated the static stability of each configuration. We quantified static stability with the static margin, a measure of the distance between the center of gravity and the neutral point. The neutral point is the location where the distributed forces and moments can be modelled as point loads. It differs from the center of pressure because the pitching moment about the neutral point is independent of the angle of attack. If the neutral point is behind the center of gravity, the configuration has a positive static margin and is statically stable (Fig. 4.3e) [141].

We found that the majority of trimmed elbow, wrist, and shoulder combinations for the gull were statically stable (solid squares, n = 1331, Fig. 4.3f), but there was a set of configurations with extended wrist angles that were unstable (hollow squares, n = 126, Fig. 4.3f). We found that the progression towards instability for the gull wings was largely driven by a shift in the neutral point rather than the center of gravity, as is expected since wing morphing has only a marginal effect on shifting the center of gravity (Fig. 4.3d for a constant 15° forward sweep angle) [142]. This result agrees with Durston's finding that raptors gliding towards their trainers with fully extended wing configurations were statically unstable [219]. However, our results expand on this understanding to reveal that a gull can fold its wrist to achieve a stabilized configuration, allowing a shift between stable and unstable flight conditions.

This capacity to shift stability with wing morphing agrees with a previous finding that most species can shift between stable and unstable flight [142]. However, that previous study was limited to 0° shoulder sweep and dihedral angles, which yields only statically stable configurations for the gull. Here, we expanded on these results to show that including the shoulder joint further enhances birds' ability to transition between statically stable and unstable flight. It is important to highlight that there is limited data on the true shoulder angles used in bird flight. However, gulls are often observed flying with swept forwards wings held at a positive dihedral

angle [224], therefore this stability shift is likely used by live gliding gulls.

4.4.3 Dynamic stability about the trim state

Static stability provides a necessary, but insufficient condition of full stability. To determine if a gull is completely stable, we next calculated the dynamic characteristics by solving for the eigenvalues of the rigid gull modelled as a fourth-order system. We found that all the statically stable configurations had eigenvalues with negative real values for both vibrational modes (solid points, n = 1331, Fig. 4.4a and b) leading the gull to be dynamically, and thus completely, stable in the longitudinal axis. Only statically unstable configurations had dynamically unstable responses and exhibited a non-oscillatory divergent response, which was characterized by eigenvalues with only real parts, similar to Durston's results [219]. This indicates that the gull was only ever completely stable or unstable and there were no configurations that exhibited static stability and dynamic instability. Of note, we found that the phugoid mode remained stable even for the statically unstable configurations (Fig. 4.4b) and thus the instability was entirely due to the unstable short period response.

With the complex and real components of the eigenvalues, we calculated the damping ratio (ζ) and natural frequency (ω) associated with the two vibrational modes for all the stable

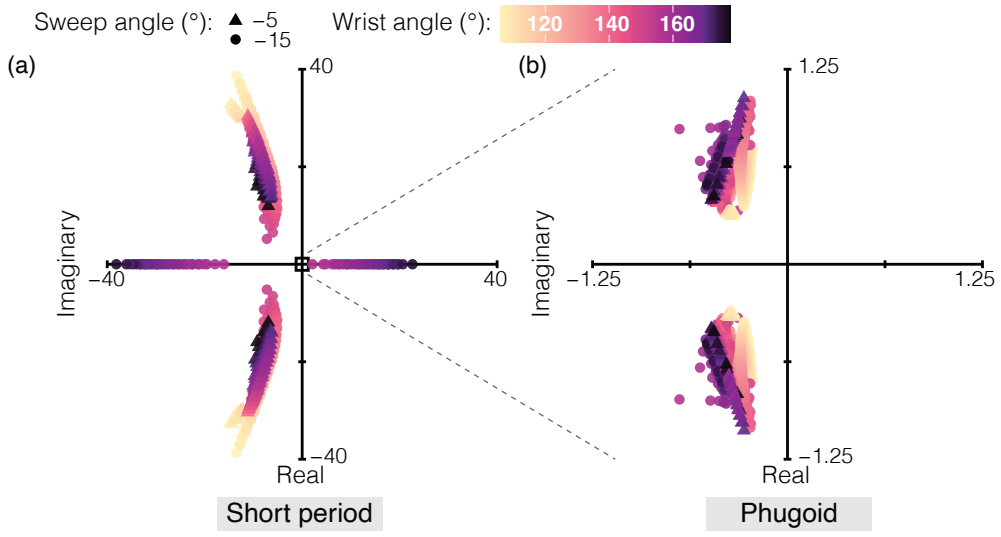

Figure 4.4: **Root locus plot of the open-loop system.** The poles of the fourth order system are displayed for a forward sweep angle of 5° (triangles) and 15° (circles) for the short period (a) and phugoid mode (b).

configurations. First, one mode had a high frequency, highly damped response (Fig. 4.5a and c) that was independent of the speed (demonstrated by the low magnitude of the teal dots in Fig. 4.6a). This response is characteristic of the short period mode (Fig. 4.1a). The short period frequency ranged from 8.9 to 41.0 rad/s, which is approximately half to more than double the frequency of a similar sized UAV (Fig. 4.5a) [217]. Previous studies have shown that small UAVs will have higher short period frequencies than large aircraft due to scaling alone [217, 218]. The gull's variable frequency response is because wing morphing allows a substantial shift in the static margin, and thus the static stability, compared to values used in traditional UAV designs [138, 139]. To this end, wing morphing has a strong effect on the short period characteristics for gulls. Furthermore, we found significant interactive effects between the elbow, wrist, and sweep angles (visualized in Fig. 4.5a and c). Despite these interactive effects, general trends in the short period characteristics are apparent within our investigated joint ranges. For example, wrist extension decreased the short period natural frequency (Fig. 4.5a) and increased the damping ratio (Fig. 4.5c), when the elbow angle was above 90°.

Next, the second identified mode had a substantially lower frequency response (Fig. 4.5b) that was independent of the angle of attack (demonstrated by the low magnitude of the light blue dots in Fig. 4.6b). This response is characteristic of the phugoid mode (Fig. 4.1b). The phugoid mode had a similar or slightly lower frequency than a similar sized UAV ranging from 0.45 to 1.10 rad/s (Fig. 4.5b). However, we found that the phugoid mode was heavily damped, with a damping ratio on the same order of magnitude as the short period mode (Fig. 4.5d). This is unlike most comparable UAVs or large scale aircraft [138, 217, 218], although a flight test on a smaller morphing gull-wing UAV found a similar heavily damped phugoid mode [31]. We expect that the high damping is because we investigated gliding flight rather than steady, level cruise and because our configurations were limited to angles of attack below 5°, which excludes the most aerodynamically efficiency results for these wing configurations. Per Pamadi's phugoid approximation, these combined approximations will decrease the phugoid frequency and increase the damping ratio [138]. Therefore, it remains possible that at more efficient trim conditions a gull configuration could be statically stable but dynamically unstable due to reduced phugoid damping. Like the short period mode, we found significant interactive effects between the elbow, wrist, and sweep angles (visualized in Fig. 4.5b and d). Unlike the rela-

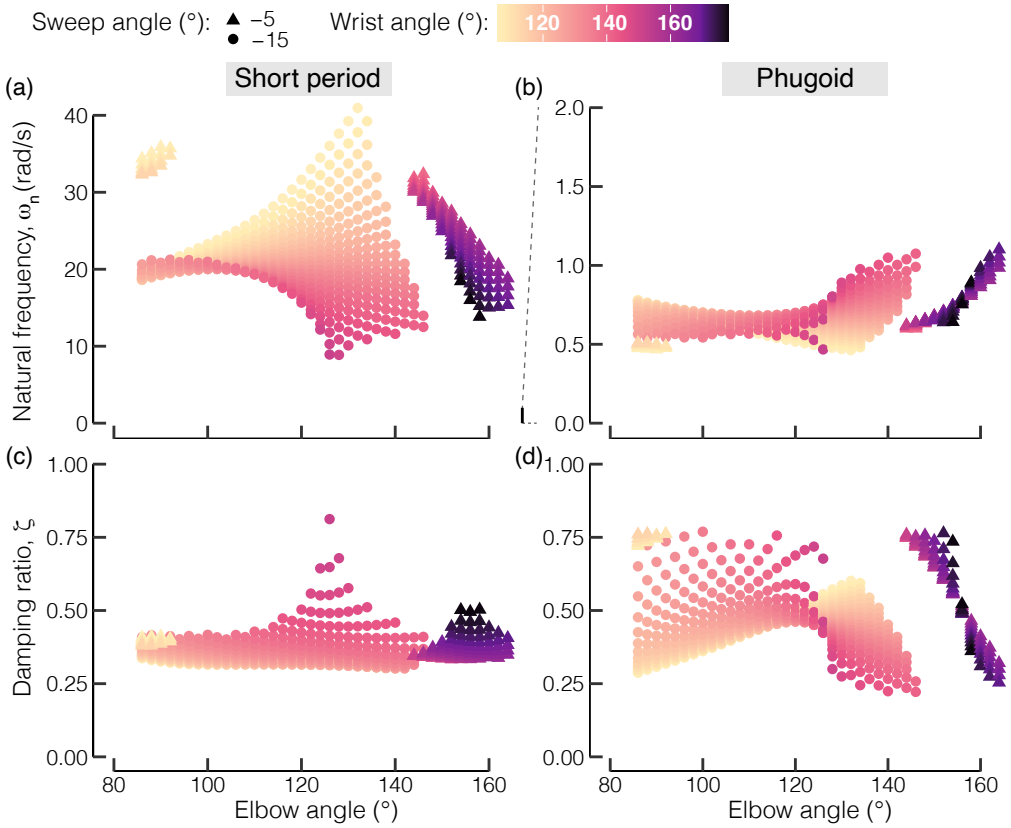

Figure 4.5: **The short period and phugoid mode characteristics are significantly affected by the wing positioning.** Within the *in vivo* range (above 90° elbow angle) wrist extension tends to decrease the short period (a) natural frequency and increase the (b) damping ratio. The effect of wrist extension on the phugoid (c) natural frequency and (d) damping ratio depends on the elbow angle.

tively consistent wing morphing trends for the short period, the effect of wrist extension on the phugoid frequency (Fig. 4.5b) and damping (Fig. 4.5d) reverses signs within our investigated ranges. For example, the damping ratio tends to increase with wrist extension at low elbow angles but tends to decrease with wrist extension at high elbow angles.

4.4.4 Flying qualities

To better understand the dynamic response characteristics, we compared the estimated flying qualities of the gull to known aircraft specifications. We evaluated the flying qualities as established by the U.S. Department of Defense's MIL-F-8785C specification [214]. This specification defines three levels of flying qualities: Level 1 flying qualities are clearly adequate for

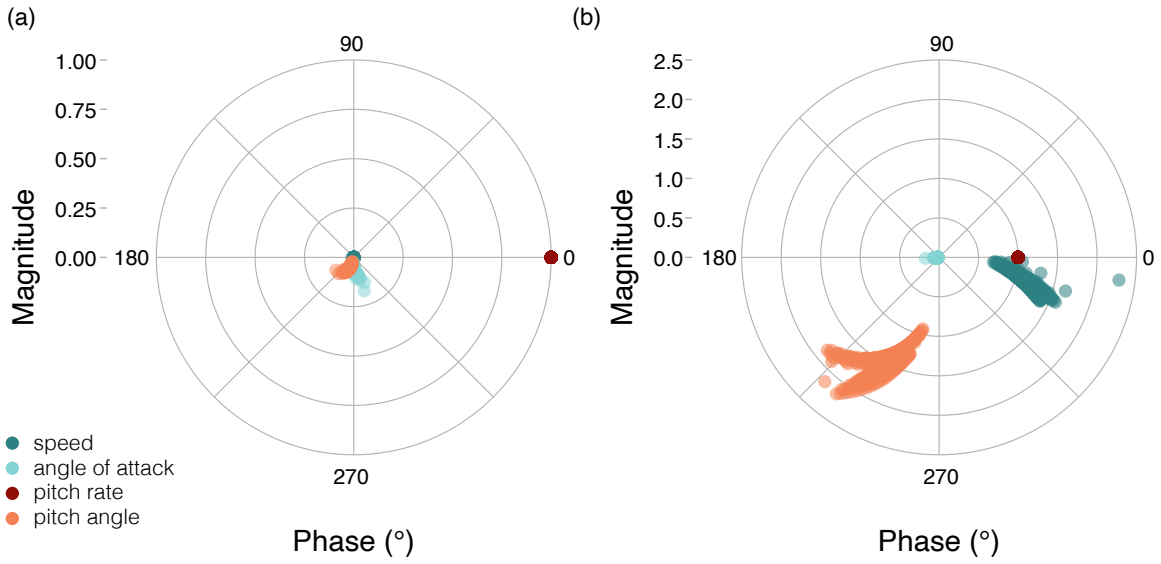

Figure 4.6: **Short period and phugoid modes were identified from the magnitude of the eigenvectors.** All magnitudes and phases were normalized to the pitch rate (maroon dot) to facilitate comparison. (a) The short period was characterized by the high magnitude response in the pitch rate (maroon dots) and a small magnitude response in the speed (dark teal dots). (b) The phugoid mode was characterized by a high magnitude response in the speed (dark teal dots) and pitch angle (orange dots) with a small magnitude response in the angle of attack (pale blue dots).

the given flight phase; Level 2 necessitates a higher pilot workload and/or degradation of mission effectiveness; and Level 3 results in an excessive workload or inadequate mission effectiveness. We considered only qualities associated with flight phases that include non-terminal flight maneuvers such as a gliding descent (Category B per MIL-F-8785C).

MIL-F-8785C defines desirable short period characteristics by the damping ratio (ζ) and a short period frequency metric, which is the ratio of the natural frequency squared (ω_{sp}^2) to the load factor per angle of attack (n_α) (y-axis, Fig. 4.7). Considering the damping ratio limits, we found that most configurations (n = 1232) satisfied the Level 1 requirements, however some configurations (n = 99) with a 20° forward sweep angle only satisfied the Level 2 requirements (Fig. 4.7, M, solid vertical lines). Considering the frequency metric requirements, we found that only seven configurations satisfied Level 2 requirements (Fig. 4.7, M, solid horizontal lines). Although interactive effects were again significant, we found that sweeping the wing forwards, extending the wrist, or folding the elbow angle tended to reduce the short period frequency metric, thus improving the flight quality (p-values < 0.001, $R^2 = 0.9083$, Fig. 4.7).

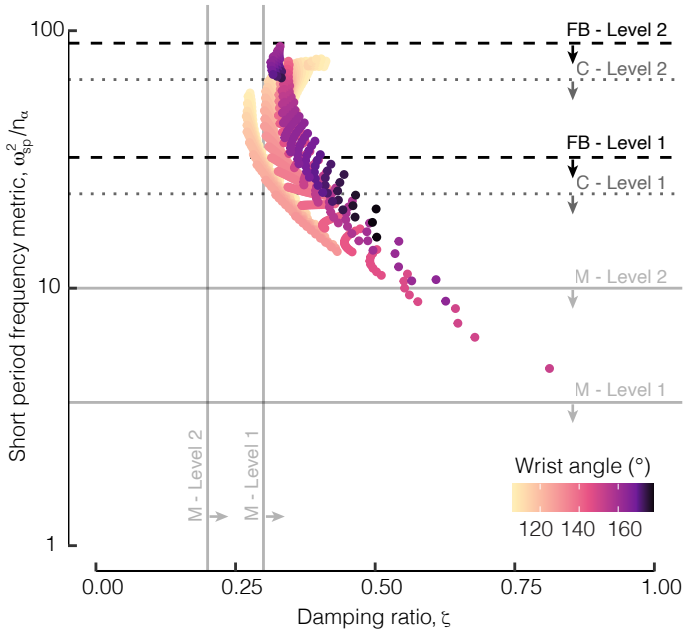

Figure 4.7: **Most gull configurations satisfied Level 2 short period requirements for human pilots per adjusted UAV guidelines.** For the damping ratio, all configurations satisfy at least Level 2 MIL-F-8785C (shortened to M, solid vertical lines). For the frequency metric, no configurations satisfied the Level 1 MIL-F-8785C requirements (M, solid horizontal lines). Adjusting for two previously published UAV metrics revealed that 185 configurations satisfied Capello et. al's Level 1 upper limits (C, grey dotted lines) and 457 configurations satisfied Foster and Bowman's Level 1 upper limits (FB, black dashed lines). All configurations satisfied Foster and Bowman's Level 2 upper limits.

All stable configurations exhibited at least Level 3 qualities in the damping ratio and frequency limits, but this is indicative of a flyer that would be difficult to control [214].

However, studies on small UAVs have shown that the MIL-F-8785C short period frequency metric guidelines do not accurately capture the flying qualities of small UAVs [215–218]. As a result, new scaling parameters have been proposed. Incorporating Foster and Bowman's [218] scaling we found that all of our stable, trimmed gull configurations (n = 1331) would have at least Level 2 flying qualities and 457 configurations would have Level 1 flying qualities (Fig. 4.7, FB, dashed lines). Incorporating Capello et. al's scaling [217], we found that 1167 configurations would have Level 2 flying qualities and 185 would have Level 1 flying qualities (Fig. 4.7, C, dotted lines). Note that we used a Cessna 172 as the comparable large scale aircraft to calculate the scaling constant [217, 225]. Thus, by accounting for known differences between large scale aircraft and small UAVs, our results suggest that a gull-like UAV design

with wings swept forward less than 20° would be flyable albeit with a higher pilot workload for many configurations.

Unlike the short period mode, MIL-F-8785C only provides a minimum criterion on the phugoid damping ratio and UAV-focused studies tend to agree with the effectiveness of this parameter [217, 218]. Our results show that the gull was substantially above the Level 1 minimum damping ratio of 0.04 (Fig. 4.5c) and had nearly an order of magnitude higher damping ratio than comparable UAVs. As discussed previously, this is due both to our gliding analysis and the lower aerodynamic efficiency in the tested configurations. Future work is required to determine if these values exhibited by gliding gulls are too heavily damped for effective implementation in a gliding UAV. A higher damped phugoid mode may be beneficial as this mode is notorious for pilot-induced oscillations, but the high damping also suggests that there is a slow response to control inputs for the flight speed and pitch angle. This sluggish response to elevator inputs was observed for a small gull-wing morphing UAV [31].

These differences in the phugoid modes between gulls and UAVs are intriguing because they may play a role in avian gust response, which tends to outperform comparable fixed-wing UAVs. Small perturbations in the forward velocity of a trimmed gliding gull would be quickly damped out according to our model. However, the gull would need to use larger control inputs to maneuver away from the equilibrium condition. These results reveal a reason that gulls may elect to switch from a stable to an unstable configuration. Gulls could use a stable configuration to reject undesired perturbations from their local environment while in transit or foraging for food. Then, gulls could extend their wrists to morph into an unstable configuration to gain a more sensitive reaction to control inputs, which would support rapid maneuvering.

4.4.5 Simplified gust response

Because the heavily damped phugoid mode pointed to possible gust-related benefits, we explored the time response of the gull to transverse and streamwise gusts. Note that a bird's gust response affects their foraging and landing capabilities [226–228]. Intriguingly, a study of live gulls in a wind tunnel found that increased turbulence intensity (a measure of variation in the freestream velocity) had no effect to the overall metabolism of the bird and thus no effect on their energetic requirements [229]. Since we found that both the phugoid and short period

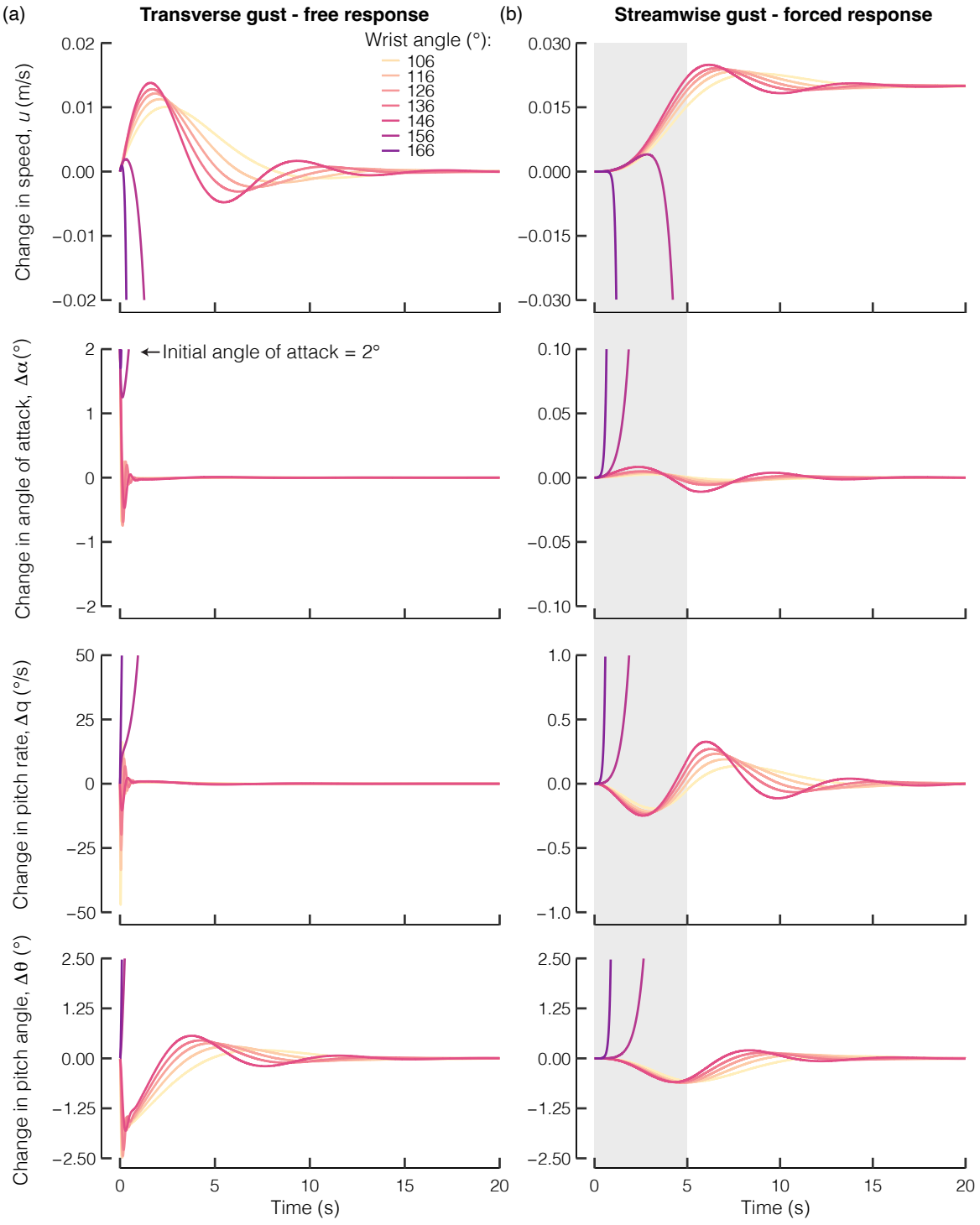

Figure 4.8: **Gull wrist gains allows substantial control over gust response.** (a) A simplified transverse gust modeled as an initial offset of 2° angle of attack. (b) A discrete 1-cosine streamwise gust modeled as an increase of 2% of the initial trim speed (U_0) over five seconds (gray box). Only configurations with an elbow angle of 130° and a forwards sweep angle of 15° are shown.

mode are heavily damped, it is possible that a gliding gull in a stabilized configuration does not require active control to return quickly to an equilibrium condition, which eliminates any additional energetic costs.

To visualize the effect of small environmental fluctuations, we calculated the dynamic responses to disturbances modeled with either a 2° step change in the angle of attack or a 2% increase in the forward speed (see Section 4.3.8). We investigated configurations with a fixed elbow angle (130°) and fixed shoulder sweep angle (15°) but a variable wrist angle (Fig. 4.8). This range allowed us to explore both stable and unstable configurations across a broad range of wrist angles. Each wing configuration was at a different trim state. The wrist angle of 156° had a trim glide angle (γ_0) of 61° and was excluded from the previous analyses as it is steeper than the imposed limit of 45° (see Section 4.3.3). We included it here for completeness.

The time responses of these configurations captured the quickly diverging dynamics associated with higher wrist angles and showed that small perturbations in the angle of attack (Fig. 4.8a) or speed (Fig. 4.8b) would be quickly damped out for lower wrist angles. For the stable configurations with lower wrist angles, the time to half the amplitude varied between 2.22 to 2.52 seconds for the phugoid mode and 0.05 to 0.12 seconds for the short period mode. For the unstable configurations with higher wrist angles, time to double the amplitude varied from 0.80 to 1.69 seconds for the phugoid mode and 0.03 to 0.04 seconds for the short period mode. In all, these results show that gulls gain significant control over their dynamic characteristics through solely adjusting their wrist joint. It is important to again highlight that the strong interactive effects acting between the elbow, wrist, and shoulder joints means that the effect of each morphing joint depends on the other joint positions and these evaluated configurations are only a representative sample. These interactive effects indicate that a complex control system would be required to effectively pilot a gull-like UAV.

4.5 Limitations

There were many simplifications used throughout this study. Predominately, this approach uses a quasi-steady aerodynamic analysis of a rigid gull undergoing small perturbations in symmetric flight. Additional work is required to extend this analysis to include a lateral anal-

ysis, non-linear and unsteady flight conditions, and larger scale atmospheric gusts. Further, we used a single gull specimen to focus our study, but there will be individual differences as well as species-specific differences in the dynamic characteristics of bird flight. To extend this study, further work will be necessary to improve aerodynamic prediction capabilities at higher angles of attack to allow an investigation of the most aerodynamically efficient configurations. Although the discussed flight qualities are a useful comparative tool, the MIL-F-8785C and the adjusted UAV guidelines are dictated by conversations with pilots [214, 217, 218]. These flying qualities do not necessarily translate to avian flying qualities, which are unlikely to be directly comparable to human metrics. Work is underway to investigate the neurological control mechanisms related to avian flight [136]. Connecting our results with information about the avian neurological control system will be a necessary next step to understand avian flight control methodologies.

4.6 Conclusion

Gulls regularly morph their wings in flight, which has been hypothesized to permit enhanced maneuverability and control. Our work incorporated existing studies on the aerodynamic and inertial properties of a gliding gull to provide the first detailed investigation of dynamic stability characteristics throughout wing morphing. Our results suggest that the gull could fold its wing joints or sweep its wings backwards to remain in a trimmed state as wind speeds increase. Further, we showed that most gull wing configurations have a short period mode that satisfies the minimum controllability requirements for Level 2 human-piloted aircraft as well as a heavily damped phugoid mode. We suggested that the high phugoid damping acts to reduce the gull's sensitivity to small perturbations in the localized environment. However, this reduced sensitivity suggests that the gull would have a sluggish response to control inputs needed to effectively maneuver. Thus, we hypothesized that gulls initiate sudden maneuvers by morphing into unstable configurations and shift into a stabilized configuration to reject non-desirable perturbations to their flight path.

In all, our study confirms that gulls can negotiate trade-offs in stability and maneuverability by morphing their wings between dynamically stable and unstable configurations and provides

a mechanism for how birds exhibit both stable flight and sudden, rapid maneuvers. Our results should encourage additional engineering investigations into morphing wings that may permit a substantial shift in the static margin. With this capability, we will be able to identify whether the ability to shift stability modes is a necessary condition to achieve avian-like maneuverability and if this approach can be harnessed to advance the maneuverability of future UAVs.

Chapter 5

Conclusion

I never am really satisfied that I understand anything; because, understand it well as I may, my comprehension can only be an infinitesimal fraction of all I want to understand about the many connections and relations which occur to me, how the matter in question was first thought of or arrived at...

– Ada Lovelace

5.1 Key results

UAV design has advanced tremendously in the past century. However, UAVs still struggle to adapt to variable conditions and missions, in part due to trade-offs between maneuverability and stability. Understanding how birds negotiate similar trade-offs provides a common ground that may inspire future more maneuverable and adaptable UAV designs. To date, it has been challenging to quantify avian flight characteristics in a way that simplifies the comparison between engineered aircraft and birds. This thesis aims to fill this gap and provide a foundational understanding of avian gliding flight stability throughout wing morphing. The stability focus provides the necessary first step towards a holistic model of avian flight maneuverability and adaptability. The main contributions and takeaways from this work are the outputs of each major data chapter as follows. Note that the introduction includes a version of sections from my published review papers [122, 129].

5.1.1 The elbow and wrist allow adaptive control

In Chapter 2, I performed the first experimentally validated lifting line analysis of a morphing bird wing and found that the extension trajectory followed while morphing the wing substantially affected the resultant aerodynamic characteristics [141].

In this chapter, I implemented an open source software (MachUpX) that calculated the lift and pitching moment of a gull's wing across the full range of flexion and extension of the elbow and wrist. To incorporate biologically-relevant wing shapes, I developed a code that discretized real gull wings into shape parameters that could be implemented in MachUpX. This methodology was informed by additional XFOIL studies on the airfoils selected to model the gull wing. These final numerically implemented, gull-inspired wings were then exported as half-wings that could be 3D printed and mounted in the wind tunnel at the University of Michigan. I 3D printed nine wings and performed wind tunnel experiments to measure the loads acting on the wing across a range of angles of attack. With the output data, I quantified the experimental uncertainty and implemented statistical approaches to analyze how the elbow and wrist angle affected the aerodynamic loads and stability across the complete range of motion.

My results identified that extending the wing with different combinations of elbow and wrist angles yielded substantially different effects on the loads and stability. One extension trajectory linearly decreased the static margin but kept the lift and pitching moment constant, while another linearly increased the lift and pitching moment but kept the static margin constant. These results are promising for two reasons. First, the linear response indicates that there are certain extension trajectories that could be used by two joints that would not require a control system to account for non-linear characteristics. Second, the substantially different outputs indicate that the same joints can adapt to different control requirements depending on the flight condition or mission.

However, I found that minor departures from the identified extension trajectories led to a coupled change in the stability and loads. This indicates a thorough sensitivity analysis of outputs would be necessary to successfully implement a gull-inspired joint-driven wing in a UAV. A version of this chapter has been published [141].

5.1.2 Birds have the capacity to shift stability states

In Chapter 3, I developed the first generalized method to calculate the inertial characteristics of flying birds and used a comparative analysis to investigate the static stability of 22 bird species [142].

For this work, I leveraged a classic analytical approach to model a flying bird with over 200

components. This approach can account for any wing posture and performs a quick calculation of the moment of inertia tensor and center of gravity. This software is published as an open source method on CRAN and GitHub. With measurements from 22 species of birds, obtained by my collaborators at the University of British Columbia, I calculated the center of gravity and moment of inertia associated with the complete range of motion of the elbow and wrist. With the outputs from Chapter 2, I estimated the location of the neutral point as a function of each bird's full range of elbow and wrist extension and flexion. With the center of gravity and neutral point, I then calculated the static margin of each species and developed a novel metric for the torsional pitch agility of a flying bird. Finally, I performed an evolutionary analysis to identify the time series model that best captured the modern birds' static margin traits. To validate and verify these results, I implemented multiple sensitivity analyses to account for measurement error and statistical variation.

I found that the majority of the investigated species (17 out of 22) had the capacity to shift between longitudinally stable and unstable flight within the range of motion of the elbow and wrist. Further, I found evidence of evolutionary pressures acting to maintain this capacity to shift between stable and unstable flight. This result shifts the field's general understanding of avian flight evolution as it was previously believed that birds were evolving towards being entirely unstable. This outcome instead suggests that there may be adaptive benefits for birds to maintain the capability to shift stability modes. Such a possibility should inspire future UAV designs to implement the capacity to shift between stable and unstable flight to approach avian-like maneuverability.

Although these results specifically indicate the capacity to shift, additional work is required to identify if, and when, live flying birds shift between stability modes. As discussed previously, different control algorithms are usually implemented for stable (open-loop) or unstable (closed-loop) configurations. Effectively implementing a control system in a UAV that can shift between these distinct stability characteristics will require a directed study. Further work is also required to identify how birds seamlessly adjust to these disparate flight conditions. A version of this chapter has been published [142].

5.1.3 Wing joints control the dynamic response

In Chapter 4, I performed the first analysis of the dynamic stability of a bird across its full range of elbow and wrist extension and flexion.

For this work, I merged the aerodynamic analysis methodology established in Chapter 2 with the inertial analysis methodology established in Chapter 3. With these aerodynamic and inertial inputs, I formulated the governing equations of motion for a rigid gull that undergoes small disturbances in the longitudinal axis. To determine a trim condition, I incorporated the shoulder joint in this analysis. I found that a positive dihedral and forward sweep angle at the shoulder joint increased the amount of trimmed configurations. With the known trim conditions for each configuration, I next calculated the eigenvalues associated with each wing joint configuration. I found that trimmed wings with high wrist angles were dynamically unstable with a non-oscillating divergent response. This unstable response was due to a negative static margin. For wings with lower wrist angles, I found that wings were dynamically stable and exhibited a traditional short period and phugoid mode. The associated natural frequency and damping ratio of these modes was found to significantly depend on the wing joints and the interactive effects between the joints.

My results showed that the stable wing configurations had short period characteristics that would be controllable by a human pilot. To arrive at this conclusion, I incorporated a UAV-based scaling to the traditional military flying quality specifications. This scaling accounts for size differences between UAVs and large scale aircraft. Unlike the controllable short period, the phugoid mode was heavily damped and would likely result in a sluggish response to control inputs. Therefore, I hypothesized that gull's ability to shift between stable and unstable flight would be necessary to allow for effective pitch control in gliding flight. For example, the heavily stabilized configurations with lower wrist angles could be used when it is desirable to inherently reject flight path perturbations, whereas a gull could extend its wrist to switch into an unstable configuration, which would result in more active control over its flight characteristics.

This initial evaluation of avian dynamic flight stability was limited to small disturbances, longitudinal flight, and a rigid body analysis. However, there are many more characteristics that must be incorporated to develop a holistic understanding of avian flight maneuverability.

5.2 Next steps

In this work, I quantified the effect of the avian elbow and wrist on longitudinal stability in a manner similar to traditional aircraft controls with the intention of identifying what aspects of bird flight control could inspire more maneuverable and adaptable UAVs. This thesis specifically focuses on gliding flight and assumes non-elastic, quasi-steady characteristics in a decoupled longitudinal plane. This approach lays the foundation for stability analysis in birds, but future studies will need to incorporate lateral characteristics and the coupling between longitudinal and lateral characteristics. Needless to say, there are a multitude of paths that must yet be explored to completely quantify and then evaluate avian flight stability, maneuverability, and adaptability. Further, there are many steps that must be taken to effectively incorporate a biological understanding of bird flight into future UAV designs. Here, I discuss three areas of study that are necessary components to advance towards a complete understanding of bird flight maneuverability.

5.2.1 Translating basic science to applied design

When approaching bio-inspired design, it is useful to begin with a comprehensive study of a desirable attribute demonstrated by a model system. With a thorough understanding of the system, it becomes possible to identify the model system's characteristics that are critical to effectively replicate the desired attribute in an engineered design. Here, the desired attribute for an engineered design is bird's enhanced maneuverability and adaptability. Therefore, the critical characteristic identified in this work is the ability to shift between stable and unstable flight. This critical characteristic is permitted by birds' ability to adjust their elbow and wrist angles.

Despite this advance in our understanding, implementing an avian-inspired elbow and wrist joint in a UAV design is likely not the next step towards realizing avian-like maneuverability. Replicating avian wing joints, or indeed any biological joint, is notoriously challenging. For an aircraft, this is further complicated because a wing joint would need to be properly reinforced to maintain an effective lifting surface and control authority under aerodynamic loading. In

addition, actuation of any wing joint requires sufficient control force to properly operate across a broad range of flight conditions. Therefore, next steps should look towards designs that use simplified, existing wing morphing mechanisms to shift between stable and unstable flight. By beginning with an example case, perhaps with a simple wing sweep morphing design, we can explore the feasibility and effectiveness of a more complicated bio-inspired design. In addition, we can evaluate if being able to shift stability modes in flight is required to enable avian-like maneuverability.

5.2.2 Relaxing flexibility constraints

Throughout this work, I have approached both the aerodynamic and inertial characteristics as if birds were rigid. This is certainly not the case. Bird feathers are flexible and result in different loading conditions across different flight speeds [230]. However, my approach allows for an initial understanding of the control provided by the wing joints and captures the implications of morphing the overall wing shape changes.

There is a focus in the aeronautical discipline to understand the role of flexibility in aircraft performance, stability, and control, however there is much left to understand about the role of flexibility in bird flight. In particular, it will be an important next step to quantify the role of flexibility in avian flight control. Specifically, it will be informative to identify how the control effectiveness of the wing joints changes due to passive morphing at different flight conditions. Aside from affecting control effectiveness, the passive response of the feathers may also serve as a form of gust alleviation and when coupled with active morphing may be an integral part to bird's ability to adapt to various flight conditions.

5.2.3 Incorporating flapping characteristics

To date, my work has entirely focused on gliding flight with the goal of laying a solid foundational understanding. Gliding flight is a valuable first step as it simplifies a direct comparison to fixed-wing UAVs. However, to truly advance our understanding of avian flight maneuverability, flapping flight cannot be overlooked.

Flapping flight and its associated unsteady characteristics play a significant role in avian

flight. In fact, some species of birds are not known to glide but instead use bounding flight, which involves repeatedly transitioning between flapping flight and tucking their wings against their body [100]. Such birds may provide inspiration for novel maneuverable UAV designs and we require more directed studies to better understand this method of flight. Substantial future work is necessary to advance towards a holistic model of bird flight that accurately captures the attributes of both gliding and flapping flight.

5.3 Summary

Here, I investigated how varying the avian elbow and wrist affected the longitudinal stability of a gliding bird. This analysis revealed that the elbow and the wrist range of motion alone permits a wide range of longitudinal control and stability characteristics. In particular, the ability to shift between stable and unstable flight was identified as a key characteristic that should be considered for future UAV designs. In all, investigating how birds control their gliding flight provides new inspiration to advance the design of more maneuverable and adaptable UAVs.

Appendix A

AvInertia Implementation

This chapter provides a detailed breakdown of the assumptions and procedures used within the development and implementation of AvInertia. The final outputs from AvInertia are returned in the pre-selected origin and axis system: the bird (vehicle) reference point (VRP) and "full bird" frame of reference (always right-handed axes). In our work, we selected the VRP to be the location where the neck attaches to the torso (Fig. A.1) . This is approximately the center of the spinal cord if cut at the clavicle. The x-axis points forwards along the center of the bird, z-axis points ventrally and y-axis points along the right wing. The selection of the origin and axis system is user-specific but must be consistently followed for all inputs. All measurements input into the program should be defined relative to this same origin unless otherwise noted in this document.

Multiple frames of reference are utilized throughout this program. Each individual section will detail the appropriate frame of reference utilized. The wing is modeled as a composite structure of bones, muscles, feathers and skin. When computing the final bird inertial properties it is possible to model both symmetric and asymmetric wing shapes. In this work, we focused solely on symmetric configurations.

A.0.1 High level methodology

1. Model all bird components as a simplified geometric shape.

2. Determine moment of inertia tensor (**I**) and center of gravity (CG) of each component within a frame of reference and about an origin that simplifies their formulation.

3. Transform **I** and CG to be within the full bird frame frame of reference with the VRP as

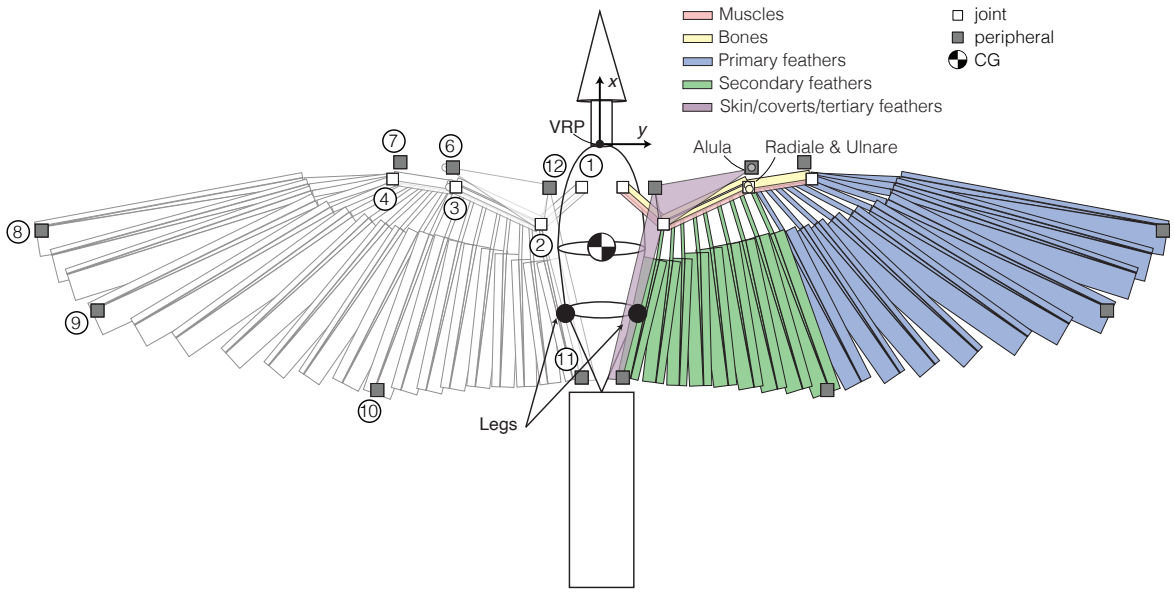

Figure A.1: **Dorsal view of entire bird modeled as a composite of simplified geometric shapes.**

the origin. This procedure is highly variable and the following sub-sections detail how each component is transformed to be in this final frame of reference.

4. Combine **I** and CG of each component appropriately.

5. Shift the origin of **I** to be about the final full CG location.

Note: Parallel axis theorem is only valid between an arbitrary point and the center of gravity, not between two arbitrary points [179]. This was accounted for within the code.

A.0.2 Required measurements

1. Full bird mass, m_{bird}

2. Single wing mass, m_{wing}

3. Position of the wing defined by ten key landmarks (Fig. A.1). Note that the identity of Pt11 varies among species; see *"birdmeasurements_readytorun.csv"* in the publicly available data repository for total feather counts. In addition, we do not include Pt5 and Pt7 as these positions were not needed within the analysis. We did not renumber to avoid

confusion.

- Pt1: Humeral head
- Pt2: Center of the elbow joint
- Pt3: Center of the wrist joint
- Pt4: Distal tip of the carpometacarpus
- Pt6: Wing leading edge ahead of the wrist joint
- Pt8: The distal tip of the final primary feather (usually P10)
- Pt9: Distal tip of the fourth-to-last primary feather (usually P7)
- Pt10: Distal tip of the first secondary feather (S1)
- Pt11: Distal tip of the final secondary feather
- Pt12: The most proximal location along the leading edge of the wing

A.0.3 Assumptions

1. **Base geometric shapes** are the greatest assumption within this code although it is commonly used for estimating the inertial characteristics of complex objects [179]. Biological specimens are variable and the accuracy of this assumption will vary between different species.

2. **Wings were aligned** so that the point on the wrist joint is in line with the shoulder along the y-axis and along the x-axis. The wing was then rotated so that the point on the feather tip at the wing root was at the same height (on the z-axis) as the shoulder. However, this is not inherent to AvInertia and any wing alignment can be input.

A.1 Wing bones

The major wing bones (humerus, radius, ulna, and carpometacarpus) are modeled as hollow cylinders with solid end caps [231, 232]. The radiale and ulnare are modeled as point masses at the wrist joint (Pt3). In addition to all physical measurements, we must know the location of the beginning of the bone and the end of the bone to extract the appropriate orientation.

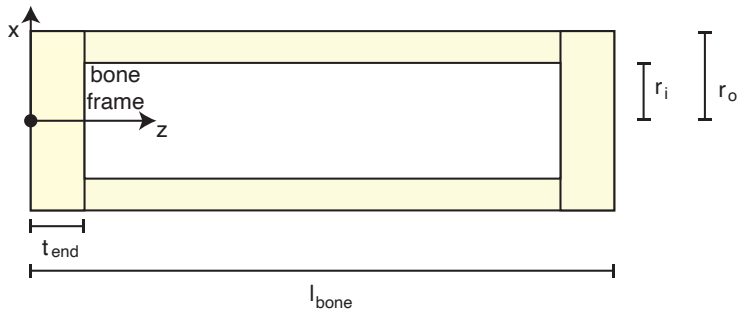

Figure A.2: **Simplified bone diagram including the referenced frames of reference.**

A.1.1 Methodology

1. Calculate the end cap thickness from:

$$\frac{m_{bone}}{\rho_{bone}} = 2(\pi r_o^2 t_{end}) + \pi({r_o}^2 - {r_i}^2)(l_{bone} - 2t_{end}) \tag{A.1}$$

2. Calculate the mass of each end cap and the hollow cylinder.

3. Determine **I** and CG of the hollow cylinder (eqn. A.5 and A.13) and two end caps (eqn. A.6 and A.13) with respect to the bone specific frame of reference and origin (Fig. A.2).

4. Transform each **I** and CG to be measured with the VRP as the origin.

5. Sum **I** of the hollow cylinder and two end caps.

6. Transform **I** and CG to be expressed within the full bird frame.

7. Radiale and ulnare estimated as point masses on Pt3 within the full bird frame.

A.1.2 Required measurements

1. Mass of each bone, m_{bone}

2. Length of each bone, l_{bone}

3. Average radius of each bone, r_o

A.1.3 Assumptions

1. **Density** (ρ_{bone}) treated as constant 2060 kg/m^3 for all major bones [233].
2. **Inner radius** (r_i) assumed to be 78% of the outer radius [234].
3. **Neglect all other wing bones.**
4. **Carpometacarpus length and mass** include digit II as well (Fig. **??**).
5. **CG is at the center of the measured bone length.** This may differ slightly from that extracted using the Optitrack markers. The start of the bone is assumed to be at the most proximal Optitrack marker.

A.2 Wing muscles

The muscles in the wing are grouped into the brachial, antebrachial and manus regions and assuming that the muscle mass is stretched the length of the major wing bones. In addition to all physical measurements, we must know the location of the beginning of the bone and the end of the bone associated with each muscle group to extract the appropriate orientation.

A.2.1 Methodology

1. Calculate the cylinder radius based on the mass and muscle density for the current group.
2. Determine **I** and CG of the cylinder (eqn. A.6 and A.13) within the bone frame of reference and origin (Fig. A.2).
3. Transform each **I** and CG to be measured with the VRP as the origin.

A.2.2 Required measurements

1. Mass of each muscle group, m_{muscle}
2. Length of each bone, l_{bone}

A.2.3 Assumptions

1. **Density** ($\rho_{muscles}$) was assumed to be 1100 kg/m^{-3} for all groups [235]. This is slightly higher than 1060 kg/m^{-3} that was calculated for muscles alone [236] because we did want to include the tendons and connective tissues in the overall calculation.

2. **Muscles are stretched** along the length. In reality, muscles will be more heavily grouped to the start and end section but for simplicity we assumed a constant muscle width along the bone length.

3. **Radius** of the muscles is determined based on the muscle group mass, estimated muscle density and the length of the bones.

A.3 Flight feathers

The flight feathers including all primaries and secondaries are modeled as a composite object (Fig. A.3). The calamus is modelled as a hollow cortex cylinder [237], the rachis as a hollow cortex exterior square pyramid and a solid medullary interior square pyramid [237, 238], and the vanes as flat rectangular plates. In addition to all physical measurements, we must provide the approximate location of the feather tip and root to extract the appropriate orientation.

A.3.1 Methodology

1. Calculate the approximate vane mass assuming vanes are composed of solid cortex cylindrical barbs with a previously determined [239, 240] barb radius (r_{barb}) and spacing (d_{barb}) per:

$$n_{barbs} = l_{vane}/(d_{barb} + 2r_{barb}), \tag{A.2}$$

$$m_{vane} = \rho_{cortex} n_{barbs} w_{vane} \pi r_{barb}^2. \tag{A.3}$$

2. Substract the proximal and distal vane masses from the total feather mass m_f to determine the total mass of the rachis and calamus (m_{rc}).

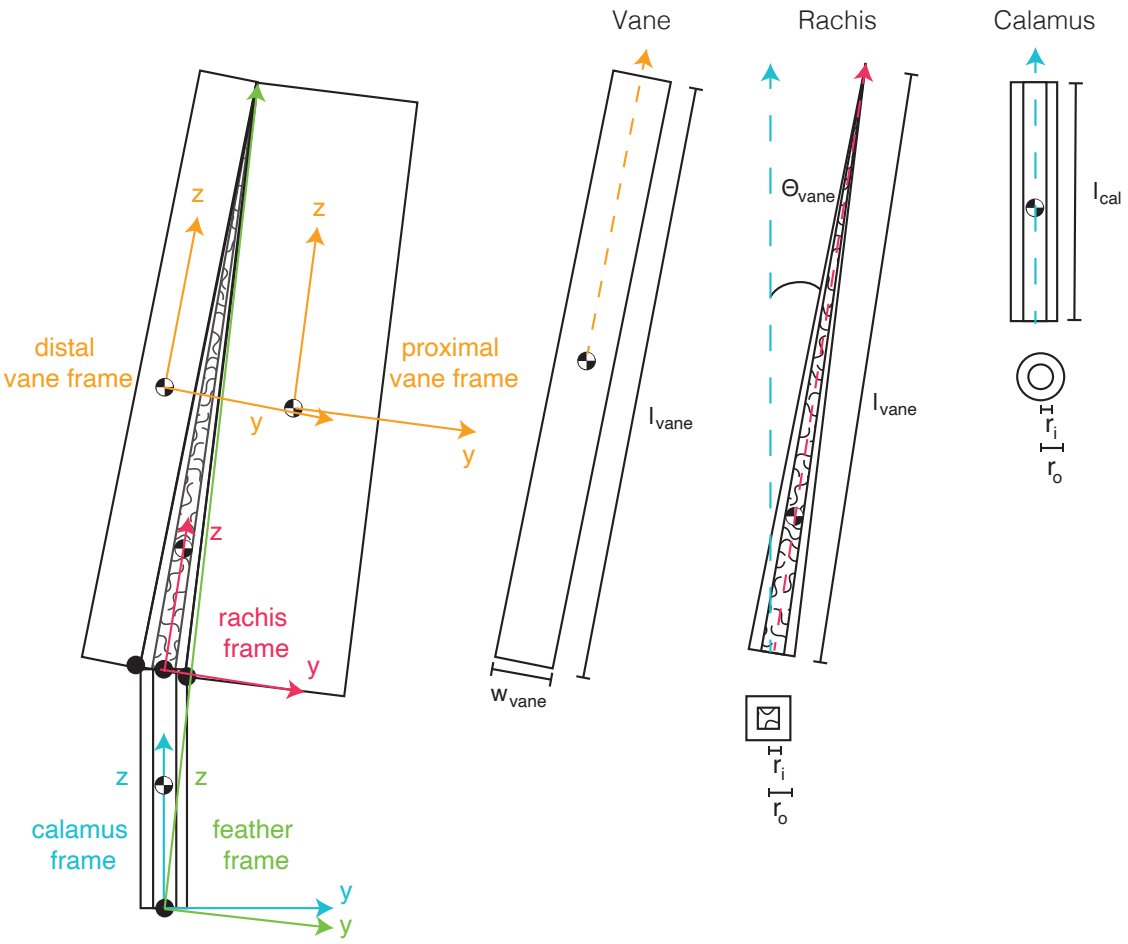

Figure A.3: **Simplified feather diagram including the referenced frames of reference.**

3. Calculate the inner radius ($r_{i_{cal}}$) of the calamus and width of the interior rachis pyramid by ensuring that m_{rc} is equal to the mass predicted by the volume and density of the calamus and rachis components:

$$m_{rc} = \rho_{cor}(\pi(r_{o_{cal}}^2 - r_{i_{cal}}^2)l_{cal} + \frac{4}{3}(r_{o_{cal}}^2 - r_{i_{cal}}^2)l_{vane}) + \rho_{med}(\frac{4}{3}r_{i_{cal}}^2 l_{vane}). \quad \text{(A.4)}$$

4. Determine **I** and CG of the calamus (eqn. A.6 and A.13) within the calamus frame assuming a hollow cylinder.

5. Determine **I** and CG of the rachis (eqn. A.10 and A.14) within the rachis frame assuming exterior cortex and interior medullary retangular pyramids.

6. Determine **I** and CG of each vane (eqn. A.11) within their respective vane frames assuming flat rectangular plates with a mass calculated in Step 1.

7. Transform each vane property into the rachis frame.

8. Combine the rachis and vane **I** and CG properties.

9. Transform rachis and vane **I** and CG to be expressed in the calamus frame, (rotate by θ_{vane}) with the origin as the start of the feather.

10. Combine **I** and CG for the rachis and vane with the calamus components.

11. Transform **I** and CG to be expressed in the feather frame. Up to this point all of this inertial data can be computed with no knowledge of the current wing positioning. For this reason, the code has two seperate functions relating to the feather inertial calculations.

12. Transform **I** and CG to be expressed in the full bird frame using information about each individual feather positioning and orientation.

13. Alula feathers estimated as a point mass on Pt6 within the full bird frame.

A.3.2 Required measurements

1. Mass of each feather, m_f
2. Length of the calamus, l_{cal}
3. Length of the vane, l_{vane}
4. Outer radius of the calamus, $r_{o_{cal}}$
5. Distance between barbs, d_{barb}
6. Radius of feather barbs, r_{barb}
7. Average width of proximal/distal vanes, w_{vane}
8. Interior angle between calamus and rachis, θ_{vane}

A.3.3 Assumptions

1. **Density** of cortex (ρ_{cor})[238, 241–244] and of medullary (ρ_{med})[242, 245] material treated as constant 1150 kg/m^3 and 80 kg/m^3, respectively.

2. **Shape of feathers** was assumed to be constant within a species. We measured the shape properties for only one specimen but, individually measured the mass of each specimen's feathers. Then we assumed isometric scaling to adjust the length and area measurements for each feather as necessary.

3. **Length of medullary** part of the rachis extends all the way to the feather tip [238].

4. **Mass of vanes** is based on previously measured barb radii and distance between barbs [239, 240].

5. **Proximal and distal vane barb** properties are treated as constant. Note that previous work did find slight but measurable differences between the vanes that will be neglected in this work[246].

6. **Alula feathers** are treated as a point mass on Pt6 although their structure differs between species.

7. **Feather positioning:**

    - The base of the secondaries are equally spaced along the ulna and their tips are equally spaced along the line between Pt10 and Pt 11 (last secondary).
    - The base of P1 through P6 are equally spaced along the carpometacarpus and their tips are equally spaced along the line between Pt10 and Pt9.
    - The base P7 and up are located at the end of the carpometacarpus (Pt4) and their tips are equally spaced along the line between Pt9 and Pt8.

8. **Feather orientation:**

    - Primaries lay flat on the plane defined by Pt3, Pt4 and their tip position as defined above.
    - Secondaries lay flat on the plane defined by Pt2, Pt3 and their tip position as defined above.

A.4 Tertiaries and skin/coverts

The tertiary feathers and skin/coverts are modeled as flat triangular plates. The tertiary feather sections are defined as two sections, with vertices as follows: 1) Pt12, Pt2 and the trailing edge of the wing at the body and 2) Pt11, Pt2 and the trailing edge of the wing at the body. The skin/coverts section vertices are defined by Pt12, Pt2 and Pt6.

A.4.1 Methodology

1. Given the input positions calculate **I** and CG based on the general polygon formulations [247] within a frame of reference and about an origin that simplifies their formulation.

2. Transform **I** and CG to be within the full bird frame and shift so that the VRP is the origin.

A.4.2 Required measurements

1. Mass of the skin and coverts, m_{skin}

2. Mass of the tertiaries, $m_{tertiaries}$

A.4.3 Assumptions

1. **Skin density** (ρ_{skin}) treated as constant (1060 kg/m^3) based on a previously measured muscle-only measurement [236, 248]. This was used to calculate the final skin thickness based on ensuring that the volume would return the known mass of the section.

2. **Tertiary density** is treated as constant and equal to the cortex density (ρ_{cor})[238, 241–244] of 1150 kg/m^3. As with the skin this was used to calculate the final thickness of the tertiary sections based on ensuring that the volume would return the known mass of the section.

3. **Tertiary mass** is divided equally between the two tertiary sections.

A.5 Head, neck, legs and tail

The head (including the beak) was modeled as a solid cone, the neck was modeled as a solid cylinder, the legs were point masses and the tail was modeled as a flat rectangular plate.

A.5.1 Methodology

1. Calculate **I** and CG of the head (eqn. A.8 and eqn. A.14), neck (if used, eqn. A.6 and eqn. A.13) and tail (eqn. A.11).
2. Calculate **I** and CG of the legs as point masses placed on the ventral sides of the bird.
3. Transform **I** and CG to be within the full bird frame and shift so that the VRP is the origin.

A.5.2 Required measurements

1. Mass of the head, m_{head}
2. Length of the head (tip of beak to neck), l_{head}
3. Radius of the head (maximum), r_{head}
4. Mass of the neck, m_{neck}
5. Length of the neck outstretched, l_{neck}
6. Radius of the neck, r_{neck}
7. Mass of the tail, m_{tail}
8. Length of the furled tail, l_{tail}
9. Width of the furled tail, w_{tail}
10. Length of the torso + tail, l_{tot}
11. Mass of both legs, m_{leg}
12. x-location of leg insertion, l_{leg}

A.5.3 Assumptions

1. **Head/beak CG** was measured on the specimens and we found that for all of the measured species the head CG was within 15% of the quarter of the head length (See *"VerificationData.xlsx"* tab *"HeadCGVerification"* in the publicly available data repository). Thus, we assumed that a solid cone would be a fair approximation of the shape.

2. **Neck was only included for some species** that are known to stretch out their neck while in a cruise flight configuration. If not outstretched, the neck mass is added to the head mass. This can be adjusted for general use.

3. **Legs modeled as point masses** however some birds do stick their legs behind their body while in flight. Because grebes have very minimal tails and fly with their legs directly behind their bodies the grebes' legs were treated as a tail. However, for other species this effect was neglected in our work and should be investigated in future studies.

A.6 Torso

The torso is modeled as a structure composed of a hemiellipsoid, partial elliptical cone and either a full elliptical cone (3 individuals) or elliptical cylinder (33 individuals) (Fig. A.1). Due to the complex structure, the center of gravity position of the torso + tail must be measured and thus the code largely functions to estimate the associated moment of inertia for the torso. In the study, we performed a sensitivity analysis for up to 15% error of the total torso length on the CG measurement.

A.6.1 Methodology

1. Calculate the volume of each component assuming an elliptical cylinder for the back piece.

2. Option 1: If the calculated average density places the CG within 5% of the measured value, use the elliptical cylinder and continue to step 5.

3. Option 2: If not, calculate if the average density using an elliptical cone for a back piece places the CG within 5% of the measured value. If so, use the elliptical cone and continue to step 5. Figure A.1 illustrates option 2.

4. Option 3: If not, use an elliptical cylinder and an optimization routine to vary the density between each of the three sections of the torso. The routine minimizes the difference between the output densities and the calculated average density for the full torso. In

addition, we assume that the CG is moved forwards by 5% of the total length. This is necessary to ensure reasonable densities. We assumed that density measurements could be very low due to the possibility that the majority of the volume is made from loosely packed feathers. The lowest density was found to be 42 kg-m^{-3} for the end section of a storm petrel. All section densities can be seen within the *"VerificationData.xlsx"* tab *"TorsoDensities"* that is included within the publicly available data repository.

5. One of the three above options will provide the final calculated volume, mass and output CG.

6. Given these parameters for each section, calculate **I** (eqn. A.12, A.9 and A.7) and CG (eqn. A.15 and A.14) for each component in the torso frame, where $z_{torso} = -x_{fullbird}$, $x_{torso} = z_{fullbird}$ and $y_{torso} = y_{fullbird}$.

7. Transform **I** and CG to be within the full bird frame and shift so that the VRP is the origin.

A.6.2 Required measurements

1. Mass of the torso and legs, m_{torso}
2. Full torso length, l_{torso}
3. Mass of both legs, m_{leg}
4. Body width at leg insertion, w_{leg}
5. x-location of leg insertion, l_{leg}
6. Maximum body width, w_{max}
7. Maximum body height, h_{max}
8. x-location of maximum body width, l_{bmax}
9. x-location of the CG of torso + legs, CG_x
10. z-location of the CG of torso + legs, CG_z

A.6.3 Assumptions

1. **Minimum density** allowed by the optimizer for the front section is 200 kg/m^3.

A.7 Base moment of inertia tensors

All tensors are listed in a published handbook [249] except for the elliptical cone calculation which was computed for this project.

1. **Hollow cylinder.** r_o is the outer radius, r_i is the inner radius, l is the length and m is the mass. Origin is at the center of mass. Used for the bone interior, neck and feather calamus.

$$\mathbf{I} = m \begin{bmatrix} \frac{1}{12}(3(r_o^2 + r_i^2) + l^2) & 0 & 0 \\ 0 & \frac{1}{12}(3(r_o^2 + r_i^2) + l^2) & 0 \\ 0 & 0 & \frac{1}{2}(r_o^2 + r_i^2) \end{bmatrix} \tag{A.5}$$

2. **Solid cylinder.** r is the radius, l is the length and m is the mass. Origin is at the center of mass. Used for the bone end caps and muscles.

$$\mathbf{I} = m \begin{bmatrix} \frac{1}{12}(3r^2 + l^2) & 0 & 0 \\ 0 & \frac{1}{12}(3r^2 + l^2) & 0 \\ 0 & 0 & \frac{1}{2}r^2 \end{bmatrix} \tag{A.6}$$

3. **Elliptical cylinder.** a is half the maximum height along the x direction, b is half the maximum width along the y direction, l is the length, and m is the mass. Origin is at the center of mass. Used for the last portion of the body if required.

$$I = m \begin{bmatrix} \frac{1}{12}(3b^2 + l^2) & 0 & 0 \\ 0 & \frac{1}{12}(3a^2 + l^2) & 0 \\ 0 & 0 & \frac{1}{4}(a^2 + b^2) \end{bmatrix} \tag{A.7}$$

4. **Solid cone.** r is the radius of the cone base, h is the height and m is the mass. Origin is

at the center of the cone's base, not the center of mass. Used for the head/beak.

$$\mathbf{I} = m \begin{bmatrix} \frac{1}{10}(\frac{3}{2}r^2 + l^2) & 0 & 0 \\ 0 & \frac{1}{10}(\frac{3}{2}r^2 + l^2) & 0 \\ 0 & 0 & \frac{3}{10}r^2 \end{bmatrix} \tag{A.8}$$

5. **Elliptical cone.** l length until the tip of the cone, A is half the maximum height along the x direction, B is half the maximum width along the y direction, and m is the mass. Origin is at the base of the cone, not the center of mass. Used for the back two-thirds of the body.

$$I = m \begin{bmatrix} \frac{1}{10}(\frac{3}{2}B^2 + l^2) & 0 & 0 \\ 0 & \frac{1}{10}(\frac{3}{2}A^2 + l^2) & 0 \\ 0 & 0 & \frac{3}{20}(A^2 + B^2) \end{bmatrix} \tag{A.9}$$

6. **Solid square pyramid.** w is the entire width of one side of the pyramid base, h entire height of the pyramid and m is the mass. Origin is at the center of the pyramid's base, not the center of mass. Used for the rachis.

$$\mathbf{I} = m \begin{bmatrix} \frac{1}{20}(w^2 + 2h^2) & 0 & 0 \\ 0 & \frac{1}{20}(w^2 + 2h^2) & 0 \\ 0 & 0 & \frac{1}{10}w^2 \end{bmatrix} \tag{A.10}$$

7. **Flat rectangular plate.** w is the entire width of one side, h entire height and m is the mass. Origin is at the center of mass. Used for the feather vanes and tail.

$$\mathbf{I} = \frac{1}{12}m \begin{bmatrix} (w^2 + h^2) & 0 & 0 \\ 0 & h^2 & 0 \\ 0 & 0 & w^2 \end{bmatrix} \tag{A.11}$$

8. **Solid hemi-ellipsoid.** a is half the height along the x direction, b is half the width along the y direction and c is half the length along the z direction. Origin is at the base of the

hemi-ellipsoid, not the center of mass. Used for the front third of the body.

$$\mathbf{I} = \frac{1}{5}m \begin{bmatrix} (b^2+c^2) & 0 & 0 \\ 0 & (a^2+c^2) & 0 \\ 0 & 0 & (a^2+b^2) \end{bmatrix} \tag{A.12}$$

A.8 Base center of gravity vectors

1. **Cylinder.** (hollow, solid, elliptical or circular) l is the length. Origin at the center of the base.

$$CG = \begin{bmatrix} 0 \\ 0 \\ \frac{1}{2}l \end{bmatrix} \tag{A.13}$$

2. **Pyramid.** (circular, square or elliptical) h is the height. Origin at the center of the base.

$$CG = \begin{bmatrix} 0 \\ 0 \\ \frac{1}{4}h \end{bmatrix} \tag{A.14}$$

3. **Hemi-ellipsoid.** c is the height. Origin at the center of the base.

$$CG = \begin{bmatrix} 0 \\ 0 \\ \frac{3}{8}c \end{bmatrix} \tag{A.15}$$

A.9 Illustrations of the required measurements

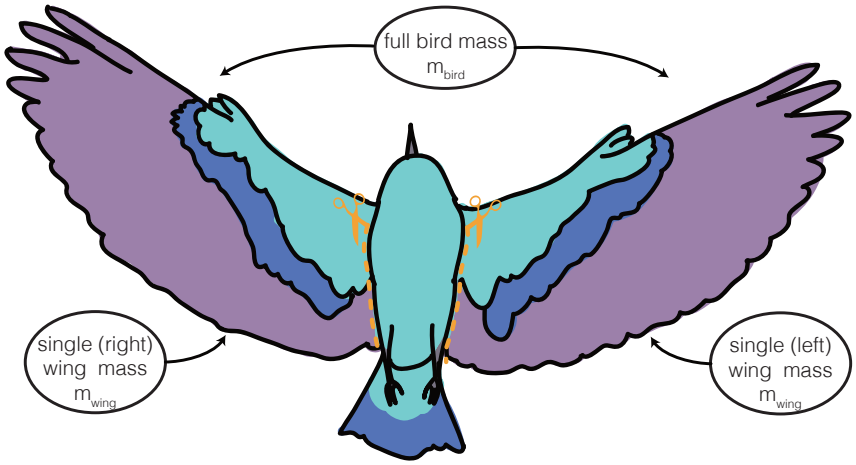

Figure A.4: **Entire bird measurements.** Drawn by J.C.M. Wong for [142].

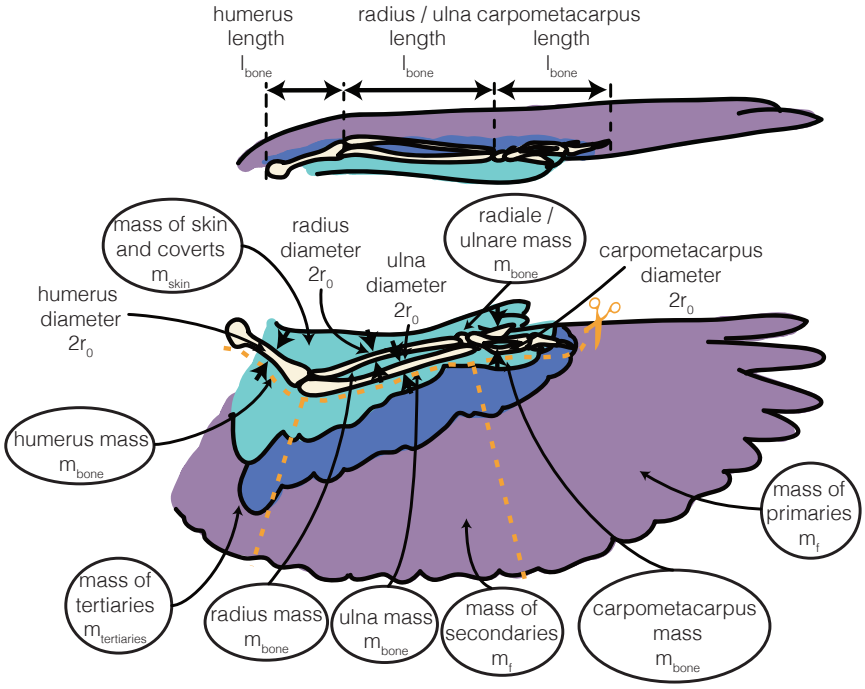

Figure A.5: **Wing specific measurements.** Drawn by J.C.M. Wong for [142].

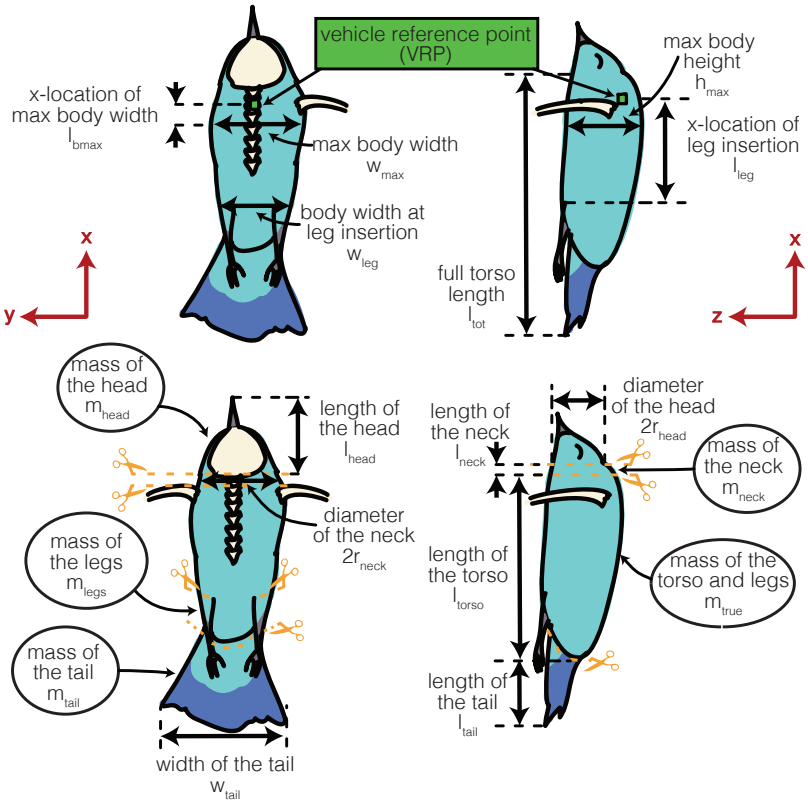

Figure A.6: **Body specific measurements.** Drawn by J.C.M. Wong for [142].

Bibliography

[1] N. Tesla. (1898). Method of and apparatus for controlling mechanism of moving vessels or vehicles. USA Patent, US613809A. URL: https://patents.google.com/patent/US613809A/en.

[2] L. R. Newcome. (2004). *Unmanned aviation: a brief history of unmanned aerial vehicles*. American Institute of Aeronautics and Astronautics, Reston, VA, USA.

[3] L. R. G. Carrillo, A. E. D. López, R. Lozano, C. Pégard. (2012). *Quad rotorcraft control: vision-based hovering and navigation*. Springer Science & Business Media.

[4] H. Everett. (2015). *Unmanned systems of World Wars I and II*. MIT Press.

[5] J. F. Keane, S. S. Carr. (2013). A brief history of early unmanned aircraft. *Johns Hopkins APL Technical Digest*, 32(3), 558–571.

[6] S. Barbarino, O. Bilgen, R. M. Ajaj, M. I. Friswell, D. J. Inman. (2011). A review of morphing aircraft. *Journal of Intelligent Material Systems and Structures*, 22, 823–877. doi: 10.1177/1045389x11414084.

[7] K. L. B. Cook. (2007). The Silent Force Multiplier: The History and Role of UAVs in Warfare, in: *2007 IEEE Aerospace Conference*, IEEE, 1–7. doi: 10.1109/AERO.2007.352737.

[8] P. D. Bravo-Mosquera, L. Botero-Bolivar, D. Acevedo-Giraldo, H. D. Cerón-Muñoz. (2017). Aerodynamic design analysis of a UAV for superficial research of volcanic environments. *Aerospace Science and Technology*, 70, 600–614. doi: 10.1016/j.ast.2017.09.005.

[9] T. F. Villa, F. Gonzalez, B. Miljievic, Z. D. Ristovski, L. Morawska. (2016). An Overview of Small Unmanned Aerial Vehicles for Air Quality Measurements: Present Applications and Future Prospectives. *Sensors*, 16(7). doi: 10.3390/s16071072.

[10] D. Hausamann, W. Zirnig, G. Schreier, P. Strobl. (2005). Monitoring of gas pipelines–a civil UAV application. *Aircraft Engineering and Aerospace Technology*, 77(5), 352–360. doi: 10.1108/00022660510617077.

[11] F. Outay, H. A. Mengash, M. Adnan. (2020). Applications of unmanned aerial vehicle (UAV) in road safety, traffic and highway infrastructure management: Recent advances and challenges. *Transportation Research Part A: Policy and Practice*, 141, 116–129. doi: 10.1016/j.tra.2020.09.018.

[12] E. Salamí, C. Barrado, E. Pastor. (2014). UAV Flight Experiments Applied to the Remote Sensing of Vegetated Areas. *Remote Sensing*, 6(11). doi: 10.3390/rs61111051.

[13] J. Kim, S. Kim, C. Ju, H. I. Son. (2019). Unmanned Aerial Vehicles in Agriculture: A Review of Perspective of Platform, Control, and Applications. *IEEE Access*, 7, 105100–105115. doi: 10.1109/ACCESS.2019.2932119.

[14] S. M. Adams, C. J. Friedland. (2011). A survey of unmanned aerial vehicle (UAV) usage for imagery collection in disaster research and management, in: *9th International Workshop on Remote Sensing for Disaster Response*, 8, 1–8.

[15] F. Greenwood, E. L. Nelson, P. G. Greenough. (2020). Flying into the hurricane: A case study of UAV use in damage assessment during the 2017 hurricanes in Texas and Florida. *PLOS ONE*, 15(2), e0227808. doi: 10.1371/journal.pone.0227808.

[16] J. Schenkel, P. Taele, D. Goldberg, J. Horney, T. Hammond. (2020). Identifying Potential Mosquito Breeding Grounds: Assessing the Efficiency of UAV Technology in Public Health. *Robotics*, 9(4). doi: 10.3390/robotics9040091.

[17] O. T. Michael, A. Olusegun, O. A. Paul, S. O. Felix, F. R. Kaniki, O. S. Ayosanmi, D. Wade, A. O. Faith, G. Z. Terna, A. Musa. (2019). The use of UAV/Drones in the

optimization of Nigeria vaccine supply chain. *International Journal of Scientific & Engineering Research*, 10(10), 1273–1279.

[18] I. Sung, P. Nielsen. (2020). Zoning a service area of unmanned aerial vehicles for package delivery services. *Journal of Intelligent & Robotic Systems*, 97(3), 719–731. doi: 10.1007/s10846-019-01045-7.

[19] M. G. Goman, A. V. Khramtsovsky, E. N. Kolesnikov. (2008). Evaluation of aircraft performance and maneuverability by computation of attainable equilibrium sets. *Journal of Guidance, Control, and Dynamics*, 31(2), 329–339. doi: 10.2514/1.29336.

[20] R. Dudley. (2002). Mechanisms and implications of animal flight maneuverability. *Integrative and Comparative Biology*, 42(1), 135–140. doi: 10.1093/icb/42.1.135.

[21] F. Gill, D. Donsker, P. Rasmussen. (2021). IOC World Bird List (v11.1). URL: 10.14344/IOC.ML.11.1.

[22] A. N. Iwaniuk, J. E. Nelson, H. F. James, S. L. Olson. (2004). A comparative test of the correlated evolution of flightlessness and relative brain size in birds. *Journal of Zoology*, 263(3), 317–327. doi: 10.1017/S0952836904005308.

[23] G. K. Taylor, A. C. Carruthers, T. Y. Hubel, S. M. Walker. (2012). Wing morphing in insects, birds and bats: mechanism and function, in: *Morphing Aerospace vehicles and structures*, John Wiley & Sons, Ltd, 11–40.

[24] J. W. Gerdes, S. K. Gupta, S. A. Wilkerson. (2012). A review of bird-inspired flapping wing miniature air vehicle designs. *Journal of Mechanisms and Robotics*, 4(2), 021003. doi: 10.1115/1.4005525.

[25] E. L. C. Shepard, C. Williamson, S. P. Windsor. (2016). Fine-scale flight strategies of gulls in urban airflows indicate risk and reward in city living. *Philosophical Transactions of the Royal Society B: Biological Sciences*, 371(1704), 20150394. doi: 10.1098/rstb.2015.0394.

[26] A. Hedenström, M. Rosén. (2001). Predator versus prey: on aerial hunting and escape strategies in birds. *Behavioral Ecology*, 12(2), 150–156. doi: 10.1093/beheco/12.2.150.

[27] R. H. Klaassen, B. J. Ens, J. Shamoun-Baranes, K.-M. Exo, F. Bairlein. (2012). Migration strategy of a flight generalist, the Lesser Black-backed Gull Larus fuscus. *Behavioral Ecology*, 23(1), 58–68. doi: 10.1093/beheco/arr150.

[28] J. Burger, M. Gochfeld. (1981). Age-related differences in piracy behaviour of four species of gulls, Larus. *Behaviour*, 77(4), 242–267.

[29] E. Ajanic, M. Feroskhan, S. Mintchev, F. Noca, D. Floreano. (2020). Bioinspired wing and tail morphing extends drone flight capabilities. *Science Robotics*, 5(47), eabc2897. doi: 10.1126/scirobotics.abc2897.

[30] A. A. Paranjape, S.-J. Chung, M. S. Selig. (2011). Flight mechanics of a tailless articulated wing aircraft. *Bioinspiration & Biomimetics*, 6(2), 026005. doi: 10.1088/1748-3182/6/2/026005.

[31] M. Abdulrahim, R. Lind. (2004). Flight testing and response characteristics of a variable gull-wing morphing aircraft, in: *AIAA Guidance, Navigation, and Control Conference and Exhibit*, American Institute of Aeronautics and Astronautics, Providence, RI, USA.

[32] E. Chang, L. Y. Matloff, A. K. Stowers, D. Lentink. (2020). Soft biohybrid morphing wings with feathers underactuated by wrist and finger motion. *Science Robotics*, 5(38). doi: 10.1126/scirobotics.aay1246.

[33] M. Di Luca, S. Mintchev, G. Heitz, F. Noca, D. Floreano. (2017). Bioinspired morphing wings for extended flight envelope and roll control of small drones. *Interface Focus*, 7(1), 20160092. doi: 10.1098/rsfs.2016.0092.

[34] G. C. Birch, J. C. Griffin, M. K. Erdman. (2015). UAS Detection, Classification, and Neutralization: Market Survey 2015. Technical Report SAND2015-6365, Sandia National Lab, Albuquerque, NM, USA. URL: https://doi.org/10.2172/1222445.

[35] R. V. Baudinette, K. Schmidt-Nielsen. (1974). Energy cost of gliding flight in herring gulls. *Nature*, 248, 83–84. doi: 10.1038/248083b0.

[36] P. L. Richardson. (2011). How do albatrosses fly around the world without flapping their wings? *Progress in Oceanography*, 88, 46–58. doi: 10.1016/j.pocean.2010.08.001.

[37] J. Videler, A. Groenewold. (1991). Field measurements of hanging flight aerodynamics in the kestrel Falco tinnunculus. *Journal of Experimental Biology*, 155(1), 519–530. doi: 10.1242/jeb.155.1.519.

[38] R. Spaar, B. Bruderer. (1997). Optimal flight behavior of soaring migrants: a case study of migrating steppe buzzards, Buteo buteo vulpinus. *Behavioral Ecology*, 8(3), 288–297. doi: 10.1093/beheco/8.3.288.

[39] P. Henningsson, A. Hedenström. (2011). Aerodynamics of gliding flight in common swifts. *Journal of Experimental Biology*, 214(3), 382–393. doi: 10.1242/jeb.050609.

[40] R. Ajaj, M. Friswell, M. Bourchak, W. Harasani. (2016). Span morphing using the GNATSpar wing. *Aerospace Science and Technology*, 53, 38–46. doi: 10.1016/j.ast.2016.03.009.

[41] T. Alerstam. (1975). Crane (Grus grus) migration over sea and land. *Ibis*, 117(4), 489–495. doi: 10.1111/j.1474-919X.1975.tb04241.x.

[42] T. Alerstam, G. A. Gudmundsson, B. Larsson. (1993). Flight tracks and speeds of Antarctic and Atlantic seabirds: radar and optical measurements. *Philosophical Transactions of the Royal Society of London. Series B: Biological Sciences*, 340(1291), 55–67. doi: 10.1098/rstb.1993.0048.

[43] R. Austin. (2011). *Unmanned aircraft systems: UAVS design, development and deployment*. John Wiley & Sons Ltd.

[44] J. Bäckman, T. Alerstam. (2001). Confronting the winds: orientation and flight behaviour of roosting swifts, Apus apus. *Proceedings of the Royal Society of London. Series B: Biological Sciences*, 268(1471), 1081–1087. doi: 10.1098/rspb.2001.1622.

[45] M. A. Barcala-Montejano, A. A. Rodríguez-Sevillano, J. Crespo-Moreno, R. Bardera-Mora, A. J. Silva-González. (2015). Optimized performance of a morphing micro air vehicle, in: *2015 International Conference on Unmanned Aircraft Systems (ICUAS)*, 794–800. doi: 10.1109/ICUAS.2015.7152363.

[46] M. Bronz, G. Hattenberger, J.-M. Moschetta. (2013). Development of a long endurance mini-uav: Eternity. *International Journal of Micro Air Vehicles*, 5(4), 261–272. doi: 10.1260/1756-8293.5.4.261.

[47] B. Bruderer, A. Boldt. (2001). Flight characteristics of birds: I. Radar measurements of speeds. *Ibis*, 143(2), 178–204. doi: 10.1111/j.1474-919X.2001.tb04475.x.

[48] V. S. Brusov, V. P. Petruchik. (2007). Theoretical and experimental investigations of aerodynamic characteristics for micro-UAV, in: *3rd US-European Competition and Workshop on Micro Air Vehicle Systems (MAV07) & European Micro Air Vehicle Conference and Flight Competition (EMAV2007)*, Toulouse, France, 17–21.

[49] D. Butler. (2011). The Design of a Competition Sailplane. URL: https://concordia-sailplane.com/design-of-a-competition-sailplane/.

[50] A. A. Demircali, H. Uvet. (2018). Mini Glider Design and Implementation with Wing-Folding Mechanism. *Applied Sciences*, 8(9), 1541. doi: 10.3390/app8091541.

[51] N. E. Durston, X. Wan, J. G. Liu, S. P. Windsor. (2019). Avian surface reconstruction in free flight with application to flight stability analysis of a barn owl and peregrine falcon. *Journal of Experimental Biology*, 222(9), jeb185488. doi: 10.1242/jeb.185488.

[52] H. Eder, W. Fiedler, M. Neuhäuser. (2015). Evaluation of aerodynamic parameters from infrared laser tracking of free-gliding white storks. *Journal of Ornithology*, 156, 667–677. doi: 10.1007/s10336-015-1176-7.

[53] D. Edwards. (2008). Performance Testing of RNR's SBXC Using a Piccolo Autopilot. URL: http://www.xcsoaring.com/techPicts/Edwards%20performance%20test.pdf.

[54] D. J. Edwards, A. D. Kahn, S. B. Heinzen, T. Z. Young, N. J. Arnold, D. Newton, B. Eber, S. V. Carter. (2018). CICADA Flying Circuit Board Unmanned Aerial Vehicle, in: *2018 AIAA Aerospace Sciences Meeting*, Kissimmee, FL, USA, 1008. doi: 10.2514/6.2018-1008.

[55] J. Grasmeyer, M. Keennon. (2001). Development of the black widow micro air vehicle, in: *39th Aerospace Sciences Meeting and Exhibit*, American Institute of Aeronautics and Astronautics, Reno, NV, USA, 127. doi: 10.2514/6.2001-127.

[56] H. Gruschka, I. Borchers, J. Coble. (1971). Aerodynamic noise produced by a gliding owl. *Nature*, 233, 409–411. doi: 10.1038/233409a0.

[57] D. Gyllhem, K. Mohseni, D. Lawrence, P. Geuzaine. (2005). Numerical simulation of flow around the Colorado micro aerial vehicle, in: *35th AIAA Fluid Dynamics Conference and Exhibit*, American Institute of Aeronautics and Astronautics, Toronto, ON, Canada, 4757. doi: 10.2514/6.2005-4757.

[58] M. Hacklinger. (1964). Theoretical and experimental investigation of indoor flying models. *The Aeronautical Journal*, 68(647), 728–734. doi: 10.1017/S0368393100080846.

[59] T. Hansen. (2014). Modeling the Performance of the Standard Cirrus Glider using Navier-Stokes CFD. *Technical Soaring*, 38(1), 5–14.

[60] M. Hassanalian. (2018). Conceptual Design, Bioinspiration, and Multidisciplinary Analysis of Drones, Ph.D. thesis, New Mexico State University, Las Cruces, NM, USA.

[61] A. Hedenström. (1995). Song flight performance in the skylark Alauda arvensis. *Journal of Avian Biology*, 26(4), 337–342.

[62] A. Hedenström, S. Åkesson. (2017). Adaptive airspeed adjustment and compensation for wind drift in the common swift: differences between day and night. *Animal Behaviour*, 127, 117–123. doi: 10.1016/j.anbehav.2017.03.010.

[63] T. L. Hedrick, C. Pichot, E. De Margerie. (2018). Gliding for a free lunch: biomechanics of foraging flight in common swifts (Apus apus). *Journal of Experimental Biology*, 221(22), jeb186270. doi: 10.1242/jeb.186270.

[64] R. Hoey. (2010). Exploring bird aerodynamics using radio-controlled models. *Bioinspiration & Biomimetics*, 5(4), 045008. doi: 10.1088/1748-3182/5/4/045008.

[65] N. Horvitz, N. Sapir, F. Liechti, R. Avissar, I. Mahrer, R. Nathan. (2014). The gliding speed of migrating birds: slow and safe or fast and risky? *Ecology Letters*, 17(6), 670–679. doi: 10.1111/ele.12268.

[66] P. Idrac. (1920). Soaring flight in Guinea. Technical Report NACA-TN-13, National Advisory Committee for Aeronautics. Langley Aeronautical Lab., Langley Field, VA, United States.

[67] A. R. Jenkins. (1995). Morphometrics and Flight Performance of Southern African Peregrine and Lanner Falcons. *Journal of Avian Biology*, 26, 49–58. doi: 10.2307/3677212.

[68] W. Jin, Y.-G. Lee. (2014). Computational analysis of the aerodynamic performance of a long-endurance UAV. *International Journal of Aeronautical and Space Sciences*, 15(4), 374–382. doi: 10.5139/IJASS.2014.15.4.374.

[69] S. Junlei, Z. Zhou, W. Heping, L. Shan. (2017). The Conceptual Design and Aerodynamic Characteristics Analysis of the Diamond Joined-Wing Configuration UAV, in: *2017 5th International Conference on Mechanical, Automotive and Materials Engineering (CMAME)*, IEEE, Guangzhou, China, 275–279. doi: 10.1109/CMAME.2017.8540111.

[70] J. Kellogg, C. Bovais, J. Dahlburg, R. Foch, J. Gardner, D. Gordon, R. Hartley, B. Kamgar-Parsi, H. McFarlane, F. Pipitone. (2001). The NRL MITE air vehicle. Technical Report ADA478713, Naval Research Lab, Washington, DC, USA. URL: https://apps.dtic.mil/sti/pdfs/ADA478713.pdf.

[71] J. Kosmatka. (2007). Development of a long-range small UAV for atmospheric monitoring, in: *48th AIAA/ASME/ASCE/AHS/ASC Structures, Structural Dynamics, and Materials Conference*, American Institute of Aeronautics and Astronautics, Honolulu, HI, USA, 2234. doi: 10.2514/6.2007-2234.

[72] M. Kovač, J.-C. Zufferey, D. Floreano. (2009). Towards a self-deploying and gliding robot, in: *Flying insects and robots*, Springer, 271–284.

[73] R. A. Kroeger, H. D. Grushka, T. C. Helvey. (1972). Low speed aerodynamics for ultra-quiet flight. Technical Report AD893426, The University of Tennessee Space Institute, Tullhoma, Tennessee. URL: https://apps.dtic.mil/sti/pdfs/AD0893426.pdf.

[74] L. K. Loftin. (1985). *Quest for performance: The evolution of modern aircraft*. Scientific and Technical Information Branch, National Aeronautics and Space Administration.

[75] M. Mateos-Rodríguez, B. Bruderer. (2012). Flight speeds of migrating seabirds in the Strait of Gibraltar and their relation to wind. *Journal of Ornithology*, 153(3), 881–889. doi: 10.1007/s10336-012-0814-6.

[76] J. McGahan. (1973). Gliding flight of the Andean condor in nature. *Journal of Experimental Biology*, 58(1), 225–237. doi: 10.1242/jeb.58.1.225.

[77] S. K. Meyer, R. Spaar, B. Bruderer. (2000). To cross the sea or to follow the coast? Flight directions and behaviour of migrating raptors approaching the Mediterranean Sea in autumn. *Behaviour*, 137(3), 379–399.

[78] R. A. Meyers. (1993). Gliding flight in the American kestrel (Falco sparverius): an electromyographic study. *Journal of Morphology*, 215(3), 213–224. doi: 10.1002/jmor.1052150304.

[79] H. L. Morgan Jr, J. W. Paulson Jr. (1979). Low-speed aerodynamic performance of a high-aspect-ratio supercritical-wing transport model equipped with full-span slat and part-span double-slotted flaps. Technical Report NASA-TP-1805, NASA Langley Research Center, Hampton, VA, United States. URL: https://ntrs.nasa.gov/archive/nasa/casi.ntrs.nasa.gov/19830022119.pdf.

[80] W. Null, S. Shkarayev. (2005). Effect of camber on the aerodynamics of adaptive-wing micro air vehicles. *Journal of Aircraft*, 42(6), 1537–1542. doi: 10.2514/1.12401.

[81] P. Panagiotou, P. Kaparos, K. Yakinthos. (2014). Winglet design and optimization for a MALE UAV using CFD. *Aerospace Science and Technology*, 39, 190–205. doi: 10.1016/j.ast.2014.09.006.

[82] G. C. Parrott. (1970). Aerodynamics of Gliding Flight of a Black Vulture Coragyps Atratus. *Journal of Experimental Biology*, 53(2), 363–374. doi: 10.1242/jeb.53.2.363.

[83] C. J. Pennycuick. (1971). Gliding flight of the white-backed vulture Gyps africanus. *Journal of Experimental Biology*, 55(1), 13–38. doi: 10.1242/jeb.55.1.13.

[84] C. J. Pennycuick. (1982). The Flight of Petrels and Albatrosses (Procellariiformes), Observed in South Georgia and its Vicinity. *Philosophical Transactions of the Royal Society of London. Series B, Biological Sciences*, 300(1098), 75–106. doi: 10.1098/rstb.1982.0158.

[85] C. J. Pennycuick. (1968). A wind-tunnel study of gliding flight in the pigeon Columba livia. *Journal of Experimental Biology*, 49(3), 509–526. doi: 10.1242/jeb.49.3.509.

[86] C. J. Pennycuick, T. Alerstam, B. Larsson. (1979). Soaring migration of the common crane Grus grus observed by radar and from an aircraft. *Ornis Scandinavica (Scandinavian Journal of Ornithology)*, 10(2), 241–251. doi: 10.2307/3676068.

[87] A. Raspet. (1960). Biophysics of bird flight. *Science*, 132, 191–200. doi: 10.1126/science.132.3421.191.

[88] N. C. Rattenborg, B. Voirin, S. M. Cruz, R. Tisdale, G. Dell'Omo, H.-P. Lipp, M. Wikelski, A. L. Vyssotski. (2016). Evidence that birds sleep in mid-flight. *Nature Communications*, 7, 12468. doi: 10.1038/ncomms12468.

[89] K. V. Reynolds, A. L. R. Thomas, G. K. Taylor. (2014). Wing tucks are a response to atmospheric turbulence in the soaring flight of the steppe eagle Aquila nipalensis. *Journal of The Royal Society Interface*, 11(101). doi: 10.1098/rsif.2014.0645.

[90] M. Rosén, A. Hedenström. (2002). Soaring Flight in the Eleonora's Falcon (Falco eleonorae). *The Auk*, 119(3), 835–840. doi: 10.1093/auk/119.3.835.

[91] M. Rosén, G. Spedding, A. Hedenström. (2007). Wake structure and wingbeat kinematics of a house-martin Delichon urbica. *Journal of The Royal Society Interface*, 4(15), 659–668. doi: 10.1098/rsif.2007.0215.

[92] M. Rosén, A. Hedenstrom. (2001). Gliding flight in a jackdaw: a wind tunnel study. *Journal of Experimental Biology*, 204(6), 1153–1166. doi: 10.1242/jeb.204.6.1153.

[93] R. C. B. Sampaio, A. C. Hernandes, M. Becker, F. M. Catalano, F. Zanini, J. L. Nobrega, C. Martins. (2014). Novel hybrid electric motor glider-quadrotor MAV for in-flight/V-STOL launching, in: *2014 IEEE Aerospace Conference*, IEEE, Big Sky, MT, USA, 1–12. doi: 10.1109/AERO.2014.6836414.

[94] E. Sarradj, C. Fritzsche, T. Geyer. (2011). Silent owl flight: Bird flyover noise measurements. *AIAA Journal*, 49(4), 769–779. doi: 10.2514/1.J050703.

[95] J. Shamoun-Baranes, E. van Loon. (2006). Energetic influence on gull flight strategy selection. *Journal of Experimental Biology*, 209(18), 3489–3498. doi: 10.1242/jeb.02385.

[96] H. Sharma, C. Suraj, A. Roshan, G. Ramesh, S. Ahmed, P. Narayan. (2013). Design of a High Altitude Fixed Wing Mini UAV–Aerodynamic Challenges, in: *9th International Conference on Intelligent Unmanned Systems*, Indian Institute of Technology Kanpur, Aeronautics Research and Development Board and Department of Science and Technology, Jaipur, Rajasthan, India.

[97] A. Shelton, A. Tomar, J. Prasad, M. J. Smith, N. Komerath. (2006). Active multiple winglets for improved unmanned-aerial-vehicle performance. *Journal of Aircraft*, 43(1), 110–116. doi: 10.2514/1.13987.

[98] G. R. Spedding. (1987). The wake of a kestrel (Falco tinnunculus) in gliding flight. *Journal of Experimental Biology*, 127(1), 45–57. doi: 10.1242/jeb.127.1.45.

[99] G. R. Spedding, M. Rosén, A. Hedenström. (2003). A family of vortex wakes generated by a thrush nightingale in free flight in a wind tunnel over its entire natural range of flight speeds. *Journal of Experimental Biology*, 206(14), 2313. doi: 10.1242/jeb.00423.

[100] B. Tobalske, K. Dial. (1996). Flight kinematics of black-billed magpies and pigeons over a wide range of speeds. *Journal of Experimental Biology*, 199(2), 263–280. doi: 10.1242/jeb.199.2.263.

[101] B. Tobalske, K. Dial. (1994). Neuromuscular control and kinematics of intermittent flight in budgerigars (Melopsittacus undulatus). *Journal of Experimental Biology*, 187(1), 1–18. doi: 10.1242/jeb.187.1.1.

[102] B. W. Tobalske. (1996). Scaling of muscle composition, wing morphology, and intermittent flight behavior in woodpeckers. *The Auk*, 113(1), 151–177. doi: 10.2307/4088943.

[103] B. Tobalske. (1995). Neuromuscular control and kinematics of intermittent flight in the European starling (Sturnus vulgaris). *Journal of Experimental Biology*, 198(6), 1259–1273. doi: 10.1242/jeb.198.6.1259.

[104] A. Tomaszewski, Z. J. Goraj. (2018). Assessment of a small UAV speed polar graph by conducting flight tests. *Aircraft Engineering and Aerospace Technology*, 91(5). doi: 10.1108/AEAT-03-2018-0099.

[105] V. A. Tucker. (1987). Gliding Birds: The Effect of Variable Wing Span. *Journal of Experimental Biology*, 133(1), 33–58. doi: 10.1242/jeb.133.1.33.

[106] V. A. Tucker, C. Heine. (1990). Aerodynamics of gliding flight in a Harris' hawk, Parabuteo unicinctus. *Journal of Experimental Biology*, 149(1), 469–489. doi: 10.1242/jeb.149.1.469.

[107] J. Wakeling, C. P. Ellington. (1997). Dragonfly flight. I. Gliding flight and steady-state aerodynamic forces. *Journal of Experimental Biology*, 200(3), 543–556. doi: 10.1242/jeb.200.3.543.

[108] A. Welch. (1973). Development of the competition glider. *The Aeronautical Journal*, 77(756), 612–619. doi: 10.1017/S0001924000042056.

[109] A. Welch. (1995). Evolution of the high performance glider. *The Aeronautical Journal*, 99(986), 243–259. doi: 10.1017/S0001924000049630.

[110] C. White, S. Watkins, E. W. Lim, K. Massey. (2012). The soaring potential of a micro air vehicle in an urban environment. *International Journal of Micro Air Vehicles*, 4(1), 1–13. doi: 10.1260/1756-8293.4.1.1.

[111] H. J. Williams, A. J. King, O. Duriez, L. Börger, E. L. Shepard. (2018). Social eavesdropping allows for a more risky gliding strategy by thermal-soaring birds. *Journal of The Royal Society Interface*, 15(148), 20180578. doi: 10.1098/rsif.2018.0578.

[112] C. J. Williamson, A. Spelt, S. P. Windsor. (2020). Bird-inspired Velocity Optimization for UAVs in the Urban Environment, in: *AIAA Scitech 2020 Forum*, American Institute of Aeronautics and Astronautics, Orlando, FL, USA, 1948. doi: 10.2514/6.2020-1948.

[113] T. Wolf, R. Konrath. (2015). Avian wing geometry and kinematics of a free-flying barn owl in flapping flight. *Experiments in Fluids*, 56(2), 28. doi: 10.1007/s00348-015-1898-6.

[114] W. Biesel, H. Butz, W. Nachtigall. (1985). Erste Messungen der Flügelgeometrie bei frei gleitfliegenden Haustauben (columbia livia var. domestica) unter Benutzung neu ausgearbeiteter Verfahren der Windkanaltechnik und der Stereophotogrammetrie. *Bionareport*, 3, 139–160.

[115] J. D. Anderson Jr. (1990). *Modern compressible flow: with historical perspective*. McGraw-Hill New York.

[116] R. O. Prum, J. S. Berv, A. Dornburg, D. J. Field, J. P. Townsend, E. M. Lemmon, A. R. Lemmon. (2015). A comprehensive phylogeny of birds (Aves) using targeted next-generation DNA sequencing. *Nature*, 526(7574), 569–573. doi: 10.1038/nature15697.

[117] T. Alerstam, M. Rosén, J. Bäckman, P. G. P. Ericson, O. Hellgren. (2007). Flight Speeds among Bird Species: Allometric and Phylogenetic Effects. *PLOS Biology*, 5(8), e197. doi: 10.1371/journal.pbio.0050197.

[118] B. Carmichael. (1981). Low Reynolds number airfoil survey, volume 1. Technical Report NASA-CR-165803-VOL-1, National Aeronautics and Space Administration, Capistrano Beach, CA, USA. URL: https://ntrs.nasa.gov/citations/19820006186.

[119] P. Lissaman. (1983). Low Reynolds number airfoils. *Annual Review of Fluid Mechanics*, 15(1), 223–239. doi: 10.1146/annurev.fl.15.010183.001255.

[120] D. Lentink, R. de Kat. (2014). Gliding Swifts Attain Laminar Flow over Rough Wings. *PLoS ONE*, 9(6), e99901. doi: 10.1371/journal.pone.0099901.

[121] P. Butler, A. Woakes. (1980). Heart rate, respiratory frequency and wing beat frequency of free flying barnacle geese Branta leucopsis. *Journal of Experimental Biology*, 85(1), 213–226. doi: 10.1242/jeb.85.1.213.

[122] C. Harvey, D. J. Inman. (2021). Aerodynamic efficiency of gliding birds vs. comparable UAVs: a review. *Bioinspiration & Biomimetics*, 16(3), 031001. doi: 10.1088/1748-3190/abc86a.

[123] J. Winslow, H. Otsuka, B. Govindarajan, I. Chopra. (2018). Basic Understanding of Airfoil Characteristics at Low Reynolds Numbers (10 4–10 5). *Journal of Aircraft*, 55(3), 1050–1061. doi: 10.2514/1.C034415.

[124] V. A. Tucker, G. C. Parrott. (1970). Aerodynamics of gliding flight in a falcon and other birds. *Journal of Experimental Biology*, 52, 345–367. doi: 10.1242/jeb.52.2.345.

[125] S. V. Shkarayev, P. G. Ifju, J. C. Kellogg, T. J. Mueller. (2007). *Introduction to the design of fixed-wing micro air vehicles including three case studies*. American Institute of Aeronautics and Astronautics.

[126] V. B. Baliga, I. Szabo, D. L. Altshuler. (2019). Range of motion in the avian wing is strongly associated with flight behavior and body mass. *Science Advances*, 5(10), eaaw6670. doi: 10.1126/sciadv.aaw6670.

[127] D. Lentink, U. K. Müller, E. J. Stamhuis, R. de Kat, W. van Gestel, L. L. M. Veldhuis, P. Henningsson, A. Hedenström, J. J. Videler, J. L. van Leeuwen. (2007). How swifts control their glide performance with morphing wings. *Nature*, 446, 1082. doi: 10.1038/nature05733.

[128] C. Harvey, V. B. Baliga, P. Lavoie, D. L. Altshuler. (2019). Wing morphing allows gulls to modulate static pitch stability during gliding. *Journal of The Royal Society Interface*, 16(150), 20180641. doi: 10.1098/rsif.2018.0641.

[129] C. Harvey, L. L. Gamble, C. R. Bolander, D. F. Hunsaker, J. J. Joo, D. J. Inman. (2022). A review of avian-inspired morphing for UAV flight control. *Progress in Aerospace Sciences*, 132, 100825. doi: 10.1016/j.paerosci.2022.100825.

[130] D. L. Altshuler, J. W. Bahlman, R. Dakin, A. H. Gaede, B. Goller, D. Lentink, P. S. Segre, D. A. Skandalis. (2015). The biophysics of bird flight: functional relationships integrate aerodynamics, morphology, kinematics, muscles, and sensors. *Canadian Journal of Zoology*, 93(12), 961–975. doi: 10.1139/cjz-2015-0103.

[131] N. Shubin, C. Tabin, S. Carroll. (1997). Fossils, genes and the evolution of animal limbs. *Nature*, 388(6643), 639–648. doi: 10.1038/41710.

[132] H. I. Fisher. (1957). Bony mechanism of automatic flexion and extension in the pigeon's wing. *Science*, 126(3271), 446–446. doi: 10.1126/science.126.3271.446.a.

[133] A. K. Stowers, L. Y. Matloff, D. Lentink. (2017). How pigeons couple three-dimensional elbow and wrist motion to morph their wings. *Journal of The Royal Society Interface*, 14. doi: 10.1098/rsif.2017.0224.

[134] T. L. Hieronymus. (2016). Flight feather attachment in rock pigeons (Columba livia): covert feathers and smooth muscle coordinate a morphing wing. *Journal of Anatomy*, 229(5), 631–656. doi: 10.1111/joa.12511.

[135] R. J. Raikow, L. Bicanovsky, A. H. Bledsoe. (1988). Forelimb joint mobility and the evolution of wing-propelled diving in birds. *The Auk*, 105(3), 446–451. doi: 10.1093/auk/105.3.446.

[136] D. L. Altshuler, M. V. Srinivasan. (2018). Comparison of Visually Guided Flight in Insects and Birds. *Frontiers in Neuroscience*, 12, 157. doi: 10.3389/fnins.2018.00157.

[137] A. L. R. Thomas, G. K. Taylor. (2001). Animal flight dynamics I. Stability in gliding flight. *Journal of Theoretical Biology*, 212, 399–424. doi: http://dx.doi.org/10.1006/jtbi.2001.2387.

[138] B. N. Pamadi. (2004). *Performance, Stability, Dynamics, and Control of Airplanes*. American Institute of Aeronautics and Astronautics.

[139] R. C. Nelson. (1998). *Flight stability and automatic control*. volume 2, WCB/McGraw Hill New York.

[140] J. D. Anderson Jr. (1989). *Introduction to Flight*. 3 ed., McGraw-Hill Higher Education.

[141] C. Harvey, V. B. Baliga, C. D. Goates, D. F. Hunsaker, D. J. Inman. (2021). Gull-inspired joint-driven wing morphing allows adaptive longitudinal flight control. *Journal of The Royal Society Interface*, 18(179), 20210132. doi: 10.1098/rsif.2021.0132.

[142] C. Harvey, V. B. Baliga, J. C. M. Wong, D. L. Altshuler, D. J. Inman. (2022). Birds can transition between stable and unstable states via wing morphing. *Nature*, 603(7902), 648–653. doi: 10.1038/s41586-022-04477-8.

[143] J. Valasek. (2012). *Morphing aerospace vehicles and structures*. John Wiley & Sons.

[144] S. Mintchev, D. Floreano. (2016). Adaptive morphology: A design principle for multimodal and multifunctional robots. *IEEE Robotics & Automation Magazine*, 23(3), 42–54. doi: 10.1109/MRA.2016.2580593.

[145] A. M. Wickenheiser, E. Garcia. (2008). Optimization of perching maneuvers through vehicle morphing. *Journal of Guidance, Control, and Dynamics*, 31(4), 815–823. doi: 10.2514/1.33819.

[146] P. Lissaman. (2009). Effects of turbulence on bank upsets of small flight vehicles, in: *47th AIAA Aerospace Sciences Meeting including The New Horizons Forum and Aerospace Exposition*, Aerospace Sciences Meetings, American Institute of Aeronautics and Astronautics. doi: 10.2514/6.2009-65.

[147] M. W. Orr, S. J. Rasmussen, E. D. Karni, W. B. Blake. (2005). Framework for developing and evaluating MAV control algorithms in a realistic urban setting, in: *Proceedings of the 2005, American Control Conference, 2005*, IEEE, Portland, OR, USA, 6, 4096–4101. doi: 10.1109/ACC.2005.1470619.

[148] C. Harvey, V. B. Baliga, D. L. Altshuler, D. J. Inman. (2019). Pitch Control Effectiveness of the Avian Elbow and Wrist via a Numerical Lifting Line Analysis, in: *AIAA Scitech 2019 Forum*, American Institute of Aeronautics and Astronautics. doi: 10.2514/6.2019-0853.

[149] B. Lazos, K. Visser. (2006). Aerodynamic comparison of hyper-elliptic cambered span (HECS) wings with conventional configurations, in: *24th AIAA Applied Aerodynamics Conference*, American Institute of Aeronautics and Astronautics, San Francisco, CA, USA, 1–18. doi: 10.2514/6.2006-3469.

[150] G. Taylor, A. Thomas. (2014). *Evolutionary biomechanics*. OUP Oxford.

[151] R. A. Meyers, E. Mathias. (1997). Anatomy and histochemistry of spread-wing posture in birds. 2. Gliding flight in the California gull, Larus californicus: a paradox of fast fibers and posture. *Journal of Morphology*, 233(3), 237–247. doi: 10.1002/(SICI)1097-4687(199709)233:3¡237::AID-JMOR3¿3.0.CO;2-0.

[152] AeroLab. (2020). MachUpX: Fast and accurate aerodynamic modelling using lifting-line theory. URL: https://www.github.com/usuaero/MachUpX.

[153] J. T. Reid, D. F. Hunsaker. (2020). A General Approach to Lifting-Line Theory, Applied to Wings with Sweep. *Journal of Aircraft*, 58(2), 1287. doi: 10.2514/1.C035994.

[154] C. D. Goates, D. F. Hunsaker. (2021). Practical Implementation of a General Numerical Lifting-Line Method, in: *AIAA Scitech 2021 Forum*, American Institute of Aeronautics and Astronautics, Virtual. doi: 10.2514/6.2021-0118.

[155] T. L. Hedrick. (2008). Software techniques for two- and three-dimensional kinematic measurements of biological and biomimetic systems. *Bioinspiration & Biomimetics*, 3(3), 034001. doi: 10.1088/1748-3182/3/3/034001.

[156] S. Lee, H. Choi. (2017). Characteristics of the alula in relation to wing and body size in the Laridae and Sternidae. *Animal Cells and Systems*, 21(1), 63–69. doi: 10.1080/19768354.2016.1266287.

[157] R. Nudds, J. Rayner. (2006). Scaling of body frontal area and body width in birds. *Journal of Morphology*, 267(3), 341–346. doi: 10.1002/jmor.10409.

[158] T. Liu, K. Kuykendoll, R. Rhew, S. Jones. (2006). Avian Wing Geometry and Kinematics. *AIAA Journal*, 44(5), 954–963. doi: 10.2514/1.16224.

[159] T. Bachmann. (2010). Anatomical, morphometrical and biomechanical studies of barn owls' and pigeons' wings, Ph.D. thesis, RWTH Aachen University, Aachen, Germany.

[160] W. Nachtigall, J. Wieser. (1966). Profilmessungen am Taubenflugel. *Zeitschrift fur vergleichende Physiologie*, 52(4), 333–346. doi: 10.1007/BF00302288.

[161] A. C. Carruthers, S. M. Walker, A. L. R. Thomas, G. K. Taylor. (2010). Aerodynamics of aerofoil sections measured on a free-flying bird. *Proceedings of the Institution of Mechanical Engineers, Part G: Journal of Aerospace Engineering*, 224(8), 855–864. doi: 10.1243/09544100jaero737.

[162] M. Drela. (1989). XFOIL: An Analysis and Design System for Low Reynolds Number Airfoils, in: T. J. Mueller (Ed.), *Low Reynolds Number Aerodynamics*, volume 54 of *Lecture Notes in Engineering*, Springer, Berlin, Germany, 1–12.

[163] J. B. Barlow, W. H. Rae, A. Pope. (1999). *Low-speed wind tunnel testing*. John Wiley & Sons.

[164] JCGM. (2008). Evaluation of measurement data - Guide to the expression of uncertainty in measurement. Technical Report JCGM 100:2008, Joint Committee for Guides in Metrology (JCGM/WG 1).

[165] I. Ucar, E. Pebesma, A. Azcorra. (2018). Measurement Errors in R. *R Journal*, 10(2), 549–557. doi: 10.32614/RJ-2018-075.

[166] J. van Ingen. (2008). The eN Method for Transition Prediction. Historical Review of Work at TU Delft, in: *38th Fluid Dynamics Conference and Exhibit*, Fluid Dynamics and Co-located Conferences, American Institute of Aeronautics and Astronautics. doi: 10.2514/6.2008-3830.

[167] B. Schloerke, J. Crowley, D. Cook, H. Hofmann, H. Wickham, F. Briatte, M. Marbach, E. Thoen, A. Elberg, J. Larmarange. (2020). GGally: Extension to ggplot2. URL: https://github.com/ggobi/ggally.

[168] D. McLean. (2012). *Understanding aerodynamics: arguing from the real physics*. John Wiley & Sons.

[169] R. Guiler, W. Huebsch. (2005). Wind tunnel analysis of a morphing swept wing tailless aircraft, in: *23rd AIAA Applied Aerodynamics Conference*, American Institute of Aeronautics and Astronautics, Toronto, ON, Canada, 4981. doi: 10.2514/6.2005-4981.

[170] S. Nakagawa, H. Schielzeth. (2013). A general and simple method for obtaining R2 from generalized linear mixed-effects models. *Methods in Ecology and Evolution*, 4(2), 133–142. doi: 10.1111/j.2041-210x.2012.00261.x.

[171] K. Barton. (2009). MuMIn: multi-model inference. URL: https://CRAN.R-project.org/package=MuMIn.

[172] N. Hamilton. (2015). contoureR: Contouring of Non-Regular Three-Dimensional Data. URL: https://cran.r-project.org/web/packages/contoureR/index.html.

[173] J. Manzo, E. Garcia. (2010). Demonstration of an in situ morphing hyperelliptical cambered span wing mechanism. *Smart Materials and Structures*, 19(2), 025012. doi: 10.1088/0964-1726/19/2/025012.

[174] R. Dakin, P. S. Segre, A. D. Straw, D. L. Altshuler. (2018). Morphology, muscle capacity, skill, and maneuvering ability in hummingbirds. *Science*, 359(6376), 653. doi: 10.1126/science.aao7104.

[175] D. R. Warrick. (1998). The turning-and linear-maneuvering performance of birds: the cost of efficiency for coursing insectivores. *Canadian Journal of Zoology*, 76(6), 1063–1079. doi: 10.1139/z98-044.

[176] I. G. Ros, L. C. Bassman, M. A. Badger, A. N. Pierson, A. A. Biewener. (2011). Pigeons steer like helicopters and generate down- and upstroke lift during low speed turns. *Proceedings of the National Academy of Sciences*, 108(50), 19990–19995. doi: 10.1073/pnas.1107519108.

[177] J. A. Gillies, A. L. Thomas, G. K. Taylor. (2011). Soaring and manoeuvring flight of a steppe eagle Aquila nipalensis. *Journal of Avian Biology*, 42(5), 377–386. doi: 10.1111/j.1600-048X.2011.05105.x.

[178] J. M. Smith. (1952). The importance of the nervous system in the evolution of animal flight. *Evolution*, 6(1), 127–129. doi: 10.2307/2405510.

[179] H. Baruh. (1999). *Analytical dynamics*. WCB/McGraw-Hill Boston.

[180] B. Obradovic, K. Subbarao. (2011). Modeling of flight dynamics of morphing wing aircraft. *Journal of Aircraft*, 48(2), 391–402. doi: 10.2514/1.C000269.

[181] D. R. Warrick, M. W. Bundle, K. P. Dial. (2002). Bird Maneuvering Flight: Blurred Bodies, Clear Heads. *Integrative and Comparative Biology*, 42(1), 141–148. doi: 10.1093/icb/42.1.141.

[182] T. L. Hedrick, J. R. Usherwood, A. A. Biewener. (2004). Wing inertia and whole-body acceleration: an analysis of instantaneous aerodynamic force production in cockatiels (Nymphicus hollandicus) flying across a range of speeds. *Journal of Experimental Biology*, 207(10), 1689–1702. doi: 10.1242/jeb.00933.

[183] G. Ducci, V. Colognesi, G. Vitucci, P. Chatelain, R. Ronsse. (2021). Stability and Sensitivity Analysis of Bird Flapping Flight. *Journal of Nonlinear Science*, 31(2), 47. doi: 10.1007/s00332-021-09698-1.

[184] R. Mills, H. Hildenbrandt, G. K. Taylor, C. K. Hemelrijk. (2018). Physics-based simulations of aerial attacks by peregrine falcons reveal that stooping at high speed maximizes catch success against agile prey. *PLOS Computational Biology*, 14(4), e1006044. doi: 10.1371/journal.pcbi.1006044.

[185] J. A. Cheney, J. P. J. Stevenson, N. E. Durston, M. Maeda, J. Song, D. A. Megson-Smith, S. P. Windsor, J. R. Usherwood, R. J. Bomphrey. (2021). Raptor wing morphing with flight speed. *Journal of The Royal Society Interface*, 18(180), 20210349. doi: 10.1098/rsif.2021.0349.

[186] C. A. Schneider, W. S. Rasband, K. W. Eliceiri. (2012). NIH Image to ImageJ: 25 years of image analysis. *Nature Methods*, 9, 671. doi: 10.1038/nmeth.2089.

[187] R. Team. (2016). RStudio: Integrated Development Environment for R.

[188] R. C. Team. (2017). R: A Language and Environment for Statistical Computing.

[189] V. Allen, H. Paxton, J. R. Hutchinson. (2009). Variation in center of mass estimates for extant sauropsids and its importance for reconstructing inertial properties of extinct archosaurs. *The Anatomical Record: Advances in Integrative Anatomy and Evolutionary Biology: Advances in Integrative Anatomy and Evolutionary Biology*, 292(9), 1442–1461. doi: 10.1002/ar.20973.

[190] C. Berg, J. Rayner. (1995). The moment of inertia of bird wings and the inertial power requirement for flapping flight. *Journal of Experimental Biology*, 198(8), 1655–1664. doi: 10.1242/jeb.198.8.1655.

[191] S. J. Kirkpatrick. (1990). Short communication the moment of inertia of bird wings. *Journal of Experimental Biology*, 151(1), 489–494. doi: 10.1242/jeb.151.1.489.

[192] C. J. Pennycuick, A. Lock. (1976). Elastic energy storage in primary feather shafts. *Journal of Experimental Biology*, 64(3), 677. doi: 10.1242/jeb.64.3.677.

[193] J. D. Hadfield. (2010). MCMC methods for multi-response generalized linear mixed models: the MCMCglmm R package. *Journal of Statistical Software*, 33(2), 1–22. doi: 10.18637/jss.v033.i02.

[194] M. S. Ben-Shachar, D. Lüdecke, D. Makowski. (2020). effectsize: Estimation of Effect Size Indices and Standardized Parameters. *Journal of Open Source Software*, 5(56), 2815. doi: 10.21105/joss.02815.

[195] J. Cohen. (1973). Eta-Squared and Partial Eta-Squared in Fixed Factor Anova Designs. *Educational and Psychological Measurement*, 33(1), 107–112. doi: 10.1177/001316447303300111.

[196] W. Maybury, J. Rayner, L. Couldrick. (2001). Lift generation by the avian tail. *Proceedings of the Royal Society of London. Series B: Biological Sciences*, 268(1475), 1443–1448. doi: 10.1098/rspb.2001.1666.

[197] J. D. Anderson Jr. (2010). *Fundamentals of aerodynamics*. 3 ed., McGraw-Hill Education.

[198] W. Phillips, D. F. Hunsaker, R. Niewoehner. (2008). Estimating the subsonic aerodynamic center and moment components for swept wings. *Journal of Aircraft*, 45(3), 1033–1043. doi: 10.2514/1.33445.

[199] A. H. Yates. (1952). Notes on the Mean Aerodynamic Chord and the Mean Aerodynamic Centre of a Wing. *The Journal of the Royal Aeronautical Society*, 56(498), 461–474. doi: 10.1017/S0368393100129311.

[200] W. S. Diehl. (1942). The mean aerodynamic chord and the aerodynamic center of a tapered wing. Technical Report NACA-TR-751, National Advisory Committee for Aeronautics. URL: https://ntrs.nasa.gov/citations/19930091829.

[201] W. Phillips, R. Niewoehner. (2009). Characteristic length and dynamic time scale associated with aircraft pitching motion. *Journal of Aircraft*, 46(2), 572–582. doi: 10.2514/1.38724.

[202] D. Neal, M. Good, C. Johnston, H. Robertshaw, W. Mason, D. Inman. (2004). Design and wind-tunnel analysis of a fully adaptive aircraft configuration, in: *45th AIAA/ASME/ASCE/AHS/ASC Structures, Structural Dynamics & Materials Conference*,

American Institute of Aeronautics and Astronautics, Palm Springs, CA, USA, 1727. doi: 10.2514/6.2004-1727.

[203] M. W. Pennell, J. M. Eastman, G. J. Slater, J. W. Brown, J. C. Uyeda, R. G. FitzJohn, M. E. Alfaro, L. J. Harmon. (2014). geiger v2.0: an expanded suite of methods for fitting macroevolutionary models to phylogenetic trees. *Bioinformatics*, 30(15), 2216–2218. doi: 10.1093/bioinformatics/btu181.

[204] N. Cooper, G. H. Thomas, C. Venditti, A. Meade, R. P. Freckleton. (2016). A cautionary note on the use of Ornstein Uhlenbeck models in macroevolutionary studies. *Biological Journal of the Linnean Society*, 118(1), 64–77. doi: 10.1111/bij.12701.

[205] C. Boettiger, G. Coop, P. Ralph. (2012). Is your phylogeny informative? Measuring the power of comparative methods. *Evolution*, 66(7), 2240–2251. doi: 10.1111/j.1558-5646.2011.01574.x.

[206] D. P. Raymer. (1999). *Aircraft Design: A Conceptual Approach*. American Institute of Aeronautics and Astronautics.

[207] J. R. Rivera Parga. (2004). Wind Tunnel Investigation of the Static Stability and Control Effectiveness of a Rotary Tail in a Portable UAV. Master's thesis, Air Force Institute of Technology, Wright-Patterson Air Force Base, Ohio.

[208] J. R. Usherwood, J. A. Cheney, J. Song, S. P. Windsor, J. P. J. Stevenson, U. Dierksheide, A. Nila, R. J. Bomphrey. (2020). High aerodynamic lift from the tail reduces drag in gliding raptors. *Journal of Experimental Biology*, 223(3), jeb214809. doi: 10.1242/jeb.214809.

[209] R. Hewson. (1957). Social flying in ravens. *British Birds*, 50, 432–434.

[210] Y. Ropert-Coudert, D. Grémillet, P. Ryan, A. Kato, Y. Naito, Y. Le Maho. (2004). Between air and water: the plunge dive of the Cape Gannet Morus capensis. *Ibis*, 146(2), 281–290. doi: 10.1111/j.1474-919x.2003.00250.x.

[211] F. Headley. (1912). Sailing Flight of Birds. *Nature*, 90, 220. doi: 10.1038/090220b0.

[212] N. M. Noor, A. Abdullah, M. Hashim. (2018). Remote sensing UAV/drones and its applications for urban areas: A review, in: *9th IGRSM International Conference and Exhibition on Geospatial & Remote Sensing (IGRSM 2018)*, IOP Publishing, Kuala Lumpur, Malaysia, 169, 012003. doi: 10.1088/1755-1315/169/1/012003.

[213] A. Paranjape, N. Sinha, N. Ananthkrishnan. (2007). Use of Bifurcation and Continuation Methods for Aircraft Trim and Stability Analysis - A State-of-the-Art, in: *45th AIAA Aerospace Sciences Meeting and Exhibit*, American Institute of Aeronautics and Astronautics. doi: 10.2514/6.2007-1051.

[214] Department of Defence. (1980). Flying qualities of piloted airplanes. Technical Report MIL-F-8785C, Department of Defence, Wright-Patterson Air Force Base, OH, USA.

[215] M. C. Cotting. (2010). Evolution of flying qualities analysis: Problems for a new generation of aircraft, Ph.D. thesis, Virginia Polytechnic Institute and State University, Blacksburg, Virginia.

[216] J. P. Kim. (2016). Evaluation of Unmanned Aircraft Flying Qualities Using JSBSim. Master's thesis, Air Force Institute of Technology, Wright-Patterson AFB, OH, USA.

[217] E. Capello, G. Guglieri, P. Marguerettaz, F. Quagliotti. (2012). Preliminary assessment of flying and handling qualities for mini-UAVs. *Journal of Intelligent & Robotic Systems*, 65(1), 43–61. doi: 10.1007/s10846-011-9565-5.

[218] T. Foster, J. Bowman. (2005). Dynamic stability and handling qualities of small unmanned-aerial vehicles, in: *43rd AIAA Aerospace Sciences Meeting and Exhibit*, American Institute of Aeronautics and Astronautics, Reno, NV, USA, 1023. doi: 10.2514/6.2005-1023.

[219] N. Durston. (2019). Quantifying the flight stability of free-gliding birds of prey, Ph.D. thesis, University of Bristol, Bristol, UK.

[220] O. Selim, E. R. Gowree, C. Lagemann, E. Talboys, C. Jagadeesh, C. Brücker. (2021). Peregrine Falcon's Dive: Pullout Maneuver and Flight Control Through Wing Morphing. *AIAA Journal*, 59(10), 1–9. doi: 10.2514/1.J060052.

[221] W. H. Press, W. T. Vetterling, S. A. Teukolsky, B. P. Flannery. (1986). *Numerical Recipes*. 1 ed., Cambridge University Press.

[222] R. Murray, et. al. (2021). Control Systems Library for Python. URL: http://github.com/python-control/python-control.

[223] V. A. Tucker. (1992). Pitching Equilibrium, Wing Span and Tail Span in a Gliding Harris' Hawk, Parabuteo Unicinctus. *Journal of Experimental Biology*, 165(1), 21. doi: 10.1242/jeb.165.1.21.

[224] C. Harvey, V. B. Baliga, D. L. Altshuler, P. Lavoie. (2018). Observational Photos and digitized files: Wing morphing allows gulls to modulate static pitch stability during gliding. URL: https://doi.org/10.6084/m9.figshare.7436948.v1.

[225] J. Berndt. (2004). JSBSim: An open source flight dynamics model in C++, in: *AIAA Modeling and Simulation Technologies Conference and Exhibit*, American Institute of Aeronautics and Astronautics, Providence, RI, USA, 4923. doi: 10.2514/6.2004-4923.

[226] J. J. Videler, D. Weihs, S. DAAN. (1983). Intermittent Gliding in the Hunting Flight of the Kestrel, Falco Tinnunculus L. *Journal of Experimental Biology*, 102(1), 1–12. doi: 10.1242/jeb.102.1.1.

[227] E. Shepard, E.-L. Cole, A. Neate, E. Lempidakis, A. Ross. (2019). Wind prevents cliff-breeding birds from accessing nests through loss of flight control. *eLife*, 8, e43842. doi: 10.7554/eLife.43842.

[228] J. A. Cheney, J. P. Stevenson, N. E. Durston, J. Song, J. R. Usherwood, R. J. Bomphrey, S. P. Windsor. (2020). Bird wings act as a suspension system that rejects gusts. *Proceedings of the Royal Society B*, 287(1937), 20201748. doi: 10.1098/rspb.2020.1748.

[229] V. A. Tucker. (1972). Metabolism during flight in the laughing gull, Larus atricilla. *American Journal of Physiology*, 222(2), 237–245. doi: 10.1152/ajplegacy.1972.222.2.237.

[230] L. L. Gamble, C. Harvey, D. J. Inman. (2020). Load alleviation of feather-inspired compliant airfoils for instantaneous flow control. *Bioinspiration & Biomimetics*, 15(5), 056010. doi: 10.1088/1748-3190/ab9b6f.

[231] C. Pennycuick. (1967). The strength of the pigeon's wing bones in relation to their function. *Journal of Experimental Biology*, 46(2), 219–233. doi: 10.1242/jeb.46.2.219.

[232] C. A. Marelli, E. L. R. Simons. (2014). Microstructure and Cross-Sectional Shape of Limb Bones in Great Horned Owls and Red-Tailed Hawks: How Do These Features Relate to Differences in Flight and Hunting Behavior? *PLOS ONE*, 9(8), e106094. doi: 10.1371/journal.pone.0106094.

[233] E. R. Dumont. (2010). Bone density and the lightweight skeletons of birds. *Proceedings of the Royal Society B: Biological Sciences*, 277(1691), 2193–2198. doi: 10.1098/rspb.2010.0117.

[234] E. De Margerie, S. Sanchez, J. Cubo, J. Castanet. (2005). Torsional resistance as a principal component of the structural design of long bones: comparative multivariate evidence in birds. *The Anatomical Record Part A: Discoveries in Molecular, Cellular, and Evolutionary Biology: An Official Publication of the American Association of Anatomists*, 282(1), 49–66. doi: 10.1002/ar.a.20141.

[235] M. Bennett, J. A. Stafford. (1988). Tensile properties of calcified and uncalcified avian tendons. *Journal of Zoology*, 214(2), 343–351. doi: 10.1111/j.1469-7998.1988.tb04727.x.

[236] J. R. Hutchinson, J. W. Rankin, J. Rubenson, K. H. Rosenbluth, R. A. Siston, S. L. Delp. (2015). Musculoskeletal modelling of an ostrich (Struthio camelus) pelvic limb: influence of limb orientation on muscular capacity during locomotion. *PeerJ*, 3, e1001. doi: 10.7717/peerj.1001.

[237] T. Bachmann, J. Emmerlich, W. Baumgartner, J. M. Schneider, H. Wagner. (2012). Flexural stiffness of feather shafts: geometry rules over material properties. *Journal of Experimental Biology*, 215(3), 405–415. doi: 10.1242/jeb.059451.

[238] I. M. Weiss, H. O. Kirchner. (2010). The peacock's train (Pavo cristatus and Pavo cristatus mut. alba) I. structure, mechanics, and chemistry of the tail feather coverts. *Journal of Experimental Zoology Part A: Ecological Genetics and Physiology*, 313(10), 690–703. doi: 10.1002/jez.641.

[239] P. L. Pap, G. Osváth, K. Sándor, O. Vincze, L. Bărbos, A. Marton, R. L. Nudds, C. I. Vágási. (2015). Interspecific variation in the structural properties of flight feathers in birds indicates adaptation to flight requirements and habitat. *Functional Ecology*, 29(6), 746–757. doi: 10.1111/1365-2435.12419.

[240] A. M. Rijke, W. A. Jesser. (2011). The water penetration and repellency of feathers revisited. *The Condor*, 113(2), 245–254. doi: cond.2011.100113.

[241] B. Filshie, G. Rogers. (1962). An electron microscope study of the fine structure of feather keratin. *The Journal of Cell Biology*, 13(1), 1–12. doi: 10.1083/jcb.13.1.1.

[242] H. Hertel. (1966). *Structure, Form, Movement*. Reinhold Publishing Co.

[243] B. Wang, M. A. Meyers. (2017). Seagull feather shaft: Correlation between structure and mechanical response. *Acta Biomaterialia*, 48, 270–288. doi: 10.1016/j.actbio.2016.11.006.

[244] R. Fraser, T. MacRae. (1957). Part I: Introductory Survey. *Textile Research Journal*, 27(5), 379–384. doi: 10.1177/004051755702700506.

[245] T. N. Sullivan, B. Wang, H. D. Espinosa, M. A. Meyers. (2017). Extreme lightweight structures: avian feathers and bones. *Materials Today*, 20(7). doi: 10.1016/j.mattod.2017.02.004.

[246] A. Elowson. (1984). Spread-wing postures and the water repellency of feathers: a test of Rijke's hypothesis. *The Auk*, 101(2), 371–383. doi: 10.1093/auk/101.2.371.

[247] D. Hally. (1987). Calculation of the Moments of Polygons. Technical Report AD-A183 444, Defence Research Establishment Suffield Ralston, Alberta, CA. URL: https://apps.dtic.mil/dtic/tr/fulltext/u2/a183444.pdf.

[248] A. M. Heers, J. W. Rankin, J. R. Hutchinson. (2018). Building a Bird: Musculoskeletal Modeling and Simulation of Wing-Assisted Incline Running During Avian Ontogeny. *Frontiers in Bioengineering and Biotechnology*, 6, 140. doi: 10.3389/fbioe.2018.00140.

[249] J. A. Myers. (1962). Handbook of equations for mass and area properties of various geometrical shapes. Technical Report, Naval Ordnance Test Station, China Lake, CA, USA. URL: https://apps.dtic.mil/sti/pdfs/AD0274936.pdf.